# OPTIMIZATION OF AN IMAGE-GUIDED RADIATION THERAPY PROTOCOL FOR ADVANCED STAGE LUNG CANCER

by

PETER HOANG, B.Sc.

Graduate Program in Radiation Sciences

A thesis submitted to the School of
Graduate Studies in partial fulfillment of
the requirements for the degree of
Master of Science

McMaster University
Hamilton, Ontario, Canada

McMaster University MASTER OF SCIENCE (2016) Hamilton, Ontario

(Radiation Sciences; Medical Physics)

| | |
|---|---|
| TITLE: | Optimization of an Image-guided Radiation Therapy Protocol for Advanced Stage Lung Cancer |
| AUTHOR: | Peter Hoang, B.Sc. (McMaster University) |
| SUPERVISOR: | Dr. Marcin Wierzbicki |
| NUMBER OF PAGES: | xi, 133 |

# Abstract

Image-guided radiation therapy (IGRT) provides accurate and precise tumour targeting. To ensure adequate coverage in IGRT, a planning target volume (PTV) margin is added around the target to account for treatment uncertainties. Treatment plans are designed to deliver a high percentage of the prescription dose to the PTV; thus, portions of healthy tissue are also subjected to high radiation dose. IGRT employs dedicated devices that enable visual assessment of some treatment uncertainties, such as variations in patient set-up. Safe and effective IGRT delivery requires adherence to disease site-specific protocols that describe process details such as imaging technique, alignment method, and corrective action levels. Protocol design is challenging since its effect on treatment accuracy is currently unknown. This thesis aims to understand the interplay between lung IGRT protocol parameters by developing a framework that quantifies geometrical accuracy.

Deformable image registration was used to account for changes in target shape and size throughout treatment. Sufficient accuracy was considered when at least 99% of the target surface fell within the PTV. This analysis revealed that the clinical 10 mm PTV margin can be safely reduced by at least 2 mm in each direction.

Evaluation of IGRT accuracy was extended to spinal cord alignment. Simulations were carried out with various matching strategies to correct for set-up error, including rotational off-sets. Inappropriate combinations of matching strategies and safety margins resulted in sub-optimal geometrical coverage. Various lung IGRT protocol options were recommended to optimize accuracy and workflow efficiency. For example, an 8 mm PTV margin can be used with spinal cord alignment, a 4 mm cord margin, and up to 5° of rotational error. A more aggressive protocol involved a 6 mm PTV margin with direct target alignment, a 5 mm cord margin, and a 4° rotational tolerance.

**Keywords:** image registration; image-guided radiation therapy; lung cancer; safety margins; rotational tolerance; set-up error

# Contents

# Acknowledgements

First and foremost, I would like to express my sincere gratitude to my supervisor, Dr. Marcin Wierzbicki for his continuous support, patience, and immense knowledge during my MSc study. Marcin, your guidance and support not only helped me in conducting research and writing this thesis, it also gave me an appreciation for the challenges and opportunities that life has to offer. My gratitude also extends to Dr. Kevin Diamond and Dr. Orest Ostapiak for their insightful comments in the final revision of this work.

Special thanks to the educators from McMaster University: Dr. Tom Farrell, Dr. Soo-Hyun Byun, and Mr. Dave Tucker who have enlightened me with their passion for medical and health physics.

To all my friends who have helped me get here, especially: Suketu Patel, Peggy Le, Ishan Patel, Michelle Lord, Ajay Rajaram, Radek “Shadowkeys” Sadowski, Andrew Tam, and Chris Rowley.

I wish to also thank my parents for supporting me throughout my entire academic career. And last but not least, to Vy: thank you for always being by my side, for understanding, and for bringing me joy.

Funding for this work was provided by donor contributions to the Ontario Graduate Scholarship and Queen Elizabeth II Graduate Scholarship, namely with funds from the estate of Eugene G. Bolotkin.

# List of Tables

# List of Figures

# List of Abbreviations, Symbols, and Nomenclature

| | |
|---|---|
| 3D | Three-Dimensional |
| 4D | Four-Dimensional |
| AIP | Average Intensity Projection |
| AP | Anterior-Posterior |
| CBCT | Cone Beam Computed Tomography |
| cROT | Clinical Rotations |
| CRT | Conformal Radiation Therapy |
| CT | Computed Tomography |
| CTV | Clinical Target Volume |
| DIBH | Deep Inspiration Breath Hold |
| DIR | Deformable Image Registration |
| DOF | Degrees of Freedom |
| DNA | Deoxyribonucleic Acid |
| DVH | Dose-volume Histogram |
| EBRT | External Beam Radiation Therapy |
| FBCT | Free-breathing Computed Tomography |
| FFD | Free-Form Deformation |
| GTV | Gross Tumour Volume |
| HU | Hounsfield Unit |
| ICRU | International Commission on Radiation Units and Measurements |
| IGRT | Image-guided Radiation Therapy |
| IM | Internal Margin |
| IMRT | Intensity Modulated Radiation Therapy |
| ITV | Internal Target Volume |
| LR | Left-Right (lateral) |
| MI | Mutual Information |
| MIP | Maximum Intensity Projection |
| MLC | Multi-leaf Collimator |
| MRI | Magnetic Resonance Imaging |
| NSCLC | Non-small Cell Lung Cancer |
| OAR | Organs at Risk |
| pCT | Planning Computed Tomography (Image) |
| PET | Position Emission Tomography |
| PRV | Planning Organ at Risk Volume |
| PSCT | Perfect Set-up Computed Tomography (Image) |

| | |
|---|---|
| PTV | Planning Target Volume |
| RMS | Root Mean Square |
| ROI | Region of Interest |
| rPSCT | Rotated Perfect Set-up Computed Tomography (Image) |
| SBRT | Stereotactic Body Radiation Therapy |
| SCLC | Small cell Lung Cancer |
| sCS | Simulated Couch Shift |
| sCS-r | Simulated Couch Shift (for rotational error) |
| SI | Superior-Inferior |
| T | Transformation |
| TPS | Treatment Planning System |
| Tx | Treatment |
| VMAT | Volumetric Arc Therapy |
| VTK | Visualization Toolkit |

# Chapter 1

# Introduction and Background

## 1.1 Introduction to Lung Cancer

In 2015, it is estimated that 196,900 Canadians will develop cancer and 78,000 will die of the disease with lung cancer as the leading cause of death (Canadian Cancer Society, 2015). While there are many underlying causes and potential risk factors such as smoking, alcohol consumption, or hereditary conditions, lung cancer can also develop spontaneously. Lung cancer development generally involves forms of genetic mutations that eventually lead to uncontrollable cell growth in lung tissue and the possibility of malignant spread outside of the lungs. The common end points of untreated cancer are morbidity and death due to decreasing normal operating functions of the affected organs or tissues. The current 5-year relative survival rate for lung cancer is about 17%, which is the third lowest following pancreatic (8%) and esophageal (14%) cancers (Canadian Cancer Society, 2015). Lung cancers are categorized into non-small cell lung cancer (NSCLC) or small cell lung cancer (SCLC) with adenocarcinomas, squamous cell cancers, and large-cell cancers grouped under NSCLC (Beyzadeogly, Ozyigit, & Ebruli, 2010).

Available treatment strategies for lung cancer include surgery, chemotherapy, radiation therapy, or a combination. Surgery is typically used as an effective treatment for solid, well-defined tumours often found in early stage

disease, and is not generally recommended to patients in advanced stage lung cancer where distant metastases may be present (Henschke *et al.*, 1999). Direct deoxyribonucleic acid (DNA) damage or disruption of tumour cell proliferation can be achieved through the administration of chemotherapy. Radiation therapy is often performed concurrently with chemotherapy to eradicate tumours. Ionizing radiation may be delivered externally using a linear accelerator or internally by implanting radioactive isotopes within the body.

## 1.2 Lung Cancer Radiation Therapy

The goal in any of the above treatments is to maximize the therapeutic ratio by maximizing the chance of eradicating the tumour while minimizing the chance of side effects. It is well-known that malignant tumour cells are very sensitive to the damaging effects of ionizing radiation and are preferentially killed over normal cells when treatments are delivered with adequate prescriptions (E. Hall & Giaccia, 2006). Radiation therapy therefore attempts to deliver a maximal dose of radiation to the target (tumour) while minimizing dose to normal tissues. External beam radiation therapy (EBRT) employs a specifically-designed linear accelerator to generate and deliver ionizing radiation to targets within the patient. EBRT may be delivered using directly ionizing particles such as electrons and protons, but the majority of lung treatments are performed using photons which are indirectly ionizing; their interactions within the body produce secondary electrons that then deposit dose (Grutters *et al.*, 2010).

Conventional radiation therapies are typically administered over several weeks and consist of delivering a fraction of the total dose during daily treatments. Fractionated delivery gives normal cells time to repair following radiation induced DNA damage while tumour cells do not recover due to significantly slower repair mechanisms. Delivering very high doses to the tumour is restricted by the radiation tolerance of normal tissue surrounding the target volume (Baskar, Dai, Wenlong, Yeo, & Yeoh, 2014). For instance, the probability of causing radiation pneumonitis in normal lung tissue is dictated by the V20Gy, or the proportion of total lung receiving at least 20 Gy (Graham *et al.*, 1999; Murshed *et al.*, 2004). Other factors that affect the prescription dose are disease stage, whether other modalities are used in conjunction with radiation, and the overall health of the patient. Overall, 64% of NSCLC cases require radiation therapy (Tyldesley, Boyd, Schulze, Walker, & Mackillop, 2001), typically delivered in 2 Gy daily fractions for a total dose of 60-66 Gy (Beyzadeogly *et al.*, 2010). The use of radiation therapy is seen in about 54% of SCLC (Tyldesley *et al.*, 2001) cases where a total dose of 40-45 Gy is delivered in 1.8-2 Gy fractions (Beyzadeogly *et al.*, 2010).

In the last couple decades several techniques for delivering EBRT were developed. In three-dimensional conformal radiation therapy (3DCRT) a computerized tomography (CT) image of the patient is used in a treatment planning system (TPS) to conform the beam shape to the contour of the target as seen in the beam's eye view (Bucci, Bevan, & Roach, 2005). Considered a conventional technique, 3DCRT is capable of reducing dose to surrounding normal tissue, improving the therapeutic ratio. Difficulty still remains in sparing critical structures

that overlap the target (E. J. Hall & Wuu, 2003). Dose escalation could not be achieved without a more conformal dose distribution. Takahashi and Matsuda (1960) pioneered the idea of modulating the intensity of the radiation beam. The full integration of this idea into intensity-modulated radiation therapy (IMRT) was achieved in the late 80's and early 90's as multi-leaf collimators (MLC) were developed to create collimated fields for 3DCRT (Bortfeld *et al.*, 1990; Brahme, 1988; Webb, 1989). At the same time, inverse-planning was being developed. Inverse-planning allowed dosimetrists to set specific goals relating to target coverage and dose constraints in the radiation treatment plan. A computerized optimization algorithm would then produce optimal treatment parameters based on the treatment planner's goals. In contrast, 3DCRT was traditionally planned using forward-planning (Oldham, Neal, & Webb, 1995) where treatment parameters including number of fields, angles, and collimator settings were manually set by the dosimetrist and then resulting dose distribution computed. The combination of 3DCRT, MLCs, and inverse-planning form the basis for IMRT, where radiation beam intensity and weight are optimized to meet planning objectives through manipulation of collimator jaws and MLC leaf positions (Oldham *et al.*, 1995; Webb, 2003). Advantages of IMRT over 3DCRT have been documented in many studies with respect to dose conformity to target and dose sparing to surrounding tissues (Bortfeld, 2006; E. J. Hall & Wuu, 2003; Mok *et al.*, 2011). Lastly, volumetric modulated arc therapy (VMAT), which can be considered a variation of IMRT, delivers its prescribed dose over a continuous arc (Otto, 2008). With increasing complexity of treatment techniques there is increased reliance on

supporting processes, including treatment simulation, structure delineation, and dose calculation.

## 1.3 Radiation Therapy Process

Typical treatments for lung radiation therapy require accurate 3D representation of patient anatomy. This can be achieved through treatment simulation which typically employs CT imaging. A kilo-voltage (kV) fan beam x-ray source rotates around the patient and passing photons are captured by an array of detectors. At the same time, patient comfort and immobilization are assessed and documented. Raw data can be visualized as a sinogram yielding information on detector position and projection angle. Filtered back projection or iterative reconstructions are then used to obtain 3D maps of linear attenuation coefficient from the projections (Pan, Sidky, & Vannier, 2009). Image voxel intensities are set to Hounsfield Units (HU), a scale that normalizes any linear attenuation coefficient $\mu$ to the attenuation coefficient of water $\mu_w$:

$$HU = \frac{\mu - \mu_w}{\mu_w} \times 1000. \quad (1)$$

Once the tumour is localized in the CT scan, the patient's skin is tattooed to help guide patient positioning. CT image data are then exported to the TPS for further processing.

The next step in the radiation therapy planning process is to identify and contour target volumes and nearby dose-limiting structures. The International Commission on Radiation Units and Measurements (ICRU) has published reports to aid with universal reporting of radiation doses in therapy (ICRU & International

Commission on Radiation Units and Measurements, 1993; ICRU & Measurements, 1999). Reports 50 and 62 have guidelines for specifying volumes for prescribing doses in radiation therapy. The "Gross Tumour Volume" (GTV) can be defined based on diagnostic or functional imaging modalities such as CT, magnetic resonance imaging (MRI), or positron emission tomography (PET). The GTV represents palpable or visible extent of the tumour. Microscopic extension of the disease is contained by expanding the GTV into the "Clinical Target Volume" (CTV). Typically, it is the CTV that needs to be treated adequately to achieve the aim of therapy. For radiation therapy of advanced lung cancer, the CTV margin typically ranges from 5-8mm (Beyzadeogly *et al.*, 2010), although depending on patient specific factors and the technique for contouring the GTV, the margin may be as small as 0 mm. The CTV may then be combined with the internal margin (IM) which would encompass the motion of the CTV due to breathing to finally form the "Internal Target Volume" (ITV). Lastly, uncertainty in patient-beam positioning is accounted for by expanding the ITV by the set-up margin (SM) to obtain the "Planning Target Volume" (PTV). Treatment plans are typically designed such that 95% of the prescribed dose covers 95% of the PTV with a maximum dose less than 107%. This is an attempt to ensure that the dose delivered to the CTV will be within about 5% of the prescription.

Additionally, ICRU requires delineation of organs at risk (OAR). For lung radiotherapy these typically include normal lung tissue, esophagus, heart, and spinal cord. OARs are contoured because normal tissue has specific tolerance to radiation, a factor that often influences the prescribed dose and the treatment

technique. Studies of normal tissue tolerance in the modern radiotherapy setting are ongoing although a classical set of values is available (Emami *et al.*, 1991) . Finally, since it is not possible to position the OARs exactly during treatment, the ICRU has introduced the concept of the Planning Organ at Risk Volume (PRV). This is a geometric expansion around any given OAR meant to encompass movement, changes in shape and/size, and set-up error (ICRU & Measurements, 1999; McKenzie, van Herk, & Mijnheer, 2002). The PRV for an OAR is analogous to the PTV for a CTV.

Dose calculations within the TPS can be achieved with various dose calculation engines. These techniques often require knowledge of the basic radiation beam properties typically quantified using the percentage depth dose profile (PDD), horizontal beam profile or off-axis ratio, and output factor. The beam's output factor depends on collimator and phantom scatter and is thus driven by field size. The PDD and beam profile provide information on surface dose, build-up, fall-off, penumbra, and flatness. These quantities are measured in a water tank in simple conditions. Complex patient geometries are considered in 3D dose calculations by correcting the measurements for irregular field apertures, patient contours, and inhomogeneities, or by using model-based algorithms that calculate dose from first principles (Ahnesjö & Aspradakis, 1999).

The appropriateness of a treatment plan following dose calculations is commonly evaluated using dose volume histograms (DVH). A DVH can be used to determine what volumetric fraction of a structure was covered by a specific dose level. For example, sufficient target coverage would be indicated if 95% of the

PTV receives at least 95% of the prescription dose. DVHs are also used to ensure that OARs do not exceed their tolerance doses (Beyzadeogly *et al.*, 2010).

## 1.4 Accuracy of Lung Radiation Therapy

Improvements in delivery techniques have resulted in very conformal dose distributions around the PTV. However, the current prescription dose continues to achieve relatively low 5-year survival rates. Even a high-dose regime of 74 Gy given in 2 Gy fractions did not improve survival compared to standard fractionation, and might even be harmful (Bradley *et al.*, 2013). Dose escalation is limited by lung radiation pneumonitis and fibrosis, which both lead to loss of function and possibly death. Radiotherapy has however been shown to be effective in providing local control. In one study of 8 patients, GTVs decreased by 15-70% (Britton *et al.*, 2007), while another study of 60 patients revealed an average GTV reduction of about 50% by treatment completion (Lim *et al.*, 2011). These observations give hope that survival can be increased with advancement in care and technology, particularly by decreasing amount of healthy lung irradiated. Additionally, noticeable change in primary tumour volume has prompted some groups to investigate adaptive radiation therapy (ART), where the dose depends on daily anatomy and previous treatment fractions (Guckenberger, Richter, Wilbert, Flentje, & Partridge, 2011; Yan, Vicini, Wong, & Martinez, 1997).

To improve lung radiation therapy, further work is needed in inhomogeneity corrections for dose calculation algorithms, methods for reducing variations in target and OAR delineations, and techniques for addressing organ motion. Dosimetry for lung radiation therapy is affected by increased photon fluence,

increased penumbra, and decreased field flatness. The underlying cause of these effects is the heterogeneous nature of the anatomy ranging from low density lung tissue (~ 1/3 $g \cdot cm^{-3}$) to soft tissue or tumour (~1 $g \cdot cm^{-3}$) to bone (~ 1.2 $g \cdot cm^{-3}$). The primary physical interaction of photons at 6 MV is Compton scattering (Miller, Bonner, & Kline, 1998). The resulting electrons have a greater range in lower density material and scatter outside the field boundary leading to penumbral broadening. For small fields, this also results in lower dose at the field edges and decreased field flatness, potentially causing under dosage of the tumour periphery (Ekstrand & Barnes, 1990; Metcalfe, Wong, & Hoban, 1993). The underlying process is known as lateral electronic disequilibrium and is shown in Figure 1.1. Smaller lesions that are treated with smaller field sizes and higher energies are more affected by this phenomenon as the Compton electron range in lung tissue is comparable to that of the field size (Duggan & Coffey, 1998). Properly accounting for lateral disequilibrium involves modeling these effects using dose calculations algorithms (Metcalfe *et al.*, 1993). Previous methods relied on correction-based algorithms such as Bathos Power law or equivalent-tissue-air-ratio (ETAR). Current standards often employ model-based algorithms using convolution-superposition or pencil beam models (Ahnesjö & Aspradakis, 1999), while the ability to directly simulate the physical interactions of particles using Monte Carlo-based dose calculation algorithms holds great potential for improved accuracy (Verhaegen & Seuntjens, 2003).

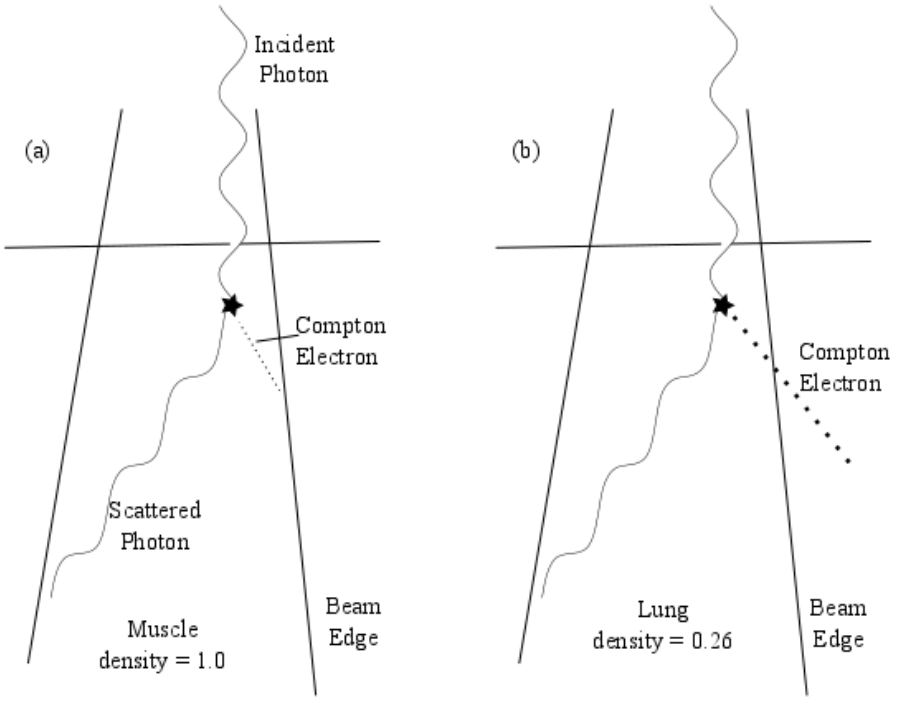


Figure 1.1. Effect of tissue density on electron equilibrium. (a) shows a Compton electron scattered within the field boundary, whereas (b) shows scatter outside the field. Adapted from Ekstrand & Barnes, 1990.

Although ICRU has established guidelines for contouring, large variations in physician delineations of lung tumours pose an additional concern (Senan *et al.*, 1999; Van de Steene *et al.*, 2002; Vorwerk *et al.*, 2009). For instance, even in the presence of detailed instructions, Vorwerk *et al.* (2009) found that lung GTV contours conducted by ten different radiation oncologists were only similar in 16% of the cases. Inter-observer variations are attributed to specialty (e.g., radiation oncologist, radiologist, medical physicist), training, personal bias, and imaging visibility (Njeh, 2008). However, anatomical information from CT images along with function information from PET imaging has improved the consistency of tumour volume delineation (Feng *et al.*, 2009; Steenbakkers *et al.*, 2006).

Additionally, accuracy of lung radiation therapy is affected by organ motion. Of particular concern is respiration that results in moving lung tumours (Admiraal, Schuring, & Hurkmans, 2008; Heath, Unkelbach, & Oelfke, 2009; Juhler Nøttrup *et al.*, 2007). More time is spent in the exhale phase than the inhale phase; this is modeled by an asymmetric periodic function, but breathing traces can be irregular (Shirato, Seppenwoolde, Kitamura, Onimura, & Shimizu, 2004). Various studies have shown that the predominant motion lies in the superior/inferior (SI) direction (Britton *et al.*, 2007; H. H. Liu *et al.*, 2007). Liu *et al.* (2007) assessed 3D respiratory-induced tumour motion and found that for 95% of the tumors, the magnitude was less than 0.59 cm, 0.40 cm. and 1.34 cm in the lateral (LR), anterior/posterior (AP), and SI directions respectively. Additionally, they found that tumour motion was associated with diaphragm motion and tumour size, SI location, and disease stage. Motion affects image acquisition, treatment planning, and treatment delivery. Motion during diagnostic image acquisition causes image artifacts and results in incorrect representation of patient geometry and tissue density (Balter, Ten Haken, Lawrence, Lam, & Robertson, 1996). These artifacts ultimately affect treatment planning since accurate structure delineation and dose calculations both depend on patient anatomy. Motion artifacts seen on free-breathing CT (FBCT) where pitch is set to ~ 1 result in a discontinuous appearance from axial projections being acquired at various stages of the respiratory cycle. Incorrect tissue densities are displayed when motion is present within a single slice acquisition; this leads to averaging of tissue densities seen as blurring on the image (Gagné & Robinson, 2004). Furthermore, a 3D scan may not

provide adequate information on tumour position since it only represents a single snapshot of patient anatomy during a particular phase of the respiratory cycle (Evans, Coolens, & Nioutsikou, 2006; Shimizu *et al.*, 2000). Henkelman and Mah (1982) reported the dosimetric consequences of organ motion. They found that AP beams resulted in 3% root-mean-square difference of dose at various landmarks between time-averaged dose and dose delivered at exhale. Not considering organ motion in treatment planning leads to tumour under dosage (Kung, Zygmanski, Choi, & Chen, 2003). The work of Bortfeld *et al.* (2002) investigated whether IMRT delivery techniques are sensitive to organ motion due to interplay between organ and MLC leaf motion. The idea is that altered dose distributions may occur if there is movement between or during IMRT beam delivery. Volume elements (voxel) of a tumour could potentially receive little to no dose due to organ motion hiding the voxels behind MLC leaves. The biggest effect was observed at the boundaries that had steep dose gradients which result in penumbral broadening and reduced dose conformity.

## 1.5 Managing Respiratory Motion in Radiation Therapy

Various approaches are available to manage respiratory motion during planning and treatment. Designing a PTV to include an ITV that encompasses full CTV motion has become common practice, but is still challenged by others who plan on a tumour's time-averaged position. Management during treatment delivery may involve use of patient immobilization, breathing techniques, or beam timing. In general, five approaches were reported by American Association of Physicists in Medicine (AAPM) Task Group 76 report: (1) motion-encompassing methods,

(2) forced shallow breathing, (3) breath-hold, (4) gating, and (5) respiratory-synchronized radiation therapy (Keall *et al.*, 2006).

### 1.5.1 Motion Encompassing Methods

Compensating for respiratory motion can be accomplished with an appropriate PTV margin. As previously stated, tumour motion can be considered to be the internal margin and added to a CTV to form an ITV. Estimating the tumour range of motion generally takes place during treatment simulation using various CT imaging strategies: (1) slow CT; (2) inhale and exhale breath hold CT; and (3) 4D CT.

The use of a slow revolution CT scan at approximately 4 seconds per rotation has shown to produce larger, but reproducible lung tumour volumes relative to fast CT scanning for free-breathing simulations; thus better capturing tumour movement (Lagerwaard *et al.*, 2001; Wurstbauer, Deutschmann, Kopp, & Sedlmayer, 2005). Patients can still be treated under free-breathing conditions using this method; however, tumour size and shape are unknown, surrounding anatomy is blurred (Chinneck, McJury, & Hounsell, 2010), and due to motion blurring, this approach is not recommended with tumours involving the mediastinum or chest wall (Keall *et al.*, 2006).

Another approach involves the acquisition of two breath hold CT scans at inhale and exhale. The extent of the lung tumour is captured during both phases by fusing separate sets of contours. Shih, Jiang, Aljarrah, Doppke, and Choi (2004) found that this technique produces the smallest internal margins compared to approaches that use the free-breathing fast or slow CTs. However, drawbacks of

inhale and exhale breath-hold CT include difficulties in patient execution, double scan time, and the fact that extreme positions may not be comparable to free-breathing positions (Keall *et al.*, 2006).

An important advancement in imaging technologies, four-dimensional computed tomography (4DCT) has resulted in improved target delineation and motion assessment (Keall *et al.*, 2006). Additionally, 4DCT has aided the implementation of other motion management techniques, including breath-hold and gating. During 4DCT, sets of 3DCT images are produced at specified intervals of the breathing cycle. This is achieved by time stamping the acquired projections while patient breathing cycles are recorded. Either internal or external markers are used to track the patient breathing cycle. External markers are more commonly used and generally involve tracking abdominal displacement via infrared technology or measuring breathed volume using a spirometer (Ford, Mageras, Yorke, & Ling, 2003; Vedam *et al.*, 2003). Full breathing cycles are typically binned into 10 equally spaced phases, which are then used to sort the image projections. Approaches to acquiring 4D data on multi-slice CT scanners involve using axial, helical, or cine acquisition protocols. During an axial acquisition, projections are continuously acquired at each couch position for a duration that is longer than the patient breathing cycle. Employing a helical scanning protocol involves sending a signal from the respiratory monitoring system to the CT scanner that tags the point of end-inspiration on the sinogram. The remaining time points are then linearly interpolated and used to reconstruct the corresponding image sets. A cine acquisition mode also requires simultaneously monitoring patient breathing.

However, images are acquired without moving the couch. Variations in patient breathing patterns may result in incorrectly assigning a breathing phase with an acquired projection. Amplitude-based binning can be employed to overcome this issue. Phase binning assigns an image to a bin according to the phase of the breathing signal at the time of image generation, whereas amplitude binning assigns images according to the breathing cycle's full amplitude. This amplitude correlates with the amplitude of the diaphragm motion and has been shown to be the superior binning mode for 4DCT (Abdelnour *et al.*, 2007). Various uses of 4DCT image data can produce patient specific margins. The most basic method is to generate internal margins from individual GTV contours drawn on all phases. Post processing tools such as maximum intensity projection (MIP) (Underberg, Lagerwaard, Slotman, Cuijpers, & Senan, 2005) and average intensity projection (AIP) (Bradley *et al.*, 2006) can reduce this workload. The MIP technique creates a single CT image from the 4DCT dataset where the CT number at each voxel represents the maximum across the breathing cycle. Underberg *et al.* (2005) validated ITV generation using the MIP image and found this technique to be clinically reliable for gated and non-gated lung radiation therapy. Alternatively, slow CT scans can be reproduced using AIP processing of 4DCT data (Bradley *et al.*, 2006). Each voxel of an AIP image represents the mean CT number across the whole breathing cycle. Data from 4DCT also allows for treatment planning using the mean tumour position which can be obtained using a single mid-ventilation CT scan (Wolthaus *et al.*, 2006). A mid-ventilation CT scan can be obtained from the 4DCT data set by calculating the mean tumour or diaphragm position and

identifying the corresponding respiratory phase. Additional margin that accounts for motion amplitude is added to the time average tumour position. Work of Bosmans and Buijsen *et al.* (2006) showed superior target volume dose coverage when structures were delineated on a mid-ventilation CT or 4DCT relative to slow and fast FBCT.

### 1.5.2 Forced Shallow Breathing

Forcing patients to breath in a shallow manner has been shown to reduce tumour motion amplitude. This approach is generally not used for conventional lung treatments. Instead, it is more commonly used in stereotactic body radiation therapy (SBRT) where additional immobilization is used to limit breathing motion since high doses are delivered (Fakiris *et al.*, 2009; Negoro *et al.*, 2001). Immobilization may include use of abdominal compression plates, body casts, or vacuum-based systems (Han *et al.*, 2010).

### 1.5.3 Breath Hold

These treatments are delivered during breath holding (typically for 10 seconds) at end-inhalation or end-exhalation phases. The use of deep inspiration breath hold (DIBH) described by Hanley *et al.* (1999) has been associated with a reduction in lung density and as a result, reduced OAR dose, particularly to normal lung and heart. This type of delivery requires additional patient training and equipment for tracking the lung inflation level. Beam control can be handled manually or automatically by external software. Reproducing DIBH for each fraction can be accomplished with an Active Breath Controller (ABC) device which

temporarily halts patient breathing (Wong *et al.*, 1999). As with breath hold CT scans, breath hold treatments can be difficult for specific patients, particular those with additional pulmonary issues.

### 1.5.4 Gating

Beam delivery can still be limited to certain phases of the respiratory cycle while removing patient involvement as seen in breath-hold techniques (Kubo & Hill, 1996; Ohara *et al.*, 1989). Compared to traditional methods, this method results in a reduction in treatment efficiency because the beam is only on during the gating window. Thus, a combination of gating with breath holding is preferred (Keall *et al.*, 2006; Mageras & Yorke, 2004). Gating has a large potential for treatment margin reduction since tumour motion during delivery is reduced. Challenges associated with gated treatments include extensive monitoring, external marker suitability as tumour motion surrogates, and long setup times (Keall *et al.*, 2006).

### 1.5.5 Respiratory-synchronized Radiation Therapy

The capability of modifying treatment beams to account for tumour motion would eliminate the need for internal margins and obtain 100% efficiency. Challenges in this design include: (1) determination of target position; (2) motion prediction; and (3) beam realignment and adaptation (Murphy, 2004). These challenges are met by the need for fast detection and response to changes above specific tolerances. The Cyberknife (Accuray, Sunnyvale CA) is a respiratory-synchronized delivery linear accelerator that is capable of delivering highly

conformable dose distributions with narrow radiation beams (Schweikard, Glosser, Bodduluri, Murphy, & Adler, 2000). It includes a robotic arm with six degrees of motion (translation and rotations along three axes). Target position is acquired through two simultaneous methods: (1) 0.1 Hz sampling for internal gold markers using x-ray imaging; and (2) 60 Hz sampling of external infra-red markers on the patient surface using infra-red tracking. Prediction of tumour motion is performed by correlating internal and external data. Despite irradiating a smaller overall volume of the patient, the Cyberknife system achieves excellent local control rates for early-stage NSCLC (Brown *et al.*, 2007; van der Voort van Zyp *et al.*, 2009). An alternative to Cyberknife is the use of dynamic MLCs (DMLC) to perform tumour tracking and intrafraction motion corrections. DLMCs require specifically designed algorithms that obtain real-time information of target location from a monitoring system and then calculate new MLC positions to account for any changes in target location (McQuaid & Webb, 2006; Sawant *et al.*, 2008).

## 1.6 IGRT Protocols

Widespread adoption of image-guided radiation therapy (IGRT) over the last decade has pushed the limit of maximizing target dose while minimizing dose to normal tissues (D. A. Jaffray, 2012; D. Jaffray, Kupelian, Djemil, & Macklis, 2007). The main driving principle behind IGRT success is the acquisition of anatomical and functional information from various medical imaging platforms. The general process of IGRT is to perform online treatment corrections based on images acquired before or during radiation therapy. Increased sophistication of treatment thus requires an understanding of the clinical workflow when carrying

out IGRT. Components of clinical workflow may include strategies and decisions pertaining to image registration, safety margins, and acceptable error. Changes in one component may impact another. Overall, there should be a standardized IGRT protocol for each treatment approach that clarifies how patients should be corrected, when they should be corrected, and if additional interventions are required (Jaffray *et al.*, 2013). Figure 1.2 shows a basic IGRT workflow. It is therefore important to be capable of quantifying treatment accuracy following IGRT. Poor accuracy using a specific protocol would trigger the need for corrective action.

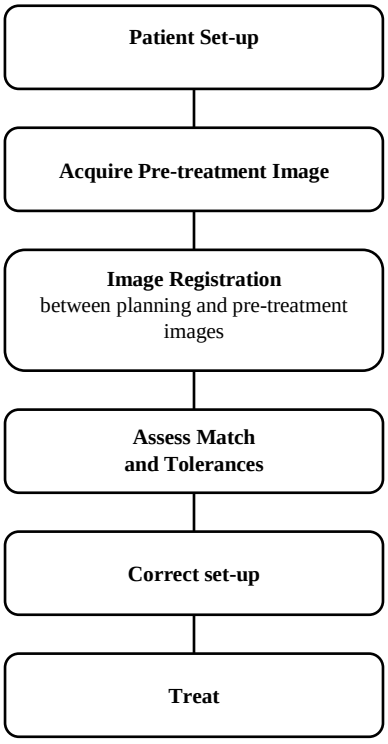


Figure 1.2. Simplified IGRT workflow that improves treatment accuracy by using image registration to assess discrepancies between planning and treatment images.

### 1.6.1 Image Registration

Medical image registration has become an important tool for IGRT. Image registration is the process of determining a spatial transformation that aligns matching features in a source image to those in a target image. The source image is transformed (moved), while the target image is fixed. This transformation yields a geometrical alignment and allows both images to be directly compared. The dimensionality of the transformation can be spatial (e.g. 2D/2D or 3D/3D) or temporal (e.g. within phases of a 4D CT data set) (Maintz & Viergever, 1998). It is possible to perform 2D-to-3D registration using the methods reviewed by Markelj *et al.* (Markelj, Tomaževič, Likar, & Pernuš, 2012), however, the focus of this thesis is on 3D-to-3D registration of CT images. An image registration algorithm is composed of a transformation model that allows source image modifications, a similarity metric that quantifies alignment, and an optimization algorithm that maximizes the similarity of source and target images.

#### 1.6.1.1 Transformation Models

Registration methods can be broadly classified as rigid or non-rigid (Maintz & Viergever, 1998). A rigid transformation preserves the size and shape of the source object. That is, the distance between any pair of points remains constant. Mathematically, rigid transformations can be written as:

$$TR = \begin{bmatrix} & R & & \begin{matrix} t_x \\ t_y \\ t_z \end{matrix} \\ 0 & 0 & 0 & 1 \end{bmatrix}, \qquad (2)$$

$$R = R_x \cdot R_y \cdot R_z$$

$$R_x = \begin{bmatrix} 1 & 0 & 0 \\ 0 & cos\theta_x & -sin\theta_x \\ 0 & sin\theta_x & cos\theta_x \end{bmatrix}$$

$$R_y = \begin{bmatrix} cos\theta_y & 0 & sin\theta_y \\ 0 & 1 & 0 \\ -sin\theta_y & 0 & cos\theta_y \end{bmatrix}$$

$$R_z = \begin{bmatrix} cos\theta_z & -sin\theta_z & 0 \\ sin\theta_z & cos\theta_z & 0 \\ 0 & 0 & 0 \end{bmatrix}, \quad (3)$$

where $R$ represents rotations by angles $\theta_x, \theta_y$ and $\theta_z$ about the x, y, and z axes, respectively and $t_x, t_y$,and $t_z$ represent translations along the x, y, and z axes respectively. Thus, rigid registration is characterized by six degrees of freedom (DOF), where three possible translations and three rotations can be applied to any point (*x*,*y*,*z*) in the source to arrive at the corresponding point (*x'*,*y'*,*z'*) in the target. This transformation of coordinates is seen as:

$$(x', y', z', 1) = TR \cdot \begin{bmatrix} x \\ y \\ z \\ 1 \end{bmatrix}. \quad (4)$$

Rigid body transforms can be complicated with six additional parameters describing scaling and shearing along each dimension. Scaling allows for compressions and expansions while shearing preserves parallel lines before and after transformation. These 12 DOFs describe what is known as affine transformations, and can be written in matrix form as:

$$TRSH = \begin{bmatrix} & & & t_x \\ & RSH & & t_y \\ & & & t_z \\ 0 & 0 & 0 & 1 \end{bmatrix}, \tag{4}$$

$$RSH = R \cdot \begin{bmatrix} s_x & 0 & 0 \\ 0 & s_y & 0 \\ 0 & 0 & s_z \end{bmatrix} \cdot \begin{bmatrix} 1 & h_x & h_y \\ 0 & 1 & h_z \\ 0 & 0 & 0 \end{bmatrix}, \tag{5}$$

where *R* is the rotation matrix, *S* is the scaling matrix with scaling factors $s_{x,y,z}$, and *H* is the shear matrix with shear factors $h_{x,y,z}$ along the x, y, and z axes.

Rigid or affine transformations affect all points globally by the same transformation. In contrast, non-rigid transformations contain a higher number of DOFs that allow local deformations of the source image. Local transformations are complex, require highly correlated source and target data, and can be parameterized in several ways. A common way to describe a local transformation is by a free-form deformation (FFD) or vector field of local translations (Sederberg, Parry, Sederberg, & Parry, 1986):

$$(x', y', z') = (x, y, z) + \Big(t_x(x), t_y(y), t_z(z)\Big), \tag{6}$$

where the displacement vector $(t_x, t_y, t_z)$ maps the source image point $(x, y, z)$ onto its corresponding $(x', y', z')$ point in the target image. These vector fields are discrete and the locations of the displacement vectors are known as nodes. These nodes can vary in density; they can be equally distributed within a grid or concentrated in specific areas. In the former case, equivalent deformations take place, whereas concentrated nodes allow for greater local control. Generally, global registrations are performed as an initial guess to non-rigid transformations.

Calculating individual displacement vectors at all possible points is not computationally efficient. Thus, FFD requires an interpolation method to obtain the transformations at each image element. Some common interpolation methods are nearest neighbour, linear, and splines. Common spline interpolants used are thin-plate and B-splines (Bookstein, 1989; S. Lee, Wolberg, & Shin, 1997) and are typically used for interpolating vector fields or providing local control around defined nodes. Sotiras, Davatzikos, and Paragios (2013) provides an extensive account of the above interpolation methods used in medical image registration. Challenges with medical image registration arise from a lack of image correspondence between the source and target images due to artifacts, noise, changes in anatomy or voxel intensities. Often, there does not exist a unique spatial transformation between two images. Brock (2010) conducted a multi-institutional study investigating accuracy of various non-rigid registration algorithms, also referred to as deformable image registration (DIR). The author indicated that while the majority of DIR algorithms were accurate to within a voxel size, common and universal tests are required to obtain objective benchmarks. Ultimately, the design of transformation models should result in a registration that converges to a realistic solution.

#### 1.6.1.2 Assessment of Data Alignment

Image registration involves an iterative process where the source is repeatedly transformed to match the target. At each stage a similarity metric is used to quantify how well the two images are matched. Similarity metrics can be

geometry- or voxel-based. Geometric features may include landmarks such as points, lines, or surfaces. One geometric-based method of aligning images minimizes the distance between the corresponding features. Voxel-based methods depend on image intensity data.

One intensity-based alignment measure for registration of images with differences in contrast for the same tissues is mutual information. This is of particular interest in this thesis due to the focus on CT to cone-beam CT (CBCT) registration. Mutual information (MI) assumes a functional relationship between voxel intensities (information) in the source and target images. A discussion of MI involves an understanding of entropy. Entropy (Shannon, 2001) quantifies the amount of information in an image:

$$H(A) = -\sum_{a} p(a) \log p(a), \tag{7}$$

where *p(a)* is the probability of having voxel intensity *a* within image *A*. The probabilities are typically obtained from a 2D histogram. Entropy is maximized when all probabilities are equal and minimized when all probabilities are zero except for one. That is to say, entropy is high if there is a lot of variability in intensities and low if there is no variability. For registration, good image alignment occurs (Wells, Viola, Atsumi, Nakajima, & Kikinis, 1996) with minimization of joint entropy *H(A,B):*

$$H(A,B) = -\sum_{a}\sum_{b} p(a,b) \log p(a,b), \tag{8}$$

where *p(a,b)* is the probability that source image *A* and target image *B* have intensities *a* and *b* respectively in the same location. One limitation of this metric

is that *H(A,B)* may not be truly minimized even when the images are registered due to a dependence on the overlap region where *H(A,B)* is calculated. This problem would occur if there exists a large number of low intensity voxels in the overlap region. The MI metric is used to overcome this limitation. MI minimizes joint entropy and maximizes individual information content in the overlap region (Collignon *et al.*, 1995):

$$MI(A,B) = H(A) + H(B) - H(A,B), \tag{9}$$

where *H(A)* and *H(B)* are entropies of the source and target images calculated only in the overlap region. Dependence on the amount of image overlap is not completely eliminated by MI. Studholme, Hill, and Hawkes (1999) proposed the normalized mutual information (NMI) metric where MI is normalized with respect to joint entropy. The survey paper by Sotiras *et al.* (2013) looks at other existing similarity metrics used in medical image registration and the possibility of combining various metrics together.

#### 1.6.1.3 Optimization

Optimization algorithms are necessary for image registration to maximize the similarity metric in a computationally efficient manner. A commonly employed optimization heuristic is the downhill simplex method (Nelder & Mead, 1965). In general, the simplex represents a geometrical figure with one more vertex than dimensions. For instance, an image registration algorithm employing a three DOF transformation model would iteratively modify a tetrahedron in 3D parameter space. The goal is to maximize a similarity metric. The downhill simplex approach

first calculates a similarity metric at all vertices and the vertex with the lowest similarity measure undergoes modifications that include reflection, expansion, or contraction. Optimization is complete if changes in the function between iterations fall below a tolerance value. The process is simple to implement because it does not require calculations of function derivatives but may result in finding local extrema.

### 1.6.2 PTV Margins

IGRT can be used to reduce PTV margins (Yeung *et al.*, 2009) to either reduce treatment toxicity or enable dose escalation to improve local control (Kilburn *et al.*, 2016). For example, volumetric images obtained using linear accelerator-mounted, CBCT scanners can be used to correct variability in tumour position and surrounding organs at risk (Bissonnette, Purdie, Higgins, Li, & Bezjak, 2009). Following patient set-up, CBCT images are registered with the planning CT and the resulting x-, y-, z-shift is applied to the treatment couch, correcting patient position prior to treatment (Guckenberger *et al.*, 2006; Higgins *et al.*, 2009). Despite CBCT image guidance, smaller PTV margins increase the chance of geometrical misses (van Herk, Remeijer, & Lebesque, 2002). On the other hand, large PTV margins used in conventional lung radiotherapy limit the opportunity for dose escalation, resulting in poor local control rates (Larry, Mary, Bahman, Karen, & Rush, 1993).

Thus, it is critical to optimize PTV margins to ensure sufficient target coverage with minimal exposure to normal tissue. PTV margins vary amongst different institutions (Nabavizadeh *et al.*, 2016). A wide range of margin ‘recipes’

are available based on different weighting factors for systematic and random uncertainties to calculate the expansion required to form the PTV (van Herk, 2004). Grills *et al.* (2008) and Bissonnette *et al.* (2009) have adopted the validated van Herk margin recipe (van Herk, 2004; van Herk, Remeijer, Rasch, & Lebesque, 2000) in their studies assessing the treatment accuracy and margins for stereotactic and conventional lung radiotherapy, respectively. van Herk's margin formula separately accounts for systematic and random errors, which are assumed to respectively shift and blur the dose distribution. Systematic errors are related to uncertainty in treatment preparation (e.g., laser alignment, organ position on imaging, delineation error) and influence all fractions, whereas random errors are associated with uncertainty in treatment execution (e.g., set-up error and organ motion) and only influence the single fraction. Patient positions can be used to estimate the systematic and random errors. Derived from an ideal dose model, this margin formula attempts to find the geometrical margin that ensures the CTV is covered by 95% of the prescription dose for 90% of the population. The population data is compiled as follows to compute the PTV margin:

$$Setup\ Margin = 2.5\Sigma + 0.7\sigma, \tag{10}$$

where $\Sigma$ is the systematic error and $\sigma$ is the random error. These errors can be calculated in a manner that corrects for the small population size and the varying number of fractions for each patient (Remeijer *et al.*, 2000). For $P$ patients, and $F_p$ fractions for each patient $p$, there are $N$ total fractions given by:

$$N = \sum_{p=1}^{P} F_p\,. \tag{11}$$

The overall mean of all errors, *M*, is thus:

$$M = \frac{1}{N}\sum_{p=1}^{P}\sum_{f=1}^{F_p} x_{pf}, \tag{12}$$

where $x_{pf}$ is the set-up error along a single axis measured during fraction *f* for patient *p*. From the patient mean, given by:

$$m_p = \sum_{f=1}^{F_p} \left(\frac{x_{pf}}{F_p}\right), \tag{13}$$

the standard deviation of individual error is calculated as:

$$\sigma_p = \sqrt{\left(\frac{1}{F_p - 1}\right)\sum_{f=1}^{F_p}\left(x_{pf} - m_p\right)^2} \ . \tag{14}$$

The overall random error is calculated as the root mean square of the individual random errors, weighted by ($F_p$-*1*) degrees of freedom:

$$\sigma = \sqrt{\frac{1}{N-P}\sum_{p=1}^{P}\left(F_p - 1\right)\sigma_p^2} \ = \sqrt{\frac{1}{N-P}\sum_{p=1}^{P}\sum_{f=1}^{F_p}\left(x_{pf} - m_p\right)^2} \ . \tag{15}$$

Systematic error, $\Sigma$, represents the mean patient error given by the standard deviation of the individual mean errors:

$$\Sigma = \sqrt{\frac{P}{N(P-1)}\sum_{p=1}^{P} F_p\left(m_p - M\right)^2} . \tag{16}$$

Small sample size in the calculation of $m_p$ introduces a random component in the systematic errors but is corrected by the following estimation:

$$\Sigma' = \sqrt{\Sigma^2 - \frac{\sigma^2}{N/P}}\,. \tag{17}$$

Alternative approaches have involved evaluating lung tumour motion using digital fluoroscopy to produce patient-specific PTVs (Sixel, Ruschin, Tirona, & Cheung, 2003), or conducting visual inspections for geographic misses to propose optimized PTV margins (Bell *et al.*, 2015).

Due to assumptions in the dose model, direct application of the van Herk approach in lung radiotherapy is limited since it does not account for target size, tissue density, or plan conformity. Furthermore, organ and target deformations are ignored. Experimental validation of the van Herk approach for lung radiation therapy yielded conservative margin estimations due to the assumption of perfect plan conformity (Ecclestone, Bissonnette, & Heath, 2013). There were also limitations of the study using digital fluoroscopy for PTV margin estimation (Sixel *et al.*, 2003). The technique did not account for target deformation and motion assessment was performed only at the time of treatment planning. The results may therefore not resemble any variations that occur throughout the course of treatment (Bosmans, van Baardwijk, *et al.*, 2006; Hugo, Yan, & Liang, 2007). More recently, an optimization algorithm (Redpath & Muren, 2005) has been developed to determine treatment margins around moving and deformable targets. However, these deformed treatment targets were manually outlined and were thus subject to intraobserver variability. Studies conducted by Mutanga *et al.* (2011) and Meijer *et al.* (2008) both used voxel tracking to calculate accumulated dose distributions for margin evaluation in prostate cancer. But, Liu and Wu (2011) found geometrical

evaluations to have a greater impact on margin improvement compared to dosimetric evaluations.

### 1.6.3 Matching Strategies

Generally, corrections using IGRT have provided better target coverage compared to initial alignments using tattoos. Image registration attempts to correct for this initial set-up error by aligning the source (treatment) and target (planning) images within a specific region of interest (ROI). Various alignment procedures would produce different residual setup errors. For example, Graff *et al.* (2013) used seven different alignment procedures for head and neck IMRT which resulted in variations in patient setup and ultimately dose distribution. In their study only certain landmarks within relevant PTV margins provided clinically acceptable results. Bony anatomy is a common landmark used in registration. For lung IGRT, matching to bony anatomy, particularly the spinal canal, minimizes additional complications from any residual dose to the spinal cord. However, bony registration has been shown to have poor correlation to tumour position (Guckenberger *et al.*, 2006). Lavoie *et al.* (2012) analyzed target coverage at the beginning, middle, and end of conventional lung IGRT using three scenarios: tattoo alignment, spine registration, and carina registration. While both spine and carina registration were superior to tattoo alignment, the authors found carina matching improved target coverage over spine matching. Conversely, Yangyang, Xiaolong, and Bing (2010) suggested that carina matching should not be used for lung SBRT because of its variable position relative to the spine and tumour, which were both acceptable landmarks. Yet previously, Higgins *et al.* (2009) found a low level of

reproducibility during rotational assessments using automatic soft-tissue (tumour) matching for conventional lung IGRT; thus, deemed soft-tissue matching infeasible. Perhaps discrepancies were due to differences in tumour size, PTV expansion, or method of classifying accuracy. Indeed, there does not exist a universally accepted method to quantify accuracy (geometric or dosimetric) of landmark registration in an IGRT protocol. There also appears to be some confusion regarding which landmark is most suitable for lung IGRT.

### 1.6.4 Rotations

Image registration can determine if patient setup for radiotherapy requires rotational corrections. However, couch corrections are commonly limited to translational shifts (three DOF correction). Margin recipes have even ignored rotational error in setup and tumor motion (Hugo *et al.*, 2007). However, advancement in treatment table tops has enabled full six DOF corrections. This freedom would be beneficial for SBRT where high patient set-up accuracy is required, although the accurate six DOF corrections require adequate immobilization (Guckenberger, Meyer, Wilbert, Baier, *et al.*, 2007). Data analysis conducted by Mancosu *et al.* (2015) of 2945 fractions across 376 patients showed improved patient set-up when a 6 DOF robotic couch-top was employed for various treatment sites, including brain, lung, liver, pancreas, and prostate.

An IGRT protocol should acknowledge rotational errors if they cannot be directly corrected using manual methods (e.g. physically rotating the patient) or automatic methods (e.g. six DOF capable couch). If rotations pose a significant issue in accuracy, six DOF correction in conventional treatments should be

considered. Murphy (2007) proposed a guideline for cases where rotational adjustments are not made. The two guidelines were: (1) registration landmark should coincide with the target site, and (2) rotations should not be included in the set-up correction. The second guideline refers to turning off rotations during image registration. Although rotational errors are not physically corrected, they should be assessed. This implies that IGRT treatments that only employ translational shifts can tolerate some degree of rotational error – the question is how much?

Studies of rotations in radiotherapy have been more focused towards prostate, bladder, and head and neck disease sites. Guckenberger *et al.* (2006) recorded rotational errors greater than 2° in 3.7% of pelvic tumours, 26.4% of thoracic tumours, and 12.4% of head and neck tumours. In the same study, a single dosimetric analysis conducted for a patient treated for spinal metastases resulted in decreased target coverage and significant dose increases to spinal cord due to translation and rotational setup errors. Redpath *et al.* (2009) used a PTV margin optimization algorithm (Redpath & Muren, 2005) to test if CTV rotation following optimal 3D translations resulted in better target alignment for prostate or bladder IGRT. The authors found that translational correction was a more dominating factor for alignment, and that rotational corrections only impacted a small fraction of treatment situations. Conversely, Lips *et al.* (2009) investigated the influence of rotations on prostate IMRT with an integrated tumour boost under image-guidance. They found their online correction protocol without rotations provided limited benefit compared to their offline analysis that incorporated rotational corrections. The influence of rotations in prostate treatments also depends on specific treatment

techniques and margin sizes (Fu *et al.*, 2006). Case by case evaluations of rotational setup errors are suggested for head-and-neck IMRT treatments (Fu, Yang, Yue, Heron, & Saiful Huq, 2013). These methods have been limited by small population size and limited representation of the entire treatment. While Peng *et al.* (2011) performed simulated rotations for intracranial stereotactic radiosurgery up to a maximum of ±7° along all three axes, Cao *et al.* (2012) only applied a single rotation with respect to the roll axis for liver SBRT. These simulations would generally not represent clinical cases and thus an acceptable rotational tolerance cannot be determined.

A limited number of studies have quantified rotational error and its associated impact on treatment accuracy in lung radiotherapy. Impact aside, studies have shown significant variations in amount of rotations seen in lung tumours. Based on six thoracic cases, rotations greater than 2° were observed in 26% of the 48 CBCT images analyzed with maximum of 8° (Guckenberger *et al.*, 2006). More recently, Garibaldi *et al.* (2016) found that 94% of the rotational errors were within 3° measured on 57 lung SBRT patients. In another study, simulated rotational offsets of 1°, 3°, and 5° in roll, yaw, and pitch resulted in small dosimetric differences in lung SBRT of medially located tumours (Yang *et al.*, 2014). Again these types of simulations may not necessarily represent clinical rotations since the rotational offsets were all considered independently – dosimetric coverage was analyzed for a single rotational offset along one particular axis. Translational corrections were shown to compensate for target dosimetric changes due to roll-rotational set-up errors in lung SBRT, but in some cases, OAR dose was

compromised (J. Lee *et al.*, 2015). Translational corrections for rotational set-up errors are met by additional challenges in tumor rotation due to respiration (Paganelli *et al.*, 2015), which have been ignored in the past (Kung *et al.*, 2003; van Herk *et al.*, 2000). The magnitude of rotational error and the influence of target location are expected to vary depending on treatment site along with associated IGRT components, including matching strategy and PTV margin size (Suzuki, Nishiyama, Ueda, Miyazaki, & Tsujii, 2012). The purpose of a rotational action level is to signal significant loss in accuracy if treatment proceeds with a simple translational correction only. If the action level is exceeded, corrective actions may include additional repositioning and imaging, or contacting additional team members for plan reassessment. Currently, there does not appear to be a commonly accepted rotational action level for lung IGRT.

In summary, previous work has focused on specific components of IGRT protocols without considering the effectiveness of the overall method. Image registration serves as the backbone of IGRT as planning and treatment images are aligned to correct for set-up error. Alignment is generally conducted within a specific region of interest and is usually limited to only translational shifts. Corresponding shifts are dependent on the matching strategy used, while acceptable alignment depends on the size of PTV margins that are often visually assessed. This implies that some degree of rotation is tolerated during treatment. An understanding of the interplay between matching strategy and rotational tolerance is required to determine if a particular IGRT protocol result in accurate treatments.

## 1.7 Hypotheses and Projects

A geographical miss results in tumour under dosage and ultimately local control failure following radiation therapy. Implementation of IGRT technologies can improve accuracy of tumour targeting, however, a successful clinical IGRT program may require adherence to a step-by-step-protocol. The overall goal of this thesis was to provide a careful analysis and optimization of the details pertaining to an IGRT protocol to ensure its full benefits are exploited. The IGRT protocol of interest was for advanced stage lung cancer with curative intent at Juravinski Cancer Centre. There are two hypotheses along with two main projects which are explored in the following chapters.

Hypothesis 1: Accounting for target deformation throughout treatment can reduce the currently employed 10 mm PTV margin for lung IGRT. This will be addressed in Project 1 using a unique metric to quantify IGRT accuracy that computes the amount of the ITV within various PTV margins before and after treatment.

Hypothesis 2: Simultaneous optimization of various parameters of a lung IGRT protocol, including matching strategy, rotational tolerance, and PTV margin can improve treatment accuracy. This will be addressed in Project 2 using software that simulates and analyzes treatment accuracy considering the effects of all treatment parameters.

# Chapter 2

# Materials and Methods

## 2.1 Materials

### 2.1.1 Computational Environment

The majority of this work was performed on a workstation running a CentOS 5.10 Linux operating system (The CentOS Project). The Python 2.4 (Python Software Foundation, Delaware, USA) scripting language interfaced with a custom version of the Visualization Tool Kit (VTK) (Kitware Inc., Clifton Park, USA) were used to perform the necessary image processing. Scripts were developed to produce an automated software tool capable of analyzing Juravinski Cancer Centre's (JCC) conventional lung IGRT protocol.

Dose computation was conducted using the Adaptive Convolution technique available in the Pinnacle (Phillips NV, Amsterdam, Netherlands) treatment planning system (TPS).

Statistical analyses were performed using R (R Core Team, Vienna, Austria) and Python. An additional statistical package, PMCMR 4.1, was required for R in order to perform pairwise multiple comparisons of mean rank sums (e.g., Nemenyi test).

### 2.1.2 Image Registration

Results of this work required a two-step alignment between CT and CBCT

images using previously validated image registration algorithms (Wierzbicki, Drangova, Guiraudon, & Peters, 2004). In the first registration, a global transformation was computed with nine degrees of freedom, including 3D translations, rotations, and scalings. The Downhill Simplex optimizer was employed to maximize mutual information (MI). This registration process served as a large-scale image alignment. This algorithm is not exclusive to nine DOFs; any combination of 3D translation, rotations, and scalings can be included (e.g., couch shifts can be simulated with a 3D transformation that only encompasses translations).

Deformable image registration (DIR) was used in the second step to fully register the data. This algorithm has been vigorously validated in thorax CT through animal studies and on MR images of human volunteers (Wierzbicki *et al.* 2004). Furthermore, this algorithm is capable of extracting information even in the presence of motion-induced imaging artefacts (Szpala *et al.* 2005, Wierzbicki *et al.* 2008). The algorithm employs a free-form deformation (FFD) approach with block matching. Once a grid of nodes is placed over the images, the Downhill Simplex algorithm is used to maximize MI in a volume of interest surrounding each node. The size of the volume of interest is the same as the grid spacing. In this FFD, a multi-resolution approach of three registration scales was used with 40 mm grid spacing in the first scale, 20 mm in the second, and 10 mm in the final scale. A limit of 10 iterations was imposed during each scale. A minimum of 50, 100, and 100% of voxels surrounding a particular vector field node was required to be within the mask before the node was included in the registration during scale 1, 2, and 3,

respectively. The magnitude of the deformation was restricted by a regularization term, α, during each scale. The chosen α values were obtained from visual evaluation of the registration results based on smoothing requirements; for all registrations the values were 250.0, 150.0, and 150.0 for each scale, respectively.

### 2.1.3 Patient Enrolment

With the exception of lung SBRT, patients who received lung RT with daily CBCT image guidance between January 2012 and September 2013 were eligible for this study, as approved by the Hamilton Health Sciences Research Ethics Board.

Two groups of patients were analyzed. Group A consisted of 18 patients with a total of 78 treatment fractions. These data were used to carry out Project 1: Assessment of ITV Coverage (hypothesis 1). Group B consisted of 16 patients with a total of 251 treatment fractions. These data were used to conduct Project 2: Simulations to Optimize Lung IGRT Protocol Parameters (hypothesis 2). All subjects in Group B were also in Group A. Table 2.1 shows subject demographics, including dose fractionation, treatment type, tumour location, and ITV size.

Table 2.1. Subject Demographics

| Parameter | n or Mean ± SD [range] Group A | Group B |
|---|---|---|
| Subjects | 18 | 16 |
| Total number of fractions | 78 | 251 |
| Treatment Modality | | |
| 3DCRT | 3 | 2 |
| IMRT | 15 | 14 |
| Dose fractionation | | |
| 45 Gy / 15 fractions* | 1 | |
| 50 Gy / 20 fractions | 1 | 1 |
| 52.5 Gy / 15 fractions* | 4 | 4 |
| 60 Gy / 15 fractions* | 1 | 1 |
| 63 Gy/ 30 fractions | 11 | 10 |
| Tumour Location | | |
| Right Lung / Left Lung | 12 / 6 | 10 / 6 |
| ITV ($cm^3$) | 105.6 ± 82.4 [13.75 - 282.62] | 96.6 ± 80.8 [13.75 - 282.62] |

* Hypofractionated regime
SD, standard deviation; 3DCRT, three-dimensional conformal radiation therapy; IMRT, intensity modulated radiation therapy; ITV, internal target volume

## 2.2 Methods

Common steps between Projects 1 and 2 include automated data import, image preparation, deformable image registration, and region of interest (ROI) coverage quantification. Project 1 investigations only involve analyzing clinical data, whereas Project 2 investigations involve analyzing clinical and simulated data. The overall steps of the methods for this work are summarized in Figure 2.1.

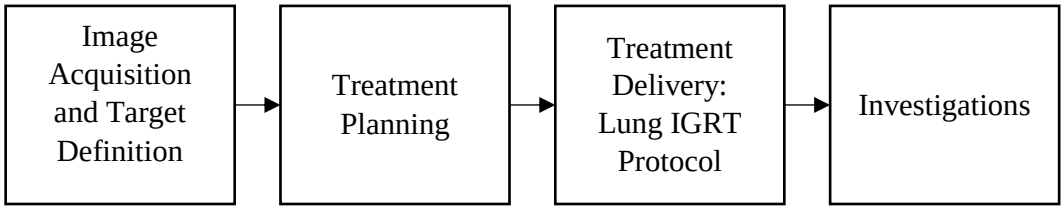


Figure 2.1. Overall workflow to obtain data for investigations.

### 2.2.1 Image Acquisition, Target Definition, and Treatment Planning

A free-breathing, planning CT image (FBCT) was acquired for all patients using a Phillips Brilliance Big Bore CT scanner (Phillips Healthcare, Andover, MA). When tumour motion due to breathing was a concern, a 4DCT was also acquired. Patients were scanned head-first, supine, with hands above their heads, while immobilized using an in-house wing board system. For 4DCT scans the respiratory signal was obtained using the real-time position management (RPM) respiratory gating system (Varian Medical Systems, Palo Alto, CA). The SI borders of the 4DCT image were limited to encompass the GTV with a 2 cm margin as seen on FBCT. This was to limit imaging dose. A maximum intensity projection (MIP) image was generated from the reconstructed 4DCT data-set. All images were reconstructed with a 3 mm slice thickness.

The ITV was contoured by a radiation oncologist using the FBCT image or the MIP, exhale, and inhale images from the 4DCT study. The organs at risk were contoured on the registered FBCT. To account for patient set-up errors and daily anatomical changes, a conservative 10 mm margin was added to the ITV to obtain the PTV. Three-dimensional conformal (3DCRT) or intensity modulated radiation therapy (IMRT) plans were developed using Pinnacle v9.2 (Phillips Healthcare, Andover, MA) with dose computation performed on the free-breathing scan. Plans were typically optimized such that at least 95% of the PTV received 95% of the prescribed dose.

### 2.2.2 Treatment Delivery: Lung IGRT Protocol

All patients were treated on Varian Clinac (Varian Medical Systems, Palo Alto, CA) linear accelerators equipped with on-board imaging (OBI) systems for kV CBCT acquisition. JCC's lung IGRT protocol is shown in Figure 2.2. Daily pre-treatment CBCT images were obtained in low dose thorax mode after initial patient set-up. Two volumetric image registrations were performed. First, rigid image registration of bony anatomy between the pre-treatment CBCT and planning CT was performed with rotations enabled. The clipbox representing bony anatomy consisted of all spinal anatomy visible in CBCT plus 1.5cm margin in all planes. An assessment of bony anatomy was conducted and manual adjustments SI were made, if necessary. Additionally, rotations were assessed. If all rotations along each axis were less than or equal to five degrees, a second rigid registration was conducted using the same clipbox with rotations disabled. The second manual assessment looked at bony anatomy match, visible target to PTV coverage, and discrepancies in external contour for large changes from planning CT to CBCT. The patient was fully re-setup if the translational or rotational differences between planning and treatment exceeded 15 mm or 5 degrees, respectively. Otherwise, translations greater than 2 mm but less than or equal to 15 mm were recorded and a translational couch shift was applied prior to treatment.

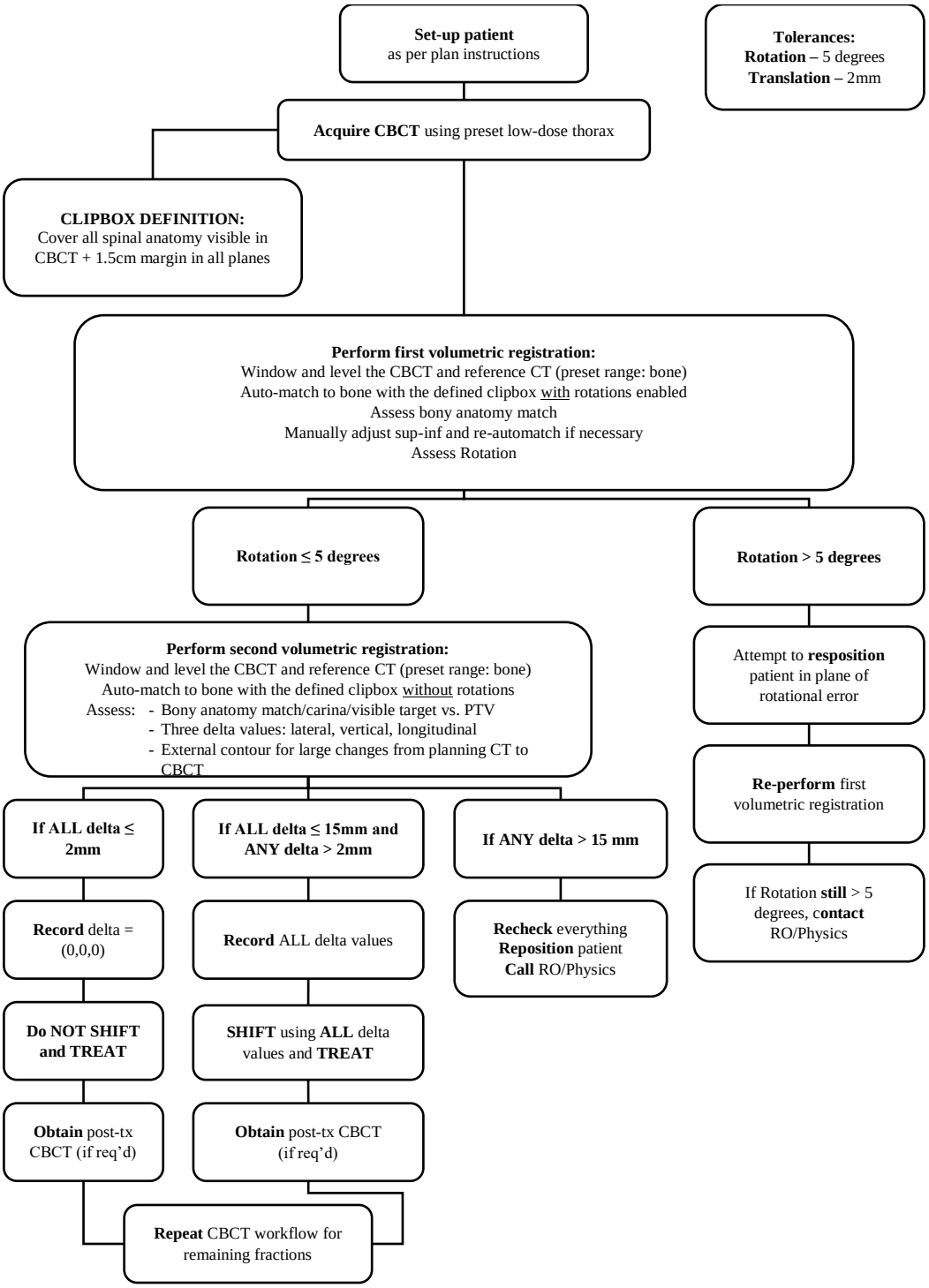


Figure 2.2. Protocol employed for lung IGRT delivery at the JCC.

### 2.2.3 Automated Data Import

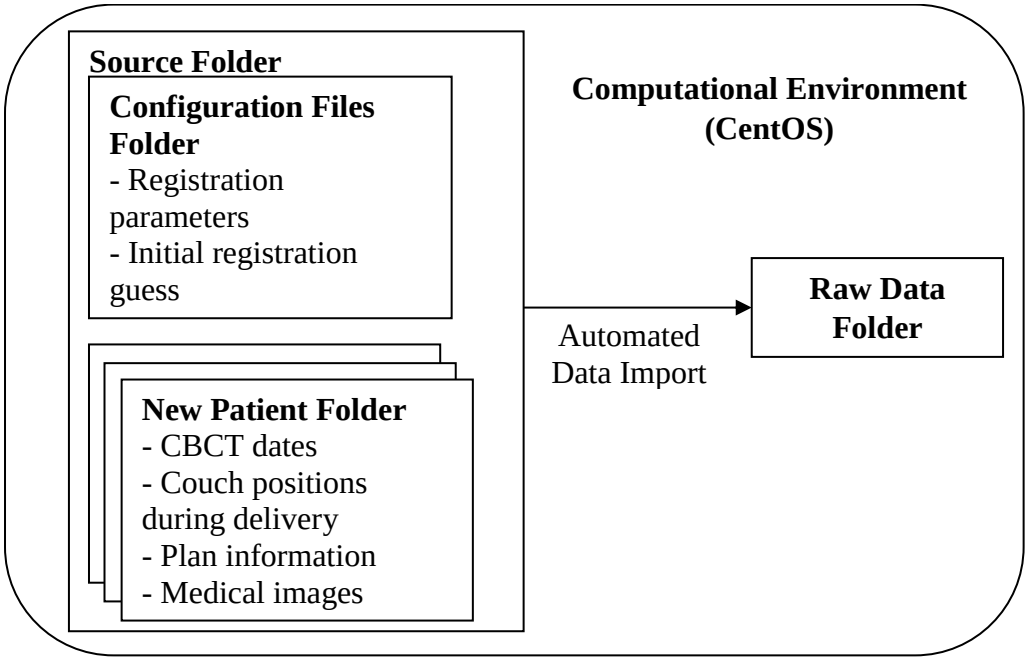


Figure 2.3. Automated data import overview. Raw patient data and configuration information required to carry out investigations are automatically sorted into a working folder in the computational environment.

Python scripts were written to automate raw patient data importing to reduce workload (Figure 2.3). A source folder was available to hold configuration files with an initial guess alignment for the global registration algorithm (initial_shift.txt) and the parameters used for deformable image registration (reg_params.txt). The global registration algorithm accepts an initial guess (in mm) for translations ($t_x$, $t_y$, $t_z$) and rotations ($r_x$, $r_y$, $r_z$) to aid in the alignment of the source image to the target image. The initial guess was only used if the unaided registration was unsuccessful. Data in initial_shift.txt was employed during registration of the average 4DCT image to FBCT image as discussed below. Table 2.2 outlines the parameters in the reg_params.txt file.

Table 2.2. Deformable image registration parameters

| Parameter | Description | Value(s)* |
|---|---|---|
| gridInterp | Interpolation method | B-Spline |
| gridSpacing | Desired, final grid spacing | 10.0 mm |
| minPercents | Amount of data required not to skip node | 50.0, 100.0, 100.0 % |
| similarity | Similarity metric | 4 [MI] |
| bins | Number of bins in joint histogram | 128 |
| maxs | Maximum value in image data | 4095 |
| alphas | Regularization term that controls resistance to deformation | 250.0, 150.0, 150.0 |
| rangeValues | Initial search for optimizer | 10.0, 5.0, 2.5 mm |
| minChanges | Minimum change to continue iteration | 0.01, 0.01, 0.01 mm |
| maxIters | Maximum number of iterations | 10, 10, 10 |
| scales | Number of registration scales | 3 |

*Multiple values indicate separate input for each registration scale
MI, Mutual information

Additionally, inside the source folder were unique patient folders holding the treatment images (FBCT, 4DCT, CBCT) and clinical couch positions set during treatment (tx_couch_pos.csv). Data in tx_couch_pos.csv was transcribed manually from the MosaiQ Radiation Oncology Information System Version 2.4 (Elekta AB, Stockhold, Sweden) and included treatment dates and couch coordinates (vertical, lateral, longitudinal) for each date when CBCT data was acquired. An example of this is shown in Figure 2.4.

| Date | Vert | Lat | Long |
|---|---|---|---|
| 20120508 | 10.4 | 3.5 | 127.4 |
| 20120515 | 10.7 | 3.9 | 126 |
| 20120522 | 10.5 | 4.5 | 129.6 |
| 20120524 | 10.4 | 2.8 | 128.8 |
| 20120530 | 10.6 | 3.3 | 128 |
| 20120606 | 10.4 | 4 | 128.7 |
| 20120619 | 10.3 | 3.3 | 128.6 |

Figure 2.4. Patient-specific file (tx_couch_pos.csv) for available CBCT images containing treatment dates (format: yyyymmdd) along with couch positions during treatment delivery.

An imaging offset was required in cases where there was an increased risk of patient-gantry collision during CBCT acquisition. This was automatically accounted for at the treatment unit by first shifting the couch to the zero lateral position, acquiring the CBCT, then shifting the couch back. Unfortunately, this process sets the lateral couch position to zero for the image, preventing further attempts to reconstruct the position at which the patient was treated. Thus, CBCT DICOM files were checked for date consistency with the couch position file and discarded if an imaging offset was employed to avoid additional processing errors.

For all patients, meshes for each ROI were produced in the TPS to enable further analyses. The conversion from contours to a surface mesh was performed such that the final mesh contained 14 vertices per $cm^3$. This density was determined by computing the ratio of the maximum number of vertices possible in the TPS to the largest ITV volume.

Planning files with information regarding ROIs (plan.roi), isocentre location (plan.Points), Pinnacle version (plan.Pinnacle), and treatment beams (plan.Trial) were included into the patient source folder. All data were anonymized

and moved to appropriately named folders (ie., 0_Raw/Patient_01/Planning for all data related to treatment planning and 0_Raw/Patient_01/CBCT for data collected during treatment) on the CentOS system.

### 2.2.4 Image Preparation

Several pre-processing steps were required to prepare image data for further analysis. First, interesting ROIs were converted into binary images with 1s representing voxels inside the ROI. This was conducted in two steps: (1) producing an edge image from the Pinnacle ROI file; and (2) filling in the edge image. Production of an edge image involves the conversion of Pinnacle world coordinates to image voxel indices based on image spacing and origin. The origin (o) is based on the planning CT image, while image spacing (s) can be customized to a user defined resolution. Conversion from world coordinates (w) to rounded image indices (i) is as follows:

$$[i_x, i_y, i_z] = [\frac{w_x - o_x}{s_x}, \frac{w_y - o_y}{s_y}, \frac{w_z - o_z}{s_z}].$$

These binary images were used to generate volumes of interest (VOI) (or masks) for image registration and to perform geometric expansions to produce PTVs or PRVs. VOIs were produced as a clipbox formed by a 2cm expansion of the ROI binary image in all directions. Figure 2.5 shows an example of a planning CT with an associated ROI binary image along with the ROI registration volume of interest.

(a) (b) (c)

Figure 2.5. Sagittal view of Patient 01 from Group A (a) planning CT image along with binary images of (b) spinal cord ROI and (c) spinal cord VOI used for registration.

Next, DICOM CBCT images were converted to the Pinnacle TPS native format (binary data with text header). Alignment of the CBCT and the planning CT images was achieved by setting the position of the CBCT geometric centre to the planning CT isocentre. Lastly, tri-linear interpolation was employed to resample planning CT images to match corresponding CBCT data. This was necessary to enable similarity metric computation during the image registration process that followed.

Prior to registration, all phases of the planning 4DCT were averaged and aligned to FBCT using global registration. Initial_shift.txt was modified and employed if large discrepancies were observed. Additionally, the aligned averaged 4DCT was supplemented with free-breathing CT intensities outside the field of view. This image depicted a moving tumour as a blurry object (Bradley *et al.* 2006), which corresponded well with data obtained during the long CBCT image acquisition. Improved correspondence between blurred 4DCT and CBCT serves to facilitate intensity-based registration. This blurred 4DCT image is referred to as the planning CT (pCT) image.

### 2.2.5 Assessment of ITV Coverage

The primary aim of the investigations carried out in Project 1 was to obtain an optimized PTV margin based on localized ITVs. Considerations for an optimal margin included its size, benefit of CBCT image-guidance, and geometrical coverage before and after IGRT treatment. These results were compared to the margins obtained using a previously described technique.

#### 2.2.5.1 Investigating ITV Coverage Pre- and Post-Treatment

For each analyzed treatment fraction two CBCT images were available: pre-couch shift (before treatment) and post-treatment (after couch shift). Note, the tx_couch_pos.csv from Section 2.2.3 was not required. The couch shift applied clinically was calculated as the difference between the couch longitudinal, lateral, and height positions stored in the headers of these two images. This shift was then applied to the pre-couch shift CBCT to obtain an image representing corrected patient geometry instantaneously prior to treatment. Thus, for each fraction, three CBCT images were available for analysis: 1. pre-couch shift; 2. pre-treatment (post-couch shift); 3. post-treatment. ITV localization and coverage quantification as were performed on all three scenarios.

Figure 2.6 shows the process of quantifying geometrical target coverage. A localized pCT image accounting for translations, rotations, scaling, and deformations at treatment was obtained using the image registration algorithms described in section 2.1.2. The term “localized” refers to the fact that the pCT image was aligned with a particular CBCT image for a given VOI mask. The resulting transformations were applied to each ITV mesh to obtain a deformed ITV surface representing the target at treatment.

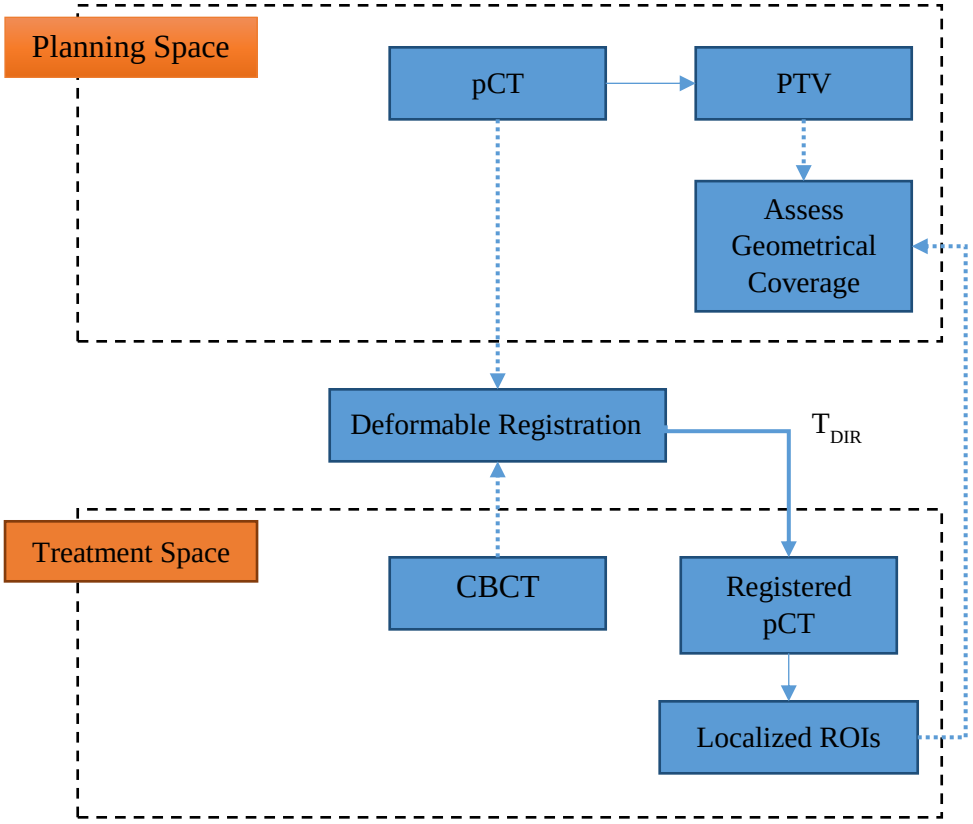


Figure 2.6. Process of obtaining localized ROIs to assess geometrical coverage. $T_{DIR}$ includes the transformations from both global and deformable image registration algorithms. Inputs are represented by dashed arrows and outputs are represented by solid arrows. pCT, planning computed tomography (image); CBCT, cone-beam CT (image); PTV, planning target volume; ROI, region of interest; T, transformation; DIR, deformable image registration.

Ninety-one evaluation margins ranging from 3 to 15 mm in the left-right (LR) and anterior posterior (AP) directions were analyzed, with the superior-inferior (SI) direction at least equal to that of the LR and AP margins. For example, LR and AP margins were held at 5 mm, while SI margins varied from 5 mm to 15 mm. Simulated PTVs represented by binary images were generated with the same resolution as the acquired CT images. The remainder of this thesis will now refer to margins in the following manner: LR, AP, SI; a single value indicates isotropic

expansion in all directions. Success of IGRT was quantified by determining the percentage of the treatment ITV mesh vertices within an evaluation PTV. This coverage metric strictly assessed whether the surface of the ITV was within various evaluation PTVs. Similar approaches were used by Antolak and Rosen (1999) and Redpath and Muren (2005). Antolak and Rosen found that the amount of CTV edge enclosed by the PTV was correlated with a minimum target dose, while Redpath and Muren only considered voxels on the surface in their optimization algorithm for treatment margins around moving and deformable targets. Other advantages for focusing on the target volume edge include the sensitivity of this strategy in ensuring tumour coverage in dose distributions with sharp dose gradients. Coverage mean and standard deviation were calculated for each patient as well as for each margin. Evaluation PTVs were obtained by morphological dilation of the binary ROI images.

Furthermore, the margin that provided a suitable level of ITV coverage over an appropriate percentage of fractions was determined. For this purpose, the situation where 99% of the ITV surface fell within the PTV in 90% of the fractions was considered suitable. This entire method, including patient data import, image resampling and registration, target coverage quantification and statistical analysis was completely automated.

#### 2.2.5.2 Benefit of CBCT Imaging and Effects of Intrafraction Motion

Since the data were non-parametric, a Wilcoxon Signed-Rank test using a tolerance value of 0.05 was performed to determine if ITV surface coverage was

different from pre-couch shift to pre-treatment, and thus, to determine if CBCT image guidance was beneficial for each margin in the analysis. The same statistical test was performed between the pre-treatment and post-treatment coverage results to ensure intrafraction motion was insignificant for the evaluated PTV margin.

#### 2.2.5.3 Optimal PTV Margin

Further analysis was performed with PTV margins that showed significant accuracy improvement when CBCT imaging was employed and demonstrated insignificant losses in accuracy during the treatment fraction. Candidate margins meeting the two above criteria were also required to have at least 99% of each ITV surface within each PTV in at least 90% of the fractions. The optimal PTV margin was identified by comparing the pre-treatment ITV coverage achieved by the candidate margins using a Friedman test (0.05 tolerance) to test for significance between their results. Since the ITV coverage was non-normally distributed, this nonparametric test was chosen to perform analysis of variance using the ranks of ITV coverage data across all appropriate margins. If necessary, additional post-hoc analysis using the Nemenyi test was employed to determine which margins were significantly different from each other.

#### 2.2.5.4 Scaled Target Volume Coverage

Lung tumours are expected to respond to treatment by physically shrinking in size. This type of change can be visually seen on CBCT (Kwint *et al.*, 2014; Lim *et al.*, 2011; Quan, Li, *et al.*, 2012; Lu Wang *et al.*, 2012). The result of using DIR to localize the ITV may result in decreasing volume relative to the original volume

drawn in planning. Typically, PTVs have been clinically designed to assume static target volumes due to uncertainty in contouring all microscopic disease (Weiss & Hess, 2003). For this reason, an investigation was carried out to analyze the deformed targets only with changes in shape. This was achieved by expanding the previously localized ITVs to their original volumes. The scaling factor (S) used was based on the assumption that target volumes were of spherical geometry:

$$S = \left(\frac{V_o}{V_D}\right)^{\frac{1}{3}},$$

where $V_o$ is the original ITV volume and $V_D$ is the deformed ITV volume. The scaling of the localized ITVs by factor S was performed around the ITV centroid. As shown in Chapter 3.2.1, this process was sufficient to recover the original volumes within a percentage error (± standard deviation) of 0.56 ± 0.05% despite the spherical geometry assumption. Analysis of scaled ITV coverage was performed for all data except for the pre-shift situation.

#### 2.2.5.5 PTV Margin Based on the van Herk Margin Recipe

The van Herk margin recipe was utilized by Yeung *et al.* (2009) to analyze the difference between bony and soft-tissue registration, which was their reference standard. Set-up errors used for the margin calculations were defined by subtracting soft-tissue registration couch shifts from bony registration couch shifts along each direction. Instead of limiting the reference standard to only translational shifts from soft-tissue matching, the reference standard utilized for this thesis was defined by the six DOF transformation (translations and rotations) using soft-tissue matching that registered pCT to CBCT. This approach would generate an improvement in the

ideal set-up standard.

In order to fully recognize and account for ITV position and deformation, information from its localized position was utilized to calculate set-up error. This is seen in the work of B. Lu *et al.* (2012) who used deformable image registration between average 4DCT and treatment CBCTs to acquire a localized ITV centroid position. Translational corrections were then determined by aligning centroids of the ITVs between 4DCT and localized CBCT. This strategy was capable of generating optimal dose coverage to tumors and had better consistency relative to conventional soft-tissue and bone matching strategies. In this thesis, PTV margin calculation was determined along each direction using set-up errors calculated by subtracting localized centroid positions $(x', y', z')$ between reference standard ITV (six DOF soft-tissue matching) and pre-treatment ITV (clinical matching) for each fraction:

$$x_{error} = x'_{clincal} - x'_{ref}$$

$$y_{error} = y'_{clinical} - y'_{ref}$$

$$z_{error} = z'_{clinical} - z'_{ref}$$

These modified set-up errors were used to calculate the population systematic and random errors in the van Herk margin recipe described in Section 1.6.2.

### 2.2.6 Simulations to Optimize Lung IGRT Protocol Parameters

Post-treatment images were not required for Project 2 investigations. Two types of simulations were carried out. The first simulation was to investigate the effect of various matching strategies on geometrical coverage. In the second investigation, the effect of rotational tolerance on the success of the lung IGRT protocol was studied.

#### 2.2.6.1 Influence of Matching Strategy

The clinical lung IGRT protocol (Figure 2.2) required manual assessment of the translational corrections obtained by registering the CBCT and planning CT images. The aim of this analysis was to test automated matching strategies with various landmarks; no manual assessments were conducted. A lower limit translational tolerance was still imposed; if all translations along each axis were less than 2 mm, then no shift was employed. Clinical corrections (spinal canal matching with manual assessment) were compared with automated matching of the spinal canal, carina, combination of bone and carina, and soft-tissue (ITV). This required the production of VOI masks specific to these landmarks as previously described in section 2.2.4. Simulated couch shifts (sCS) were obtained by globally registering (three DOF) the pCT to each CBCT using each VOI mask as seen in Figure 2.7.

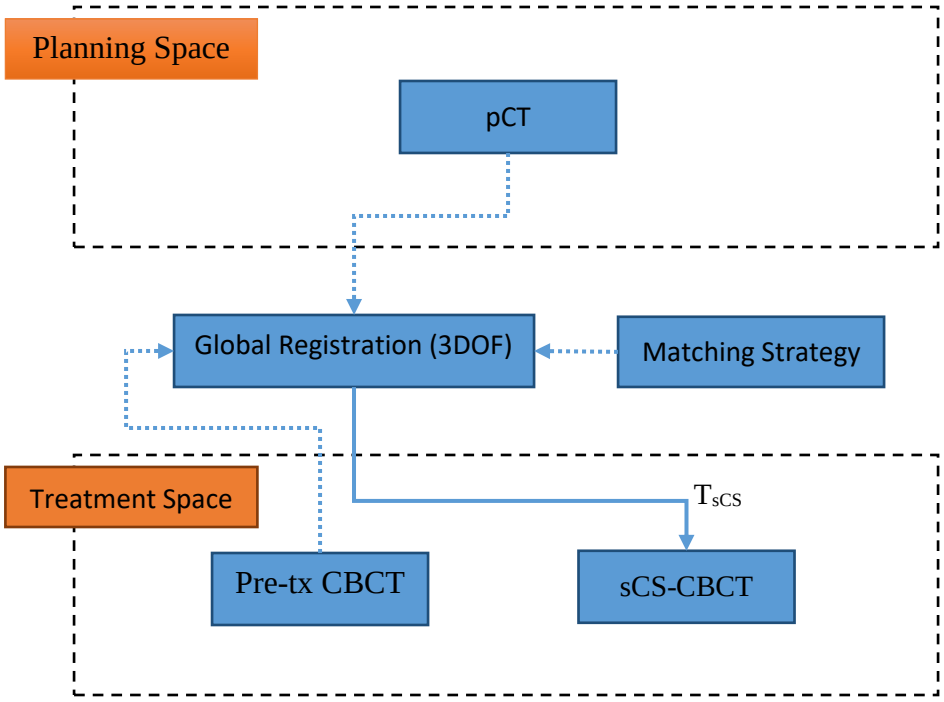


Figure 2.7. Process of obtaining automatic simulated couch shifts using various matching strategies. Inputs are represented by dashed arrows and outputs are represented by solid arrows. DOF, degree of freedom; tx, treatment; sCS, simulated couch shift.

Both ITV and spinal cord geometrical coverage were quantified using localized contours on CBCT images with the appropriate simulated couch shifts (sCS) obtained from the different matching strategies (Figure 2.6). Interesting PTV margins included a relatively small, 5 mm expansion employed elsewhere (Higgins *et al.*, 2011), a 6 mm expansion representing the average used across various cancer centres (Nabavizadeh *et al.*, 2016), JCC's initial 10 mm isotropic expansion, the 6,6,10 mm optimal expansion obtained in Project 1, and various other margins (5,5,8; 7,7,7; and 8,8,8 mm). Spinal cord coverage was evaluated only over the SI region encompassed by the ITV with 2 cm margin. This geometrical analysis of cord coverage was relatively sensitive, as it did not assess the entire cord contour; any part of the cord beyond 2 cm of the ITV SI extensions were ignored, as these

regions are already subject to minimal dose. Interesting PRV margins around the cord included isotropic expansions from 0 to 6 mm. For each margin, a Friedman test was carried out to test for significant differences in ROI coverage between the various matching strategies. This entire investigation was also carried out using volume-maintained ITVs as described in section 2.2.5.4.

#### 2.2.6.2 Influence of Rotational Tolerance

Since patients do not align perfectly during set-up and are only corrected using translational couch shifts, a certain amount of rotational error has to be tolerated. This investigation aimed to determine whether the current rotational tolerance of 5° for conventional lung IGRT was acceptable. Additionally, the effects of automatic translational corrections for simulated rotations based on clinical data was evaluated. Clinical data consisted of the planning CTs, treatment CBCTs, and observed rotational errors. Clinically observed rotational errors can be obtained from the first volumetric image registration conducted in the lung IGRT protocol (6 DOF registration). Since these rotations were not recorded in practice, this registration step was performed using the spinal cord landmark (as performed clinically). For all available treatment fractions, the rotations from the six DOF transformation (cROT) were computed using the global image registration algorithm described above.

The process to simulate the effect of geometrical coverage due to rotations is seen in Figure 2.8. In this approach, perfect set-up scenario CT (PSCT) images were obtained by applying cROT to align pCT to each CBCT using the spinal canal matching strategy; there was a PSCT for every treatment fraction. Determining

rotations with an alternative matching strategy such as soft-tissue may be difficult due to the spherical nature of ITVs; good alignment is still possible even if ITVs are rotated. Rotations of each PSCT (rPSCT) with respect to the cord centroid were generated based on random sampling of cROT using a Gaussian distribution. Four rPSCTs were generated for each treatment fraction to increase statistical power. For each rPSCT, the second volumetric image registration step (rotations off) in the lung IGRT protocol was simulated using the various matching strategies described in section 2.2.6.1. In each case, this produced a translational correction between rPSCT and its respective CBCT image. Again, simulated couch shifts to account of rotational error (sCS-R) were only employed if all translations along each axis were less than 2mm.

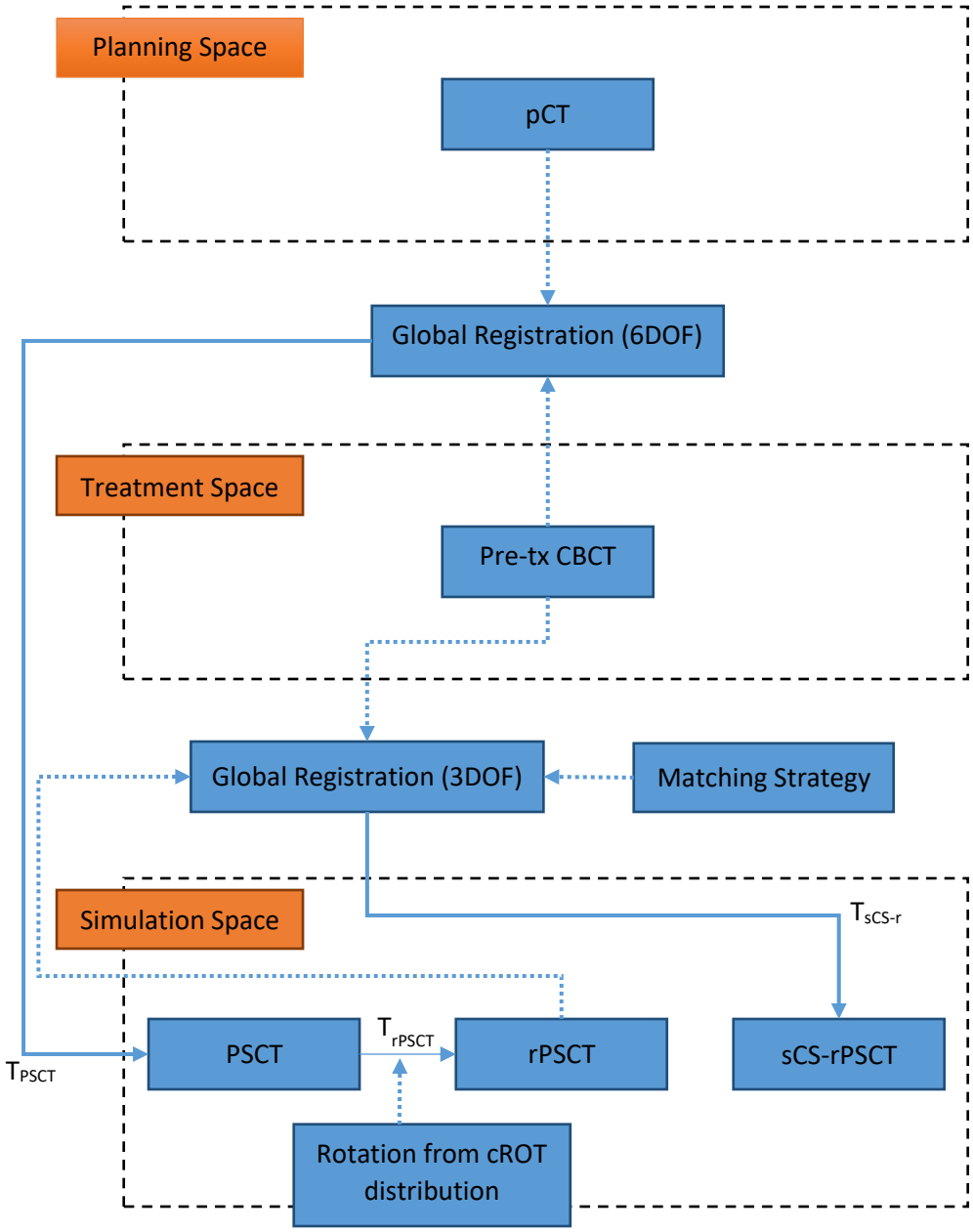


Figure 2.8. Process to simulate corrections for simulated rotational errors in order to assess the rotational tolerance in an IGRT protocol. The global registration algorithm was employed to obtain PSCT image and sCS. Inputs are represented by dashed arrows and outs are represented by solid arrows. PSCT, perfect set-up computed tomography (image); rPSCT, rotated perfect set-up computed tomography (image); sCS-r, simulated couch shift (for rotational error); cROT, clinical rotations

To quantify geometrical coverage, analyses of localized ROIs needed to be

conducted in the original planning space. To investigate coverage back in the planning space, the inverses of transformations $T_{sCS\text{-}r}$, $T_{rPSCT}$, and $T_{PSCT}$ were applied to localized ROIs obtained from DIR. In this manner, geometrical coverage resulting from translational correction of each localized (and rotated) ROI can be analyzed relative to expansions of the original planning volumes.

#### 2.2.6.3 Dose Reconstruction

The majority of this work focused on quantifying geometrical coverage using IGRT. An additional dose reconstruction method to understand the relationship with a purely geometric approach was performed. One such dose reconstruction method involves calculating dose on daily anatomy and registering it back to the planning dataset (Godley, Ahunbay, Peng, & Li, 2012). A cumulative dose can be obtained by summation of computed, registered dose grids across available treatment fractions. To avoid issues of dose computation on CBCT due to inaccuracies of HU from beam scattering, dose computation was conducted on original planning CT dataset that was deformed to each treatment CBCT (Dona Lemus, 2012). The following steps outline the process that was used to obtain reconstructed dose on a single fraction for three patients.

Direct comparison of geometrical and dosimetric IGRT success analyses required the use of the same PTV margin for both techniques. Thus, a treatment plan was optimized with the optimal PTV margin obtained in Project 1, with the objective of delivering at least 95% of the prescription dose to 95% of the PTV (planDR). The automatic translational shift using bone matching was applied to the

previously generated deformed planning CT image used to localize the ITV on the pre-treatment CBCT and then imported into the TPS. Dose was computed with planDR treatment beams based on the Adaptive Convolve algorithm, resulting in a deformed dose grid (dDG). The dDG was exported and inverse transformed to the original CT geometry to represent the dose delivered under simulated image guidance. This modified dDG was then exported back into the TPS where DVHs of original ROIs (e.g., ITV) can be evaluated (now based on deformed anatomy). A mesh of the isoline that corresponded with 95% of the prescribed dose was created in the TPS, exported to the workstation, and converted into a binary image. Direct comparison of the dosimetric analysis to our geometric coverage was carried out by quantifying the percentage of original ITV surface points within the generated isoline. In this analysis, comparisons can only be made with the PTV margin of the treatment plan using automatic bone matching.

# Chapter 3

# Results and Discussion

This work presented a method for direct evaluation of ITV coverage in conventionally fractionated radiotherapy for advanced stage lung cancer delivered under daily CBCT guidance. High geometric accuracy and reduced PTV margins can be achieved with target localization using IGRT for non-small cell lung cancer (NSCLC) patients (Bissonnette *et al.*, 2009). Quantification of geometrical accuracy is crucial to ensure that adequate coverage is achieved in practice. Several other studies (Bissonnette *et al.*, 2009; Grills *et al.*, 2008; Yeung *et al.*, 2009) estimated systematic and random errors to enable PTV margin optimization. This thesis presented methods for quantifying the mean ITV coverage and the percentage of coverage achieved in a fraction of treatments based on retrospective DIR of actual patient data. While the process is entirely automated, human assessment of DIR accuracy is necessary. This technique may be used by a new treatment centre to optimize PTV margins using IGRT data acquired with an initial patient population. For established centres, the process can be used to understand the impact of process changes such as a new immobilization device on treatment accuracy, or for periodic end-to-end type quality assurance of IGRT. The PTV margin obtained using this method was optimized in that image guidance remains effective in improving targeting accuracy while safely containing patient motion during treatment.

## 3.1 Assessment of ITV Coverage

Project 1 tested and developed the technique using data from 18 previously treated lung cancer patients. A typical result obtained when registering a planning ITV to CBCT data acquired before treatment (before couch shift) is shown in Figure 3.1. The image intensities associated with the ITV were clearly misaligned between the planning (a) and CBCT (b) axial slices; nevertheless, the DIR algorithm was able to accurately localize the ITV contour as demonstrated on the deformed planning image (c). DIR performance was assessed with a radiation oncologist who manually checked whether the results were acceptable in a subset of cases.

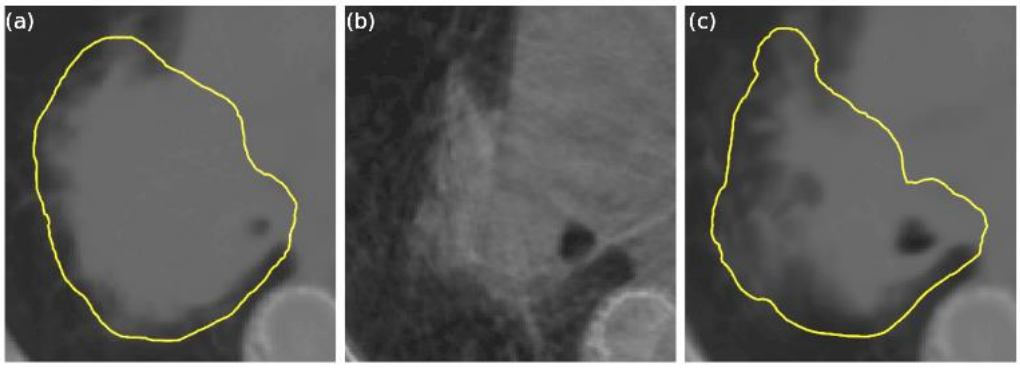


Figure 3.1. Result of deformable image registration for patient 1, fraction 1. Axial slices from (a) 4D planning image with planning ITV, (b) pre-couch shift CBCT with no ITV, and (c) deformed planning image with treatment-specific ITV.

Figure 3.2 shows an assessment of target coverage. The planning contour and an example 5 mm margin PTV are shown in Figure 3.2(a). Figure 3.2(b) shows the ITV as localized using DIR on the pre-treatment CBCT image (prior to couch correction). Figure 3.2(c) demonstrates the pre-treatment ITV after the couch correction. Lastly, Figure 3.2(d) shows the ITV as localized using DIR on the post-treatment CBCT image. This example illustrated a case where the image-guided couch shift improved geometrical coverage (b vs. c and d); however, a percentage

of the ITV was still outside the PTV before and after treatment with this example 5 mm PTV margin.

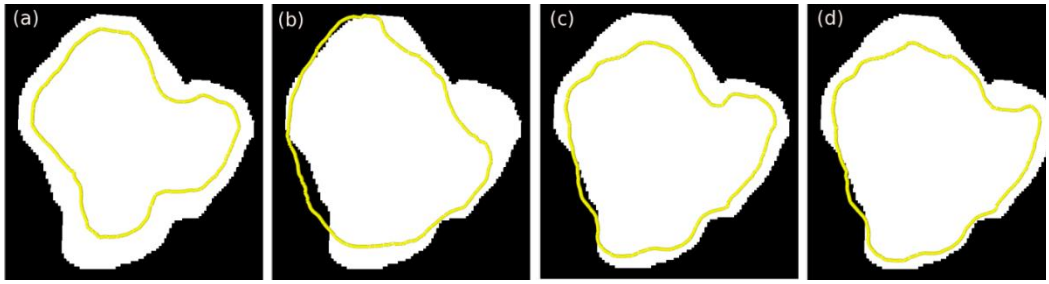


Figure 3.2. Assessment of tumour coverage following the localization of the ITV onto the three treatment scenario CBCT images of Patient 1, fraction 1. (a) Original planning ITV expanded by a 5 mm isotropic margin to obtain the PTV. (b) Adapted ITV following initial setup showing deformation and a geometric miss (pre-couch shift scenario). (c) Adapted ITV following couch correction showing reduced geometric miss (pre-treatment scenario). (d) Adapted ITV following treatment completion showing similar coverage to c (post-treatment scenario).

The mean percentages of ITVs covered across the 18 patients in Group A for various PTV margins are shown in Table 3.1. As expected, the improvement in mean ITV coverage between initial patient set-up to couch correction decreased as the margin increased.

Table 3.1. Mean ITV coverage ± standard deviation during pre-couch shift, pre-treatment, and post-treatment scenarios for PTV margins based on 78 fractions. Significant improvement with IGRT was seen for the listed margins.

| PTV Margin (LR, AP, SI mm) | Mean ± Standard Deviation of ITV Coverage (%) | | |
|---|---|---|---|
| | Pre-Couch Shift | Pre-Treatment | Post-Treatment |
| 5,5,5 | 88.8 ± 13.5 | 98.1 ± 4.4 | 96.5 ± 6.8 |
| 6,6,6 | 91.7 ± 11.4 | 98.9 ± 3.1 | 98.0 ± 4.8 |
| 6,6,10* | 94.5 ± 8.8 | 99.5 ± 2.0 | 99.1 ± 3.1 |
| 7,7,7 | 93.9 ± 9.5 | 99.4 ± 2.1 | 98.8 ± 3.5 |
| 8,8,8* | 95.7 ± 7.4 | 99.6 ± 1.4 | 99.3 ± 2.4 |
| 9,9,9* | 97.3 ± 5.2 | 99.8 ± 0.9 | 99.7 ± 1.2 |
| 10,10,10* | 98.3 ± 3.8 | 99.9 ± 0.6 | 99.9 ± 0.6 |

* Margin capable of encompassing intrafractional variation as shown by insignificance of a Wilcoxon signed rank test ($p > 0.05$) between pre- and post-treatment ITV coverage.

Figure 3.3 shows the percentage of treatment fractions for all three scenarios (pre-shift, pre-treatment, post-treatment) where at least 99% of the ITV is within the PTV for isotropic margins between 3 mm to 15 mm, and an anisotropic margin of 6,6,10 mm in the LR, AP, SI directions, respectively. The increase in targeting success with image-guidance can be observed by comparing the results obtained with the initial set-up (dark grey bars) and couch shift (white bars). Furthermore, the amount of intrafractional variation can be observed by comparing the pre-treatment (white bars) versus the post-treatment results (light grey bars). As also shown in Table 3.1, there is a significant loss in targeting accuracy due to intrafraction motion for isotropic margins less than 8 mm. Figure 3.3 reveals the sensitivity of margins in achieving sufficient ITV coverage with an acceptable frequency. For instance, the isotropic 7 mm margin was able to achieve sufficient ITV coverage in 90% of the fractions with the employed clinical shifts (pre-tx) but fell short in the post-treatment scenario, while the isotropic 8 mm margin successfully covered the ITV in at least 90% of the fractions in both scenarios. This

example highlighted the impact of how small differences in PTV margins on the order of 1 mm can affect overall target coverage.

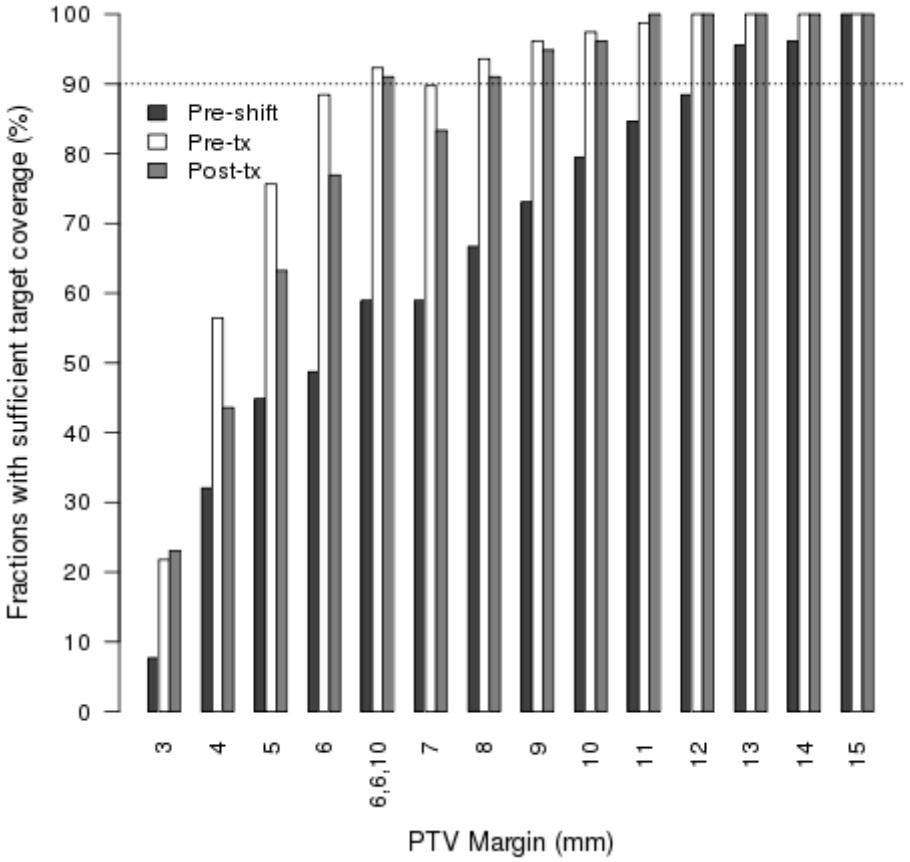


Figure 3.3 Percentage of CBCT images for the pre-shift, and pre- and post-treatment scenarios where sufficient ITV coverage was met for isotropic PTV expansions from 3 to 15 mm and an anisotropic expansion of 6,6,10 in the left-right (LR), anterior-posterior (AP), superior-inferior (SI) directions respectively. Sufficient coverage is met when at least 99% of the ITV fell within the PTV.

Figure 3.4 depicts ITV coverage (following couch correction) for a small PTV margin (5 mm), the clinical employed margin (10 mm), and two significant margins (6,6,10 mm and 8,8,8 mm). These two significant margins benefited from image-guidance, maintained targeting accuracy during treatment, and achieved 99% ITV coverage in at least 90% of the fractions. The minimum percentage of

ITV covered at any fraction was approximately 78, 87, 91, and 95 percent for the (5,5,5), (6,6,10), (8,8,8), and (10,10,10) mm margins, respectively.

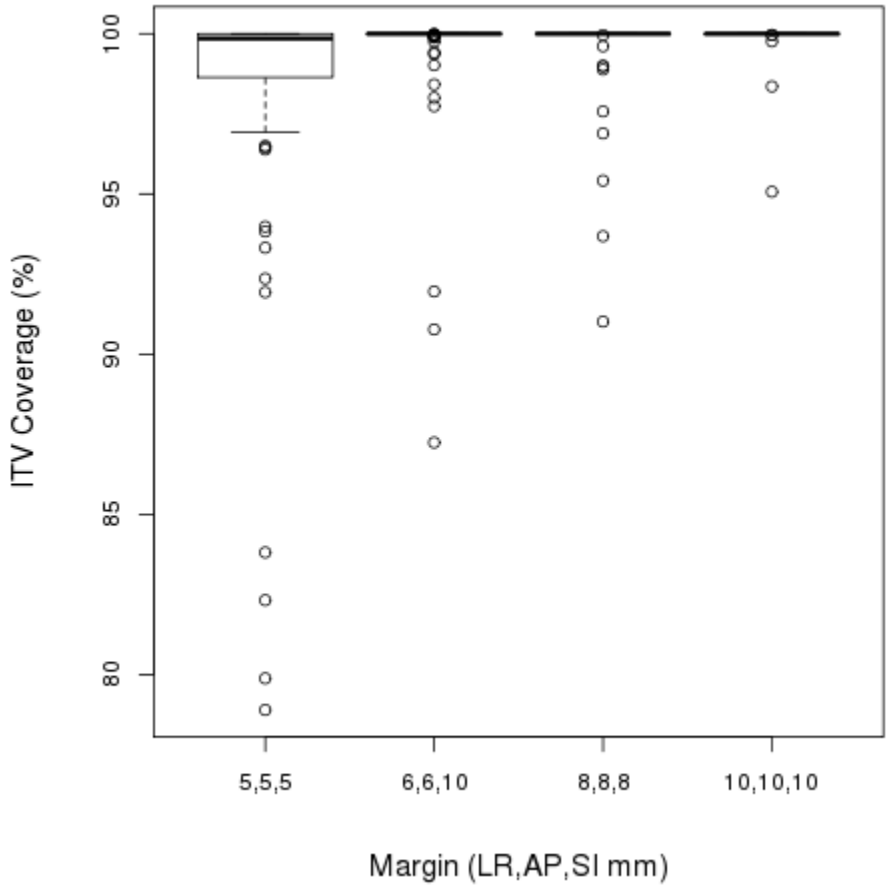


Figure 3.4. Box-and-whisker plot showing ITV coverage for pre-treatment CBCT images for various PTV margins. The bottom and top of the box respectively represent the first and third quartiles (interquartile range), and the band inside the box represents the second quartile (median). The whiskers represent the ITV coverage within 1.5 times the interquartile range.

Target coverage was also assessed while maintaining initial ITV size through treatment. The comparison between pre-treatment coverage with and without ITV size changes is shown in Figure 3.5 below. Similarly, coverage for volume-maintained ITVs was assessed between pre and post-treatment CBCT images (Figure 3.6). The scaling factor employed to maintain volume assumed that

ITVs were spherical. This was deemed appropriate since the scaled volumes were within 0.56 ± 0.05% (standard deviation) of the starting volumes.

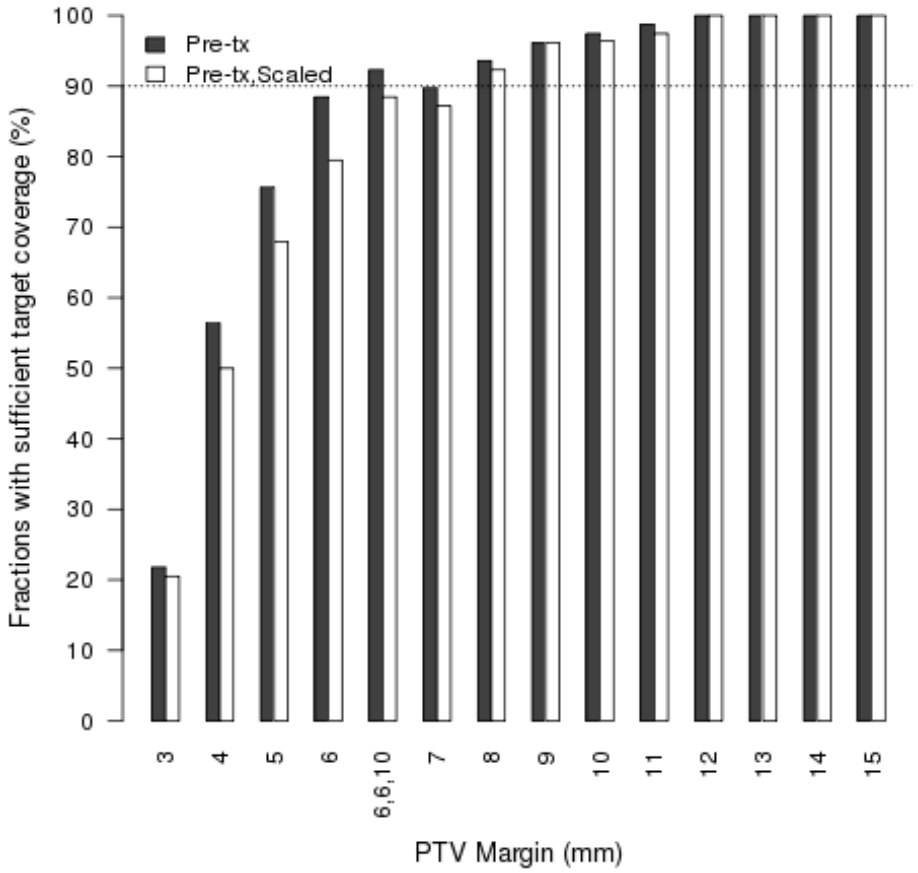


Figure 3.5. Comparison of coverage for volume-maintained (scaled) vs. varying ITVs. Percentage of pre-treatment CBCT images where sufficient ITV coverage was met for isotropic PTV expansions from 3 mm to 15 mm and an anisotropic expansion of 6,6,10 mm in the LR, AP, SI directions respectively. Sufficient coverage was met when at least 99% of the ITV fell within the PTV.

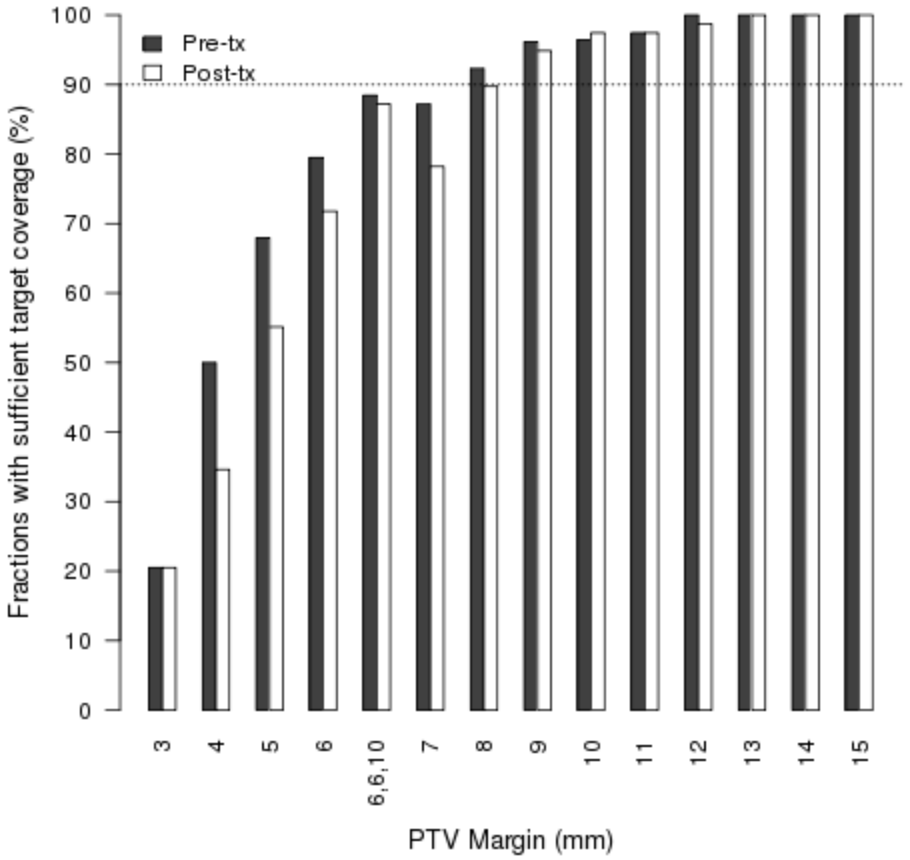


Figure 3.6. Comparison of coverage for volume-maintained ITVs at pre-treatment (with couch correct) and post-treatment. Percentage of pre-treatment CBCT images where sufficient ITV coverage was met for isotropic PTV expansions from 3mm to 15mm and an anisotropic expansion of 6,6,10 mm in the LR, AP, SI directions respectively. Sufficient coverage is met when at least 99% of the ITV fell within the PTV.

These results indicate that the 10 mm PTV margin ensures image guidance is beneficial and that patient motion during treatment is contained. While there is sufficient evidence to support margin reduction, attempting to achieve full ITV coverage in 100% of the treatment fractions is unwise as an unreasonably large margin of 15 mm would be required as seen in Figures 3.3, 3.5, and 3.6. Lastly, this analysis highlights the importance of deciding on the acceptable percentage of fractions where full target coverage does not have to be achieved.

The situation where at least 99% of the ITV is covered by the PTV in 90% of the fractions was considered an acceptable level of overall treatment accuracy. As shown in Figure 3.3, this criterion was achieved with several PTV margins less than 10 mm. Figure 3.3 also emphasizes the importance of CBCT image guidance and intrafractional variation. With image guidance, the 10 mm margin covered ≥ 99% of the ITV in 96% of fractions with a mean ITV (± standard deviation) coverage of 99.8 ± 1.1%. Five and eight mm isotropic margins were successful 75% and 92% of the time, respectively. The evaluation of anisotropic margins found that the 6,6,10 mm margin was successful in 91% of the fractions. For each margin, two Wilcoxon sign rank tests were performed to compare ITV coverage pre-couch shift versus pre-treatment, and pre-treatment versus post-treatment. The first scenario indicated whether IGRT was successful in improving targeting while the second scenario indicated whether intrafraction motion occurring during treatment was significant. With the 5 mm margin, IGRT improved coverage pre-treatment significantly, but coverage decreased significantly during treatment due to intrafraction motion. This is in contrast to the zero geometrical misses using a 5 mm PTV margin observed by Higgins *et al.* (2009). This difference may be due to the ability of the DIR approach to detect smaller geometrical changes compared to the rigid registration analysis used by Higgins *et al*. With the 8 mm isotropic, 6,6,10 mm, and 10 mm isotropic margins, IGRT significantly improved coverage and did not decrease significantly during the treatment. This analysis assumed that any internal motion during the couch shift was insignificant and that all intrafractional variation was captured in the after treatment image.

As discussed above, the 6,6,10 mm and 8 mm margins met the coverage criterion and demonstrated both an IGRT benefit and insignificance of intrafraction motion. Figure 3.4 depicts the extent of ITV miss following image guidance. The anisotropic margin resulted in 3/78 (3.8%) fractions with < 95% coverage compared to 2/78 (2.5%) for the isotropic margin. At this point, either margin may be considered as optimal but the non-isotropic option was chosen since it reduces the irriadiated volume towards OARs such as spinal canal and esophagus. A Friedman test revealed significant difference between these two margins, the 5 mm margin, and the clinically employed 10 mm margin (F-value=34.93, $\chi^2_{0.05}(df = 3) = 7.815$, $p < 0.01$). The Nemenyi post-hoc test revealed that the only significant pairs were those with associated with the 5 mm margin. The minimum coverage using the 6,6,10 mm margin was 87%. A careful analysis of this fraction indicated that the low coverage was a result of a couch correction that aligned bony anatomy without focusing on carina matching. Various thoracic registration landmarks have therefore been an interest of study in lung image-guided therapy (Grams, Brown, *et al.*, 2014; Higgins *et al.*, 2011; Yeung *et al.*, 2009) and are explored in the Sections 3.2.1 and 3.2.3.

Compared to the 6,6,10 mm PTV margin, a similar margin of 5.1, 6.9, 13.9 mm was calculated by Yeung *et al.* (2009) using a margin recipe (van Herk *et al.*, 2000) that incorporated the analysis of 289 CBCT scans from 13 patients. Using the setup errors for patients in Group A with a common margin recipe that considers the small population size produced a required margin of 3.1, 4.1, 5.1 mm as shown in Table 3.2. This calculated margin was slightly greater than the 4, 4, 3 mm PTV

margin calculated by Bissonette *et al.* (2009) for conventional lung IGRT with manual couch correction following spine alignment. Despite differences between the calculated margin in this thesis and that found by Yeung *et al.*, we both found that an anisotropic margin would be necessary with greater expansion in the SI direction. Differences in margin calculations using the recipe can be attributed to the modification in the soft-tissue reference standard and definition of set-up error; rotations were included in the registration and set-up error involved ITV centroid positions. Additionally, matching strategies have an impact on PTV margins. Yeung *et al.* quantified error of bone matching relative to soft-tissue, while this thesis quantified the soft-tissue vs clinical match which entailed bone matching along with carina and ITV assessments. The visual assessment of ITV to ensure that it was within the PTV allowed for the smaller calculated margins. Furthermore, error in this work was computed by subtracting localized ITV centroids (reference with six DOF soft tissue matching vs. clinical match). This approach ignores the fact that the planning ITV centroid may be in a different position compared to the treatment ITV due to shape changes on treatment alone. However, since advanced lung cancer targets are typically large, shape changes are unlikely to induce large changes in centroid position. Nevertheless, this calculated margin would be subjected to significant geometric miss. As previously discussed, isotropic margins less than 7 mm did not meet the frequency requirement for sufficient target coverage using the clinical matching strategy, and were affected by intrafractional motion (Figure 3.3). The analysis presented in this thesis addressed the geometric sensitivity of PTV margins. Quantification of set-up error even in the presence of

deformation revealed a relatively small margin calculation compared to the proposed 6,6,10 mm margin. The target centroids used in the error calculations are relatively stable points in a sense that there is less movement compared to the edges of the ITV. The analysis also accounted for changing ITV sizes. The suitable margins (8 mm or 6,6,10 mm) were still larger than those calculated from the margin recipe. The method presented in this thesis may therefore be a useful alternative to analyzing systemic and random error to assess required margins.

Table 3.2. Set-up errors and required margins for CBCT clinical registration (3 DOF bone matching; ensure ITV within PTV) compared with the reference standard obtained using 6 DOF soft-tissue registration. Corrections for the small population size are given in the systematic error ($\Sigma'$) and final corrected margin (Margin') rows.

| Variable | LR (mm) | AP (mm) | SI (mm) |
|---|---|---|---|
| $M$ | -0.07 | -0.64 | -0.46 |
| $\Sigma$ | 1.1 | 1.4 | 1.8 |
| $\sigma$ | 1.5 | 1.1 | 1.9 |
| $\Sigma'$ | 0.8 | 1.3 | 1.5 |
| *Margin* | 3.8 | 4.3 | 5.8 |
| *Margin'* | 3.1 | 4.1 | 5.1 |

Negative mean (M) values indicate reference centroids were left, posterior, or inferior relative to clinical centroids.

A critical assumption in this work was that successful treatment is achieved when at least 99% of the ITV is covered in at least 90% of fractions. As discussed by Harsolia *et al.* (2008) analyzing the percentage of CBCTs with at least 99% ITV coverage under image guidance addresses issues of interfractional uncertainties caused by both shifts in the intrathoracic structures and set-up error. These interfractional uncertainties are of greater importance than controlling the intrafractional motion, also addressed in this study. Furthermore, the definition of

treatment success used in this thesis appears to be conservative compared to the results of van Sörnsen de Koste *et al.* (2001), who showed sufficient dosimetric coverage is achieved even if geometrical coverage is less than 99% in radiotherapy of stage I NSCLC. Accepting a one percent miss acknowledges possible limitations in the accuracy of localizing the ITV but small misses have been justified in previous literature. The PTV margin recipe (van Herk *et al.*, 2000) that was compared in this work ensured that a minimum dose of 95% to the CTV was achieved for 90% of the patients. Another recipe proposed by Stroom, De Boer, Huizenga, & Visser (1999) ensured that at least 95% of the dose was delivered to at least 99% of the CTV (on average). With regards to the frequency of achieving a desired level of treatment accuracy, a study conducted by Gukenberger *et al.* (2007) proposed a PTV margin such that intrafraction motion was less than 2 mm in 90% of all fractions. Likewise, Bell *et al.* (2015) proposed an optimized PTV margin for post-prostectomy IMRT based on bony anatomy matching with a geographic miss rate of 9.3% (or success rate of 90.7%). Thus, the objective of ensuring adequate geometrical coverage in at least 90% of the fractions seems reasonable.

Several studies demonstrated the clinical relevance of image guidance through improved tumour targeting and decreased PTV margins (Bissonnette *et al.*, 2009; Haasbeek, Slotman, & Senan, 2009; Lu Wang *et al.*, 2012; Wong *et al.*, 1999). Results of this thesis indicated that, aside from the 15 mm isotropic margin, all evaluated margins benefitted from CBCT image guidance. Other studies have demonstrated improvement in the planned dose value to the GTV (Lu Wang,

Feigenberg, Chen, Pasklev, & Ma, 2006) and reduction in mean lung dose (Grills *et al.*, 2008; Harsolia, Hugo, Kestin, Grills, & Yan, 2008) under image guidance. Further analysis should now consider whether reducing the current PTV by as much as 4 mm in the LR and AP directions is important. Although patient-specific, a reduction in PTV margins by as little as 2 mm has allowed for a range of increased doses to tumours as well as a decrease in the mean heart, esophagus, and lung doses (Nelson, Starkschall, & Chang, 2006). Findings from the Radiation Therapy Oncology Group (RTOG) 0617 trial showed that the standard 60 Gy chemoradiation treatment resulted in superior overall survival compared to the 74 Gy chemoradiation approach for locally-advanced NSCLC (Bradley *et al.*, 2013). However, the protocol for RTOG 0617 did not use a consistent treatment protocol; variations were seen in defining CTV, ITV, and PTV margins. Most significantly, the use of IGRT was not a requirement, so it is possible the trial did not recognize treatments to their full potential (Kilburn *et al.*, 2016). Nevertheless, PTV optimization is an important factor to consider in treatment planning to potentially avoid unnecessary irradiation and reduce normal tissue complication probability (Feng *et al.*, 2009; Marks *et al.*, 2010). For instance, this analysis revealed that the employed 10 mm PTV margin was overly conservative for Patient 4 since all fractions achieved sufficient coverage with a 5 mm margin. However, a 5 mm margin was not appropriate for the majority of the patients. Patient-specific margins therefore become difficult to implement without understanding how and if set-up accuracy, intrafractional motion, and deformations affect overall accuracy.

Tumour regression is common in lung cancer radiotherapy (Jabbour *et al.*,

2015; Lim *et al.*, 2011). Since this method utilized DIR to localize ITV throughout treatment, target volumes were likely smaller in the final fractions. Although regression is common, the reduction of the irradiated volume mid-treatment remains a concern due to uncertainty in subclinical disease (Grills *et al.*, 2008). That is not to say that there is no benefit for adaptive lung radiotherapy (Guckenberger *et al.*, 2011). Although the work of Siker, Tome, and Mehta (2006) caution against routine treatment field reductions due to the uncertainty in the extent of microscopic disease, Guckenberger *et al.* (2011) found that dose to suspect microscopic disease was not compromised when adaptive radiotherapy was employed to shrinking GTVs for locally advanced NSCLC patients. This is in agreement with the study by Grams and Fong de Los Santos *et al.* (2014), who found greater dosimetric consequences related to positional uncertainty versus anatomic changes such as reductions in tumour volumes. Nevertheless, a quantitative analysis of ITV coverage while maintaining the initial planning ITV size throughout treatment was conducted. Figure 3.7 shows the change in ITV volume based on the DIR for Group B patients (since there were more data compared to Group A). The median ITV reduction after approximately 40 days following planning was 9.4% (range, 1.4%-21%). This is considerably lower relative to the values seen in literature based on manual contouring. Jabbour *et al.* (2015) found a mean reduction of 39.3% from day 1 to day 43 CBCT based on 38 patients, while Lim *et al.* (2011) found a mean percent decrease of 51.1% by treatment completion based on 60 patients. In the latter study, contours were only conducted on 31 patients since the primary tumour was peripheral; for the

remaining 29 patients, a subjective assessment was conducted that graded the regression as either less than 10% or greater than 30%. Despite the differences in ITV reduction seen in this thesis, the registration results were still valid according to the radiation oncologist. As shown in Figures 3.5 and 3.6, there was a significant impact ($p < 0.05$) of volume maintenance on margin suitability. This significance was seen for isotropic margins less than 7 mm. The 6,6,10 mm PTV margin also showed a significant difference ($p = .043$) between the volume-maintained and varying volume analyses; successful coverage rate decreased from 91% to 88.5% of fractions. Additionally, this margin became susceptible to intrafractional variation. The overall success rate remained the same for the 8 mm isotropic case and accuracy was maintained during treatment delivery. It should be noted that for 28% of all fractions, the ITV localized using DIR had a greater volume than at planning so volume down scaling actually improved coverage.

(a)

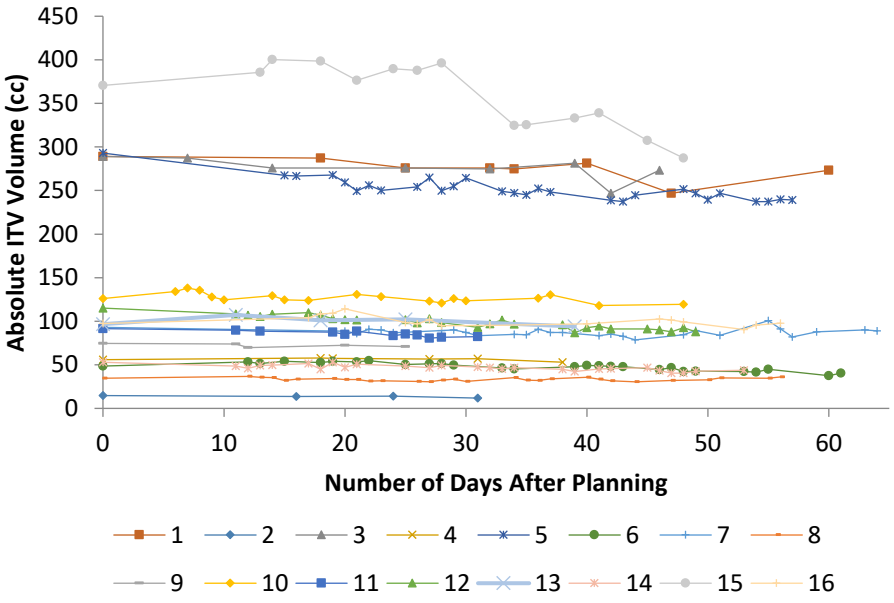


(b)

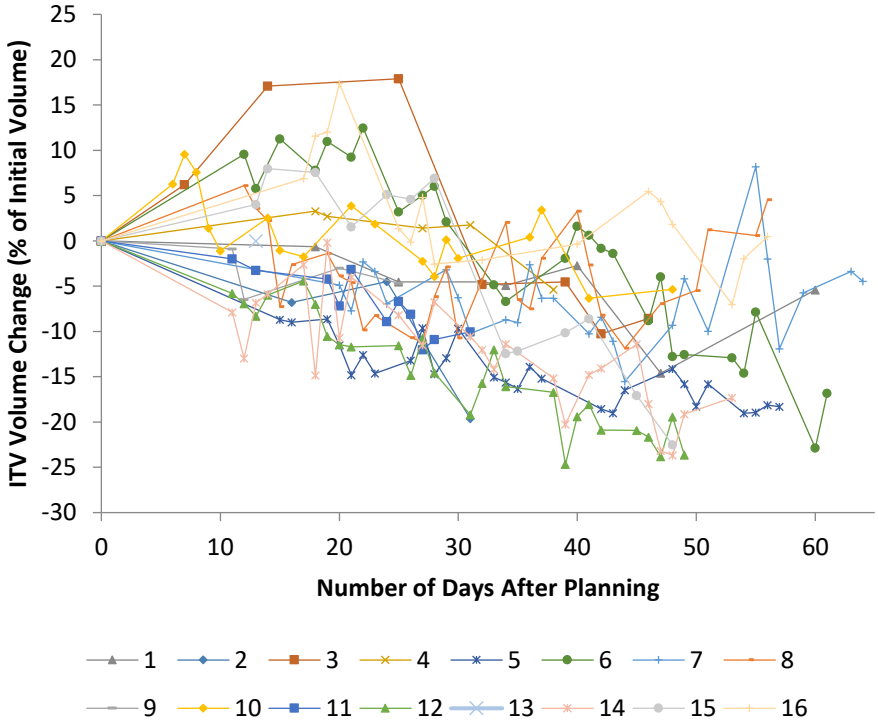


Figure 3.7. Change in ITV size throughout treatment. Deformable image registration between planning CT and pre-treatment CBCT was used to localize treatment-specific ITVs. Changes were quantified in terms of (a) absolute and (b) relative volume.

Accuracy of the employed geometric approach depended on image resolution, registration error, breathing motion, and discretization of the ITV surface. CT images used in this study had 3 mm slices with a corresponding mean registration error of approximately 3 mm in the slice direction (Wierzbicki *et al.* 2004). The differences in institutional-specific protocols for correcting set-up error plays an important role in the outcome of radiotherapy. For instance, JCC`s lung protocol used to generate data for this project relied on matching the spinal canal while visually ensuring the target remained within a 10 mm isotropic margin PTV. Hence, the computed ITV coverage was specific to a uniform 10 mm margin, yet there was still room for margin reduction. Ideally, the reduced, optimized margin from this analysis should be used in clinical practice and more data analyzed to determine if further reductions are possible. Additionally, dosimetric evaluations (Ma *et al.* 2013, Rosu *et al.* 2005, Admiraal, Schuring & Hurkmans 2008) are required to determine the full impact of margin reduction. Error in manually contouring the ITV was ignored in the analysis since it is already ignored in clinical practice (Yeung *et al.* 2009). It also becomes irrelevant in terms of PTV margin optimization using this approach since the 3D tumour shape was tracked. In the event that shape is incorrect, its position and motion are correct, which are the current concerns for PTV margins.

In summary, Project 1 introduced a metric for quantifying geometrical accuracy of localized ITVs obtained through DIR. This process served to review the clinical implementation of a lung IGRT protocol using an in-house immobilization system, a 10 mm PTV margin, spinal cord matching with manual

assessment, and a 5° rotational tolerance. While ITVs consider some intrafractional motion, the results of this project revealed that additional PTV margin is needed to encompass the remainder. This is in agreement to the works of Britton *et al.* (2007) and James *et al.* (2012) who both cautioned the use of a single 4DCT to define the ITV. Overall, PTV margins of 8 mm isotropic or 6,6,10 mm were justified given they ensured daily CBCT image guidance was beneficial, maintained ITV accuracy during treatment, and met an acceptable frequency of adequate ITV coverage. Although the analysis conducted on scaled ITVs relative to the original planning ITVs revealed significance differences ($p < 0.05$) in coverage for the 6,6,10 mm PTV margin, the fraction meeting the acceptability criterion was only 1.5% below the desired 90% level. Additionally, this margin already exceeds the margin calculated using the van Herk margin recipe. It is important to note that the current analysis was carried out on data acquired under a 10 mm PTV margin protocol. It is likely that a reanalysis of new data acquired from patients treated with the 6,6,10 mm margin would improve the outcome given the additional efforts made by therapists in ensuring the ITV is within a smaller PTV.

## 3.2 Simulations to Optimize Lung IGRT Protocol Parameters

The results of Project 2 incorporated DIR along with the geometrical approach used in Project 1 to evaluate the interplay between all parameters in the JCC's lung IGRT protocol, including matching strategies, rotational tolerances, and OAR coverage. Data analysis was conducted on both changing and volume-maintained ITVs from patients in Group B. Figures presented for ITV coverage are only for the changing volume cases. In the following sections, investigations of matching strategy and rotational tolerance are presented, followed by the analysis relating all parameters.

### 3.2.1 Influence of Matching Strategy

In addition to the clinical matching strategy (bone alignment with manual assessment), four other automatic strategies were investigated. These included alignment of bone (spinal column), carina, combination of cord and carina, and soft-tissue (ITV). For 16 patients and a total of 251 CBCTs, both ITV and cord (spinal canal) geometrical coverage were analyzed within various PTV and PRV margins, respectively. The mean coverage per patient for all matching strategies is seen in Figure 3.8, and the percentage of fractions with sufficient coverage is seen in Figures 3.9 and 3.10. Project 1 revealed that the clinically employed 10 mm PTV margin was indeed sufficient in terms of ITV coverage, but could be reduced to either an isotropic 8 mm or a 6,6,10 mm margin. The results of Project 2 are similar to Project 1: successful coverage was achieved in 92% and 91% of the fractions for the 8 mm and 6,6,10 mm PTV margins, respectively, despite the fact that more CBCT images (251 vs. 78) were analyzed.

(a)

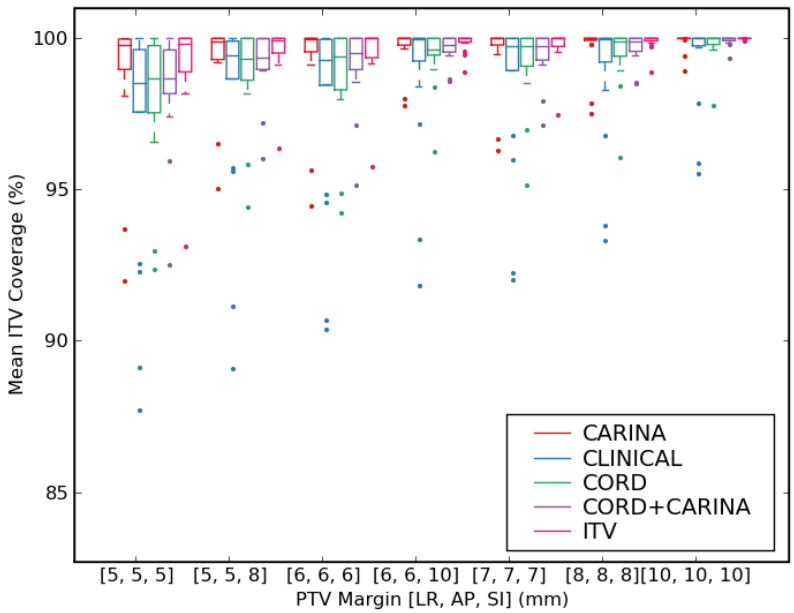


(b)

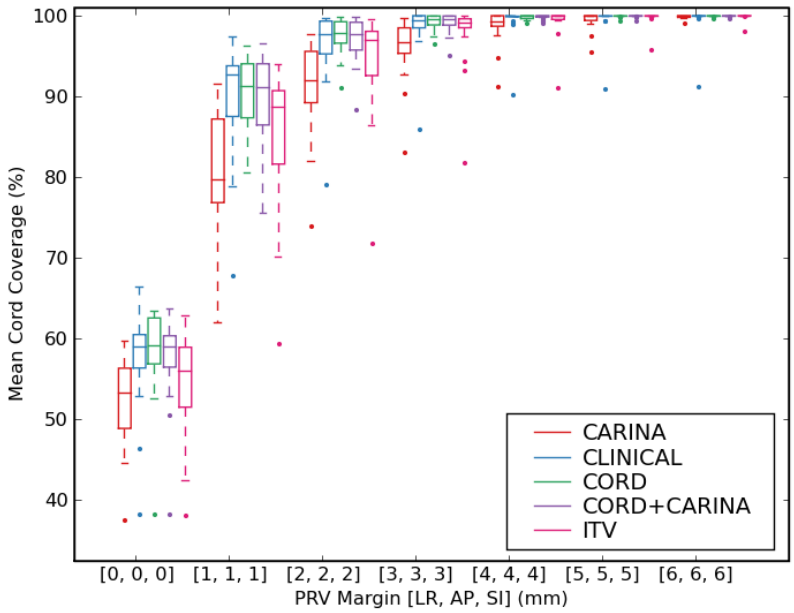


Figure 3.8. Box-and-whisker plots of the patient-specific means of (a) ITV and (b) cord coverage as a function of PTV and PRV margin respectively. The bottom and top of the box respectively represent the first and third quartiles (interquartile range), and the band inside the box represents the second quartile (median). The whiskers represent an observed coverage that was within 1.5 times the interquartile range.

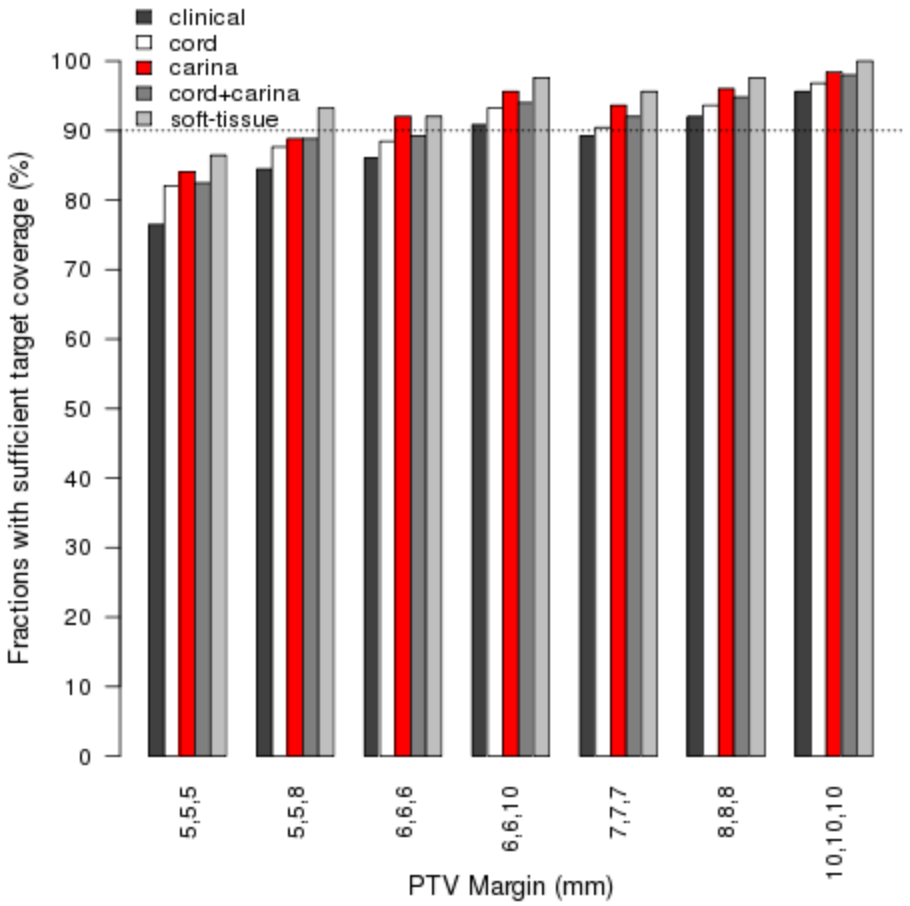


Figure 3.9. Comparison of ITV coverage within various PTV margins following IGRT correction using five different strategies of matching planning CTs with treatment CBCTs. Results represent the percentage of fractions where sufficient ITV coverage was met (at least 99% of the ITV fell within the PTV).

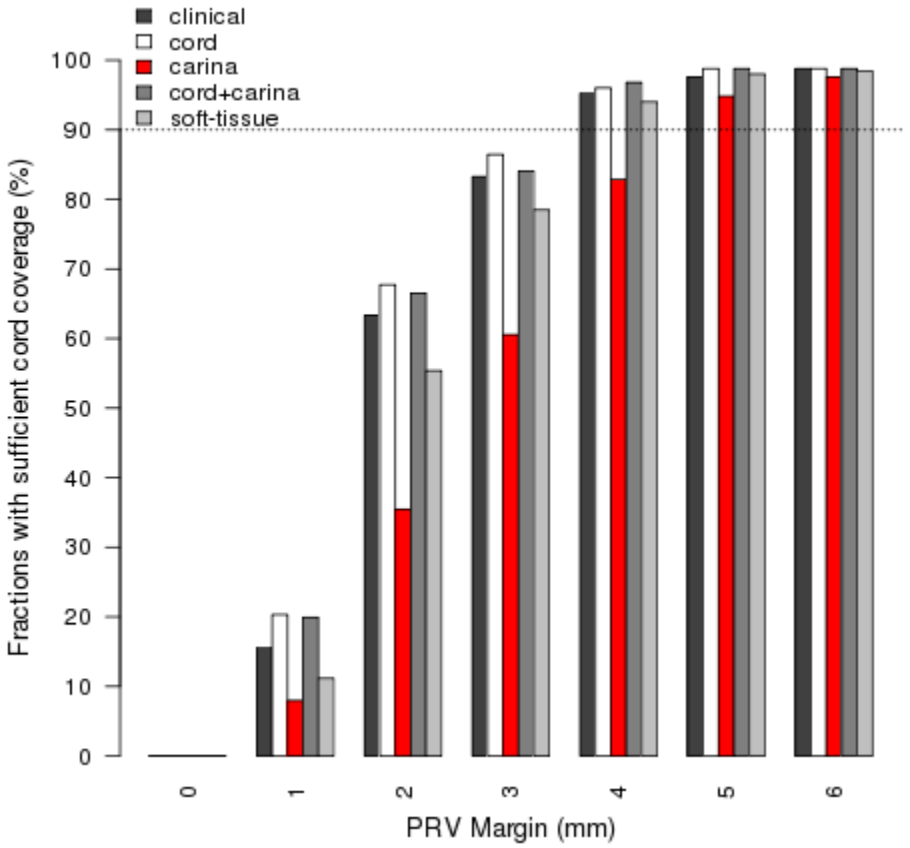


Figure 3.10. Comparison of spinal cord coverage within various PRV margins following IGRT correction using five different strategies of matching planning CTs with treatment CBCTs. Results represent the percentage of fractions where sufficient cord coverage was met (at least 99% of the cord fell within the PRV).

Geometrical cord coverage was seen to be sufficient using all matching strategies, depending on the PRV margin of interest. With the exception of carina matching, sufficient cord coverage was observed for PRV margins greater or equal to 4 mm (Figure 3.10), suggesting that carina may be an inferior landmark. This is in contrast to the study by Higgins *et al.* (2009) who found spine and carina equally acceptable landmarks for CBCT image registration for advanced lung cancer patients; neither matching strategies compromised target coverage. Those results

were however challenged by Lavoie *et al.* (Lavoie *et al.*, 2012) who determined that carina matching was superior to spine matching with regards to lung tumour and nodal coverage. The work of this thesis showed that automatic carina matching was superior to all other matching strategies except for soft-tissue with respect to frequency of successful ITV coverage (Figure 3.9), but again resulted in compromised cord coverage for cord PRV margins less than 5 mm. Table 3.3 shows the combination of PTV margins and matching strategies that achieved sufficient ITV coverage in at least 90% of the fractions, while Table 3.4 shows the combination of cord PRV margins and matching strategies that achieved sufficient cord coverage in at least 90% of the fractions.

Table 3.3. Possible combinations of matching strategies and PTV margins that achieved sufficient ITV coverage in at least 90% of the fractions.

| PTV Margin (LR, AP, SI mm) | Matching Strategy | | | | |
|---|---|---|---|---|---|
| | Clinical | Cord | Carina | Cord +carina | ITV |
| 5,5,5 | | | | | |
| 5,5,8 | | | | | ✓ |
| 6,6,6, | | | ✓ | | ✓ |
| 6,6,10 | ✓ | ✓ | ✓ | ✓ | ✓ |
| 7,7,7 | | ✓ | ✓ | ✓ | ✓ |
| 8,8,8 | ✓ | ✓ | ✓ | ✓ | ✓ |
| 10,10,10 | ✓ | ✓ | ✓ | ✓ | ✓ |

Table 3.4. Possible combinations of matching strategies and isotropic cord PRV margins that achieved sufficient cord coverage in at least 90% of the fractions.

| PRV Margin (mm) | Matching Strategy | | | | |
|---|---|---|---|---|---|
| | Clinical | Cord | Carina | Cord +carina | ITV |
| ≤ 3 | | | | | |
| 4 | ✓ | ✓ | | ✓ | ✓ |
| 5 | ✓ | ✓ | ✓ | ✓ | ✓ |
| 6 | ✓ | ✓ | ✓ | ✓ | ✓ |

The clipbox defined for each automatic matching strategy included an additional 2 cm margin around the landmark. Grams and Brown *et al.* (2014) evaluated automatic matching using three clipbox expansions (1-2 cm, 5-6 cm, entire CBCT image) of the ITV and PTV for conventionally fractionated lung tumours. They found that automatic matching using the PTV with a small expansion (1-2 cm) was the most consistent with a physician's manual match, while inconsistencies were seen with the use of large clipboxes. The inconsistencies between manual and automatic matching arose due to decreased tumour size during treatment. In this thesis, soft-tissue matching of the ITV with a 2 cm margin provided the highest frequency of sufficient target coverage for all investigated PTV margins (Figure 3.9) while accounting for varying target size seen in Figure 3.7. This is in line with the work of Rahman (2014) which deemed soft-tissue matching using ITV plus a 1 or 2 cm expansion superior compared to bone matching. While a minimal 2 mm translation was required to employ the simulated couch correction, there was no upper limit imposed in this analysis unlike the clinical protocol which had an upper translational limit of 15 mm. This was to observe any potential flaws using a purely automatic protocol. By allowing any translational magnitude (e.g., 20 mm), the limitation of automatic matching could be quantified by the resulting geometrical miss of either the ITV or cord. However, in practice, large translations would serve as an indication of severe misalignment. Even if the large translation is required for geometrical alignment, there are additional concerns with the position of surrounding anatomy relative to the treatment beams. Automatic matching yielded extremely poor geometrical

coverage for some fractions. For example, in Patient 08, automatic bone matching during fractions 4 and 13 resulted in ITV coverages of 93% and 67% using a 10 mm PTV margin respectively, while 100% coverage was achieved in both cases when automatic ITV matching was employed. This example demonstrated that for those particular fractions, bone was an inferior landmark for target matching in lung IGRT and thus manual assessments are needed to identify large geometrical misses. Multiple studies have shown the potential flaws of using bony anatomy as a surrogate of the target (Grills *et al.*, 2008; Purdie *et al.*, 2007; Suzuki *et al.*, 2012; Yeung *et al.*, 2009). However, visual assessments following any automatic matching should still be employed with intervention restricted to cases where comprised coverage is obvious. It is unlikely that minor modifications of the automatic matching corrections would improve patient alignment since clinical matching resulted in the lowest amount of coverage success for all evaluated margins (Figure 3.9). However, this investigation alone does not give a conclusive statement with regards to the most appropriate landmark for registration. Understanding the effects of matching strategy on ITV and OAR (cord) coverage along with rotational tolerance would give clinics a better understanding of the effectiveness on their IGRT protocol.

### 3.2.2 Influence of Rotational Tolerance

The clinical rotations for each patient shown in Figure 3.11 were obtained by rigid registration of corresponding planning CT and CBCT images. The mean (± standard deviation) rotational deviations for pitch, yaw, and roll were 0.06° ± 1.68°, 0.03° ± 1.44°, and -0.27° ± 1.33° with absolute maxima of 6.25°, 4.06°, and

5.93° respectively. The mean of the absolute maximum rotation independent of axis was 1.94° ± 1.12°. Simulated rotations were drawn based on random sampling of these clinical rotations with a normal distribution. Figure 3.12 shows the simulated rotations for each patient. Patient-specific ITVs underwent simulations that describe the average patient. Simulations also served to improve statistical power. Note, the rotational tolerance imposed on an IGRT protocol is independent of rotation axis; the rotational assessment made during the first registration process only depends on the maximum rotation. Table 3.5 shows the percentage of fractions that were within various rotational tolerances. The clinical rotations showed that only 41 of the 251 clinical fractions (16.7%) were less than 1°. Couch shifts were simulated using the various matching strategies to correct for the simulated rotational errors. Figure 3.13 shows the frequency of simulated fractions that required a simulated couch shift greater than the imposed 2 mm translation tolerance. For all rotational tolerances, at least 80% of the simulated fractions did not require an additional couch shift following perfect set-up between planning and the simulated fraction. Translations were expected to be relatively low due to the nature of these simulations, which have essentially isolated rotational errors; however, three DOF registration using all matching strategies still revealed opportunities for correction.

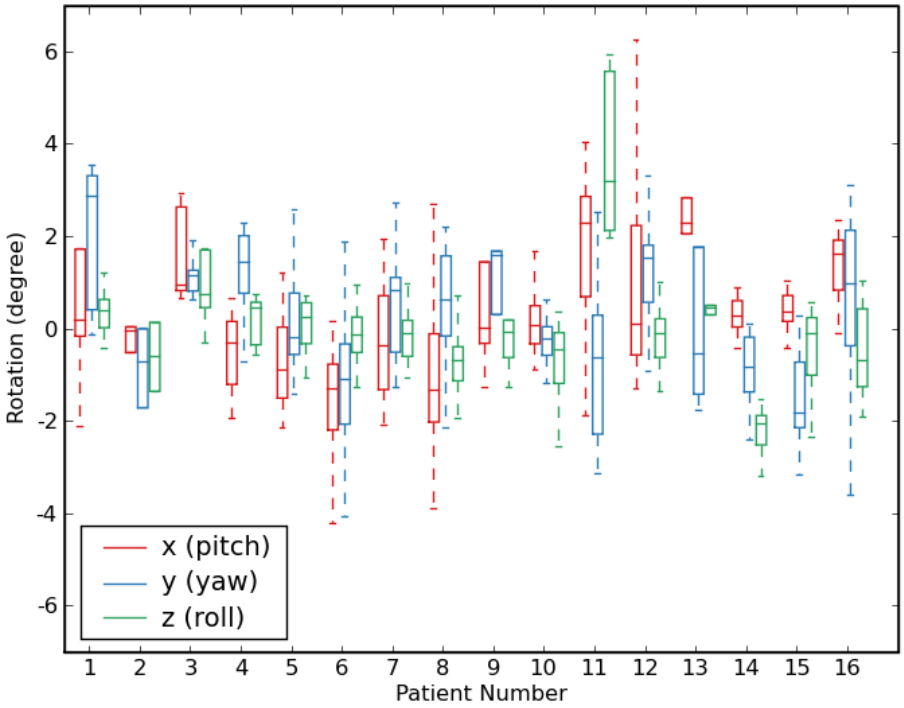


Figure 3.11. Box-and-whisker plot showing the clinical pitch, yaw, and roll rotations for each patient. Rotations were obtained by rigid registration between planning CT and treatment CBCT images. The bottom and top of the box respectively represent the first and third quartiles (interquartile range), and the band inside the box represents the second quartile (median). The whiskers represent an observed rotation that was within 1.5 times the interquartile range.

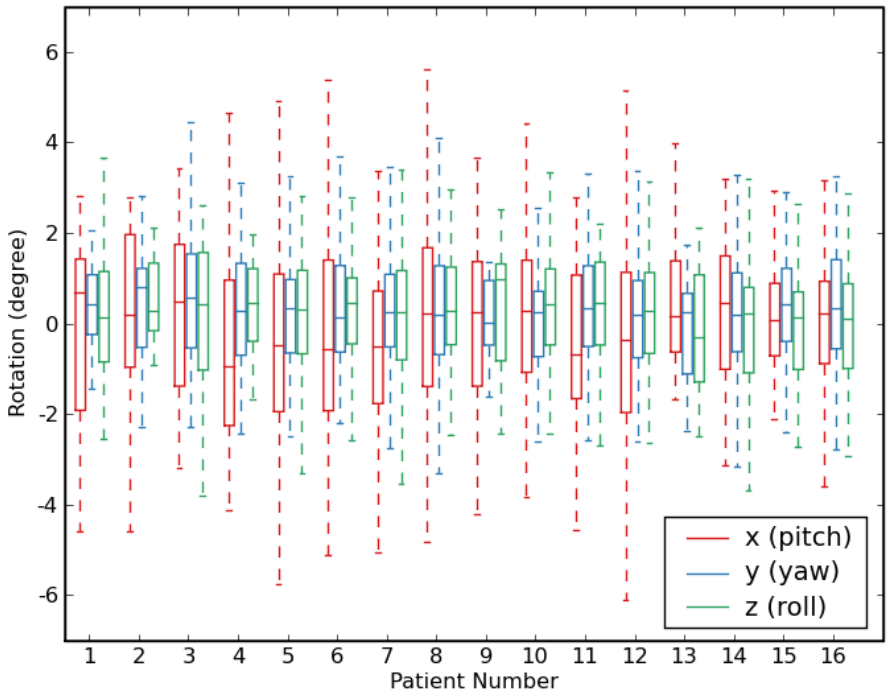


Figure 3.12. Box-and-whisker plot showing the simulated pitch, yaw, and roll rotations applied to each patient. Rotations were obtained from a normal distribution of the clinical rotations seen in Figure 3.11. The bottom and top of the box respectively represent the first and third quartiles (interquartile range), and the band inside the box represents the second quartile (median). The whiskers represent a simulated rotation that was within 1.5 times the interquartile range.

Table 3.5. Comparison of rotational errors between clinical (251 fractions) and simulation (1004 fractions) data.

| Rotational Tolerance (°) | % of Fractions < Tolerance | |
|---|---|---|
| | Clinical | Simulation |
| 1 | 16.7 | 11.7 |
| 2 | 59 | 49.3 |
| 3 | 86.9 | 82.1 |
| 4 | 94.4 | 93.7 |
| 5 | 96.8 | 98.6 |

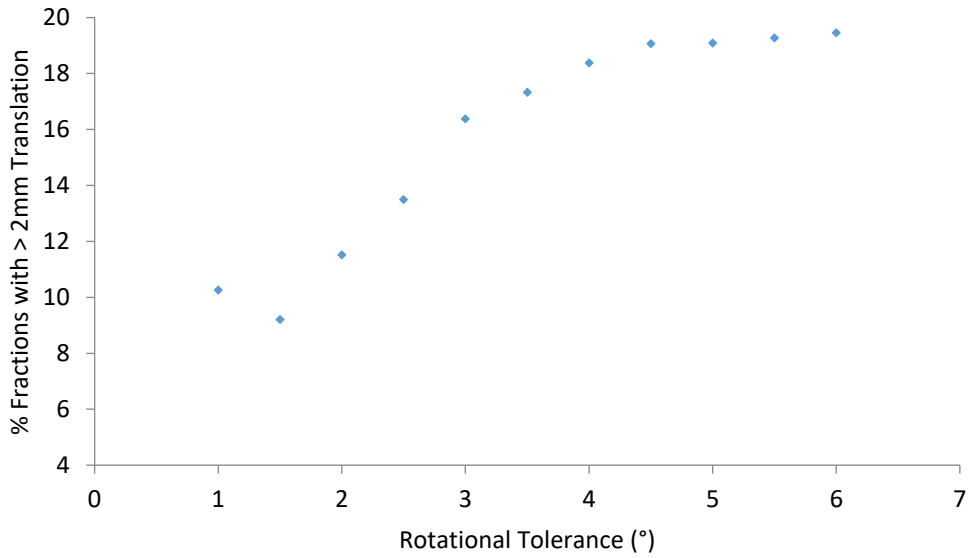


Figure 3.13. Percentage of simulated fractions that required a translational correction greater than 2 mm in any direction to account for simulated rotational error following perfect set-up.

Figures 3.14 to 3.18 document the patient-specific mean ITV and cord coverage achieved for each rotational tolerance using the simulations from the 4 automatic matching strategies. Figures 3.19 and 3.20 show the histograms of successful ITV and cord coverage respectively using all matching strategies, including the clinical strategy, which did not undergo additional simulations.

(a)

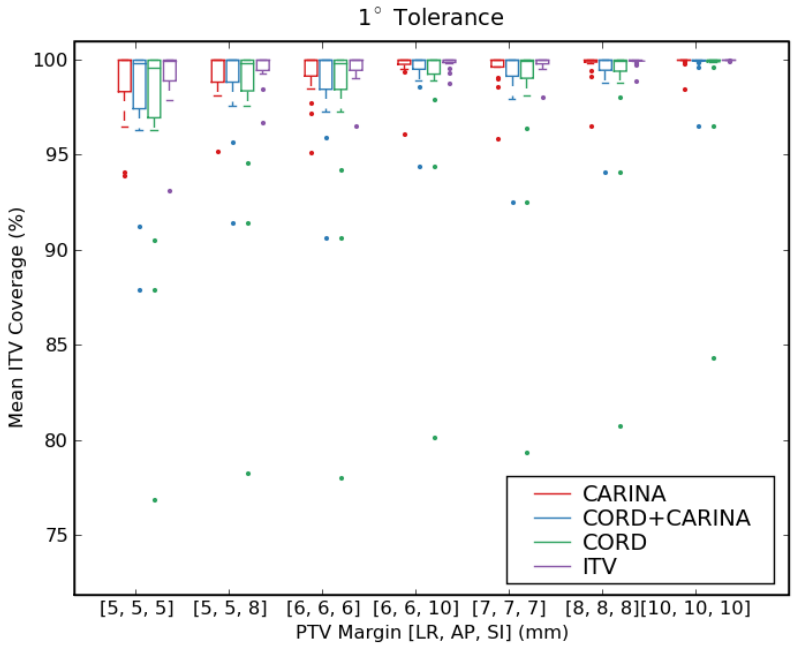


(b)

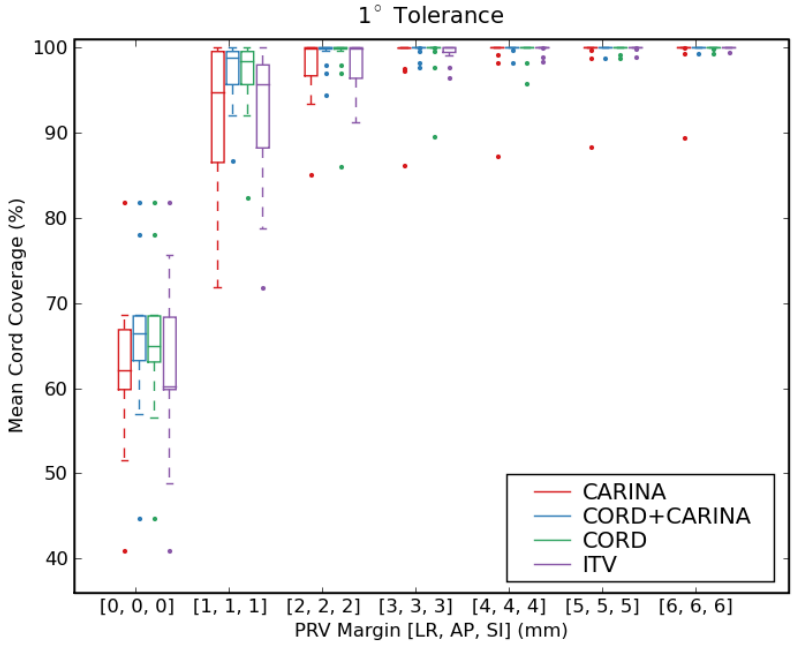


Figure 3.14. Box-and-whisker plots of the patient-specific means of (a) ITV and (b) cord coverage for simulated rotations with an imposed 1° rotational tolerance. Coverage was evaluated following four different matching strategies. The bottom and top of the box respectively represent the first and third quartiles (interquartile range), and the band inside the box represents the second quartile (median). The whiskers represent an observed coverage that was within 1.5 times the interquartile range.

(a)

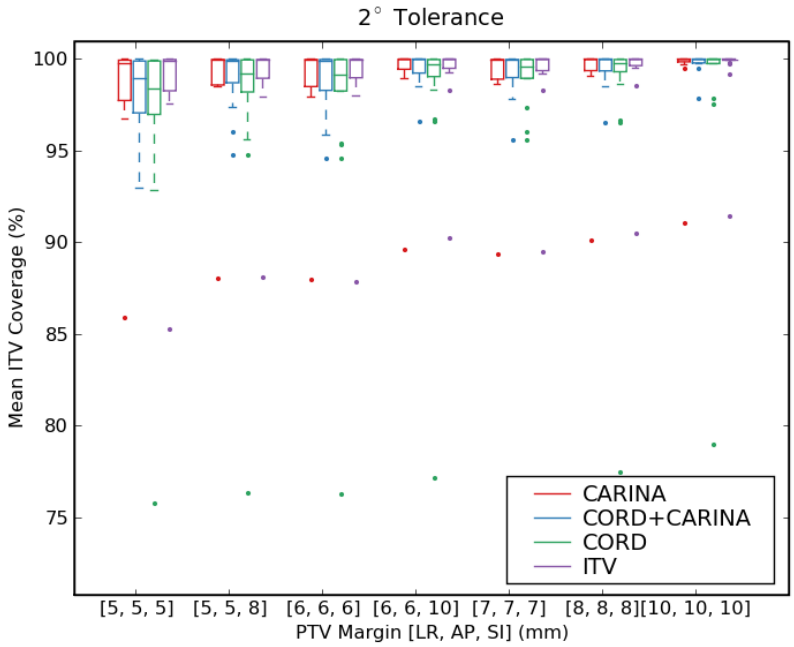


(b)

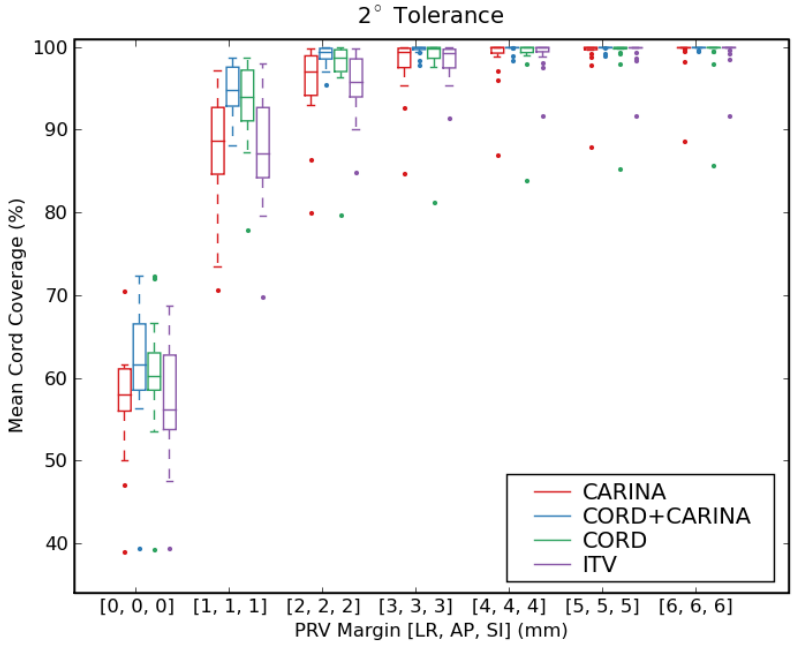


Figure 3.15. Box-and-whisker plots of the patient-specific means of (a) ITV and (b) cord coverage for simulated rotations with an imposed 2° rotational tolerance. Coverage was evaluated following four different matching strategies. The bottom and top of the box respectively represent the first and third quartiles (interquartile range), and the band inside the box represents the second quartile (median). The whiskers represent an observed coverage that was within 1.5 times the interquartile range.

(a)

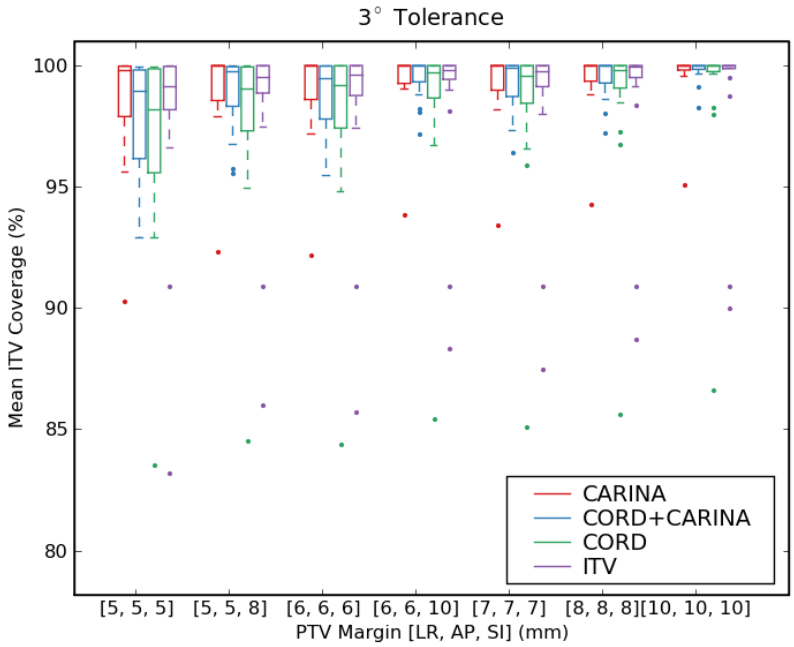


(b)

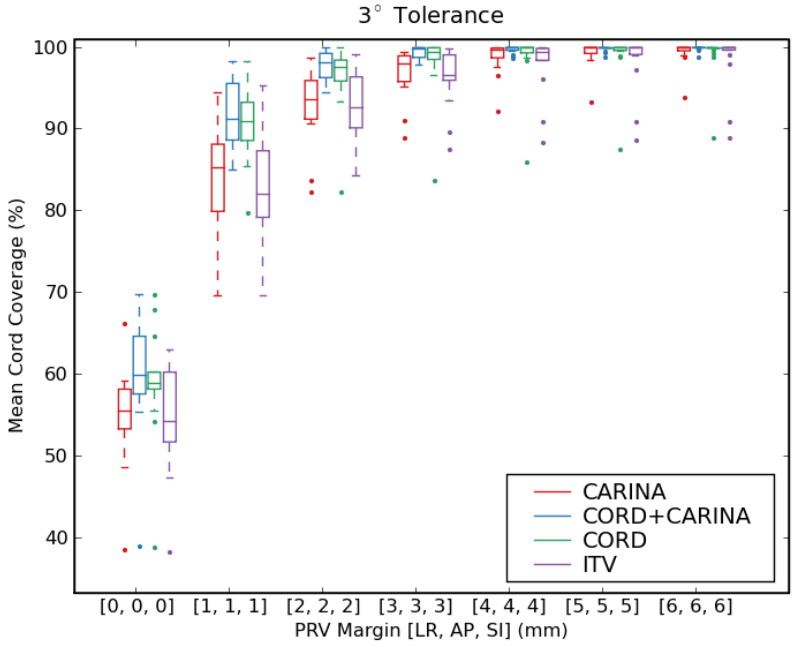


Figure 3.16. Box-and-whisker plots of the patient-specific means of (a) ITV and (b) cord coverage for simulated rotations with an imposed 3° rotational tolerance. Coverage was evaluated following four different matching strategies. The bottom and top of the box respectively represent the first and third quartiles (interquartile range), and the band inside the box represents the second quartile (median). The whiskers represent an observed coverage that was within 1.5 times the interquartile range.

(a)

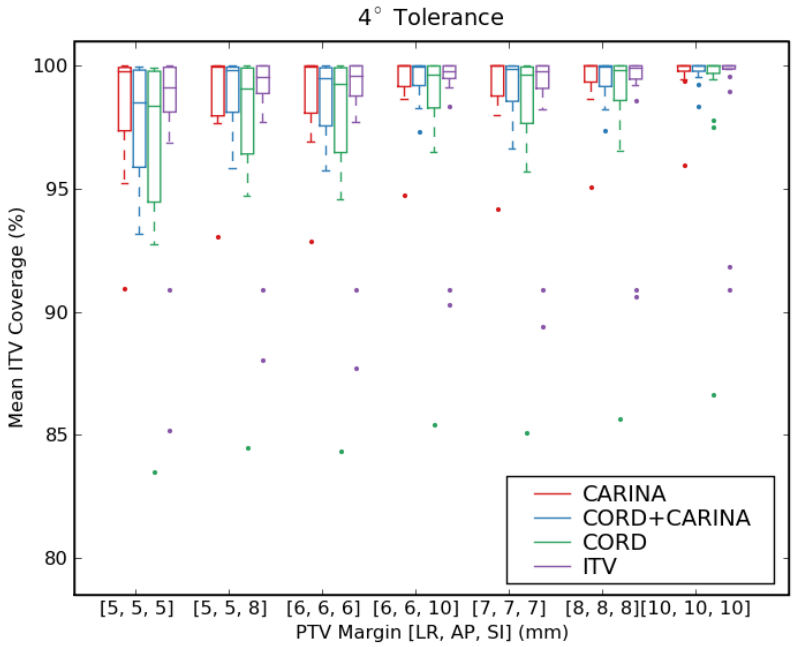


(b)

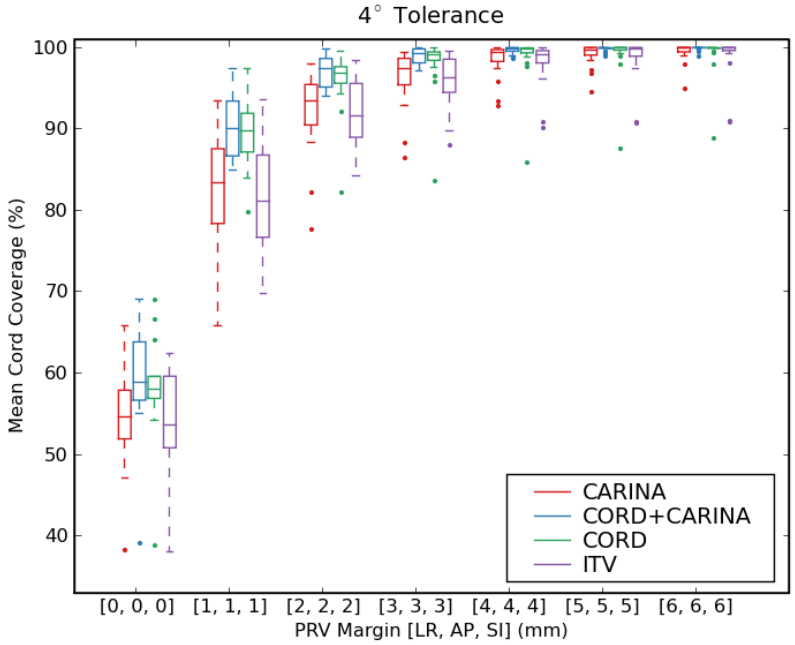


Figure 3.17. Box-and-whisker plots of the patient-specific means of (a) ITV and (b) cord coverage for simulated rotations with an imposed 4° rotational tolerance. Coverage was evaluated following four different matching strategies. The bottom and top of the box respectively represent the first and third quartiles (interquartile range), and the band inside the box represents the second quartile (median). The whiskers represent an observed coverage that was within 1.5 times the interquartile range.

(a)

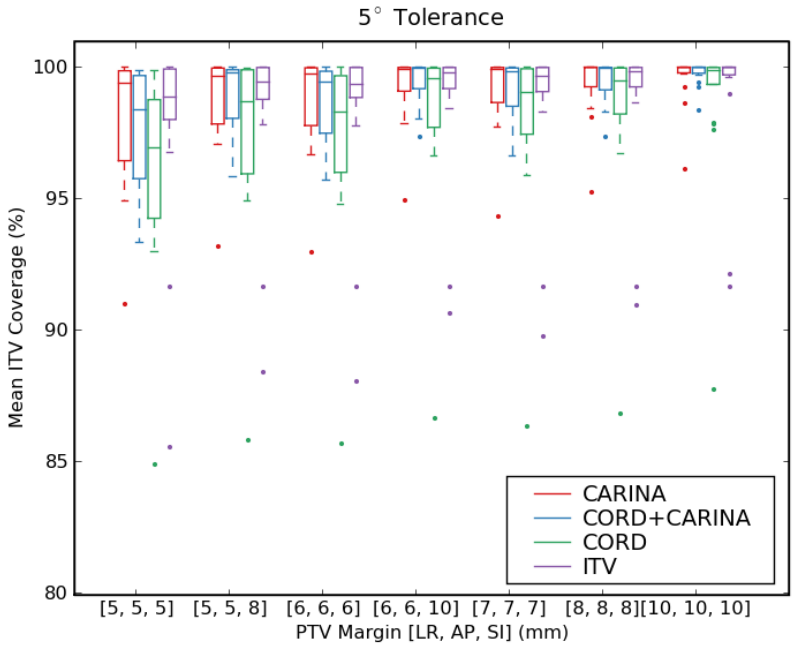


(b)

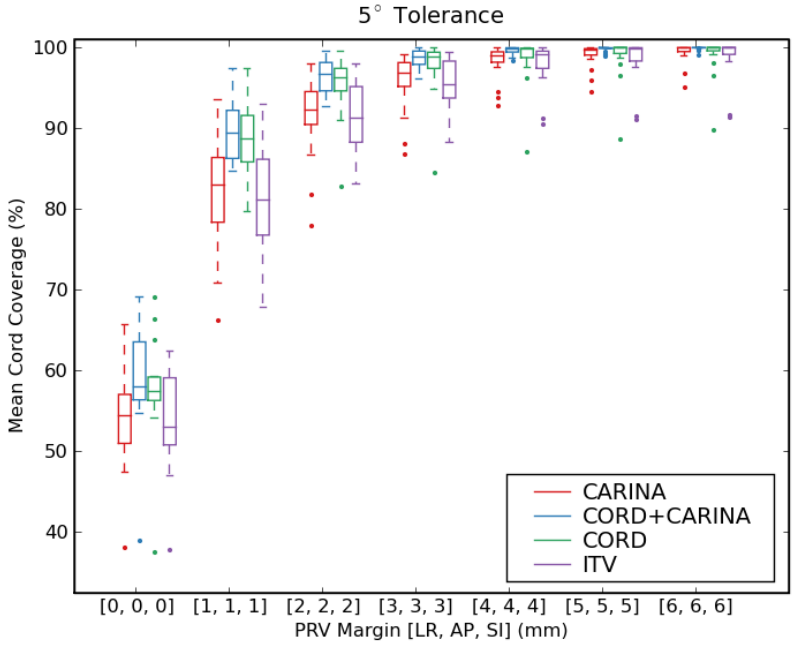


Figure 3.18. Box-and-whisker plots of the patient-specific means of (a) ITV and (b) cord coverage for simulated rotations with an imposed 5° rotational tolerance. Coverage was evaluated following four different matching strategies. The bottom and top of the box respectively represent the first and third quartiles (interquartile range), and the band inside the box represents the second quartile (median). The whiskers represent an observed coverage that was within 1.5 times the interquartile range.

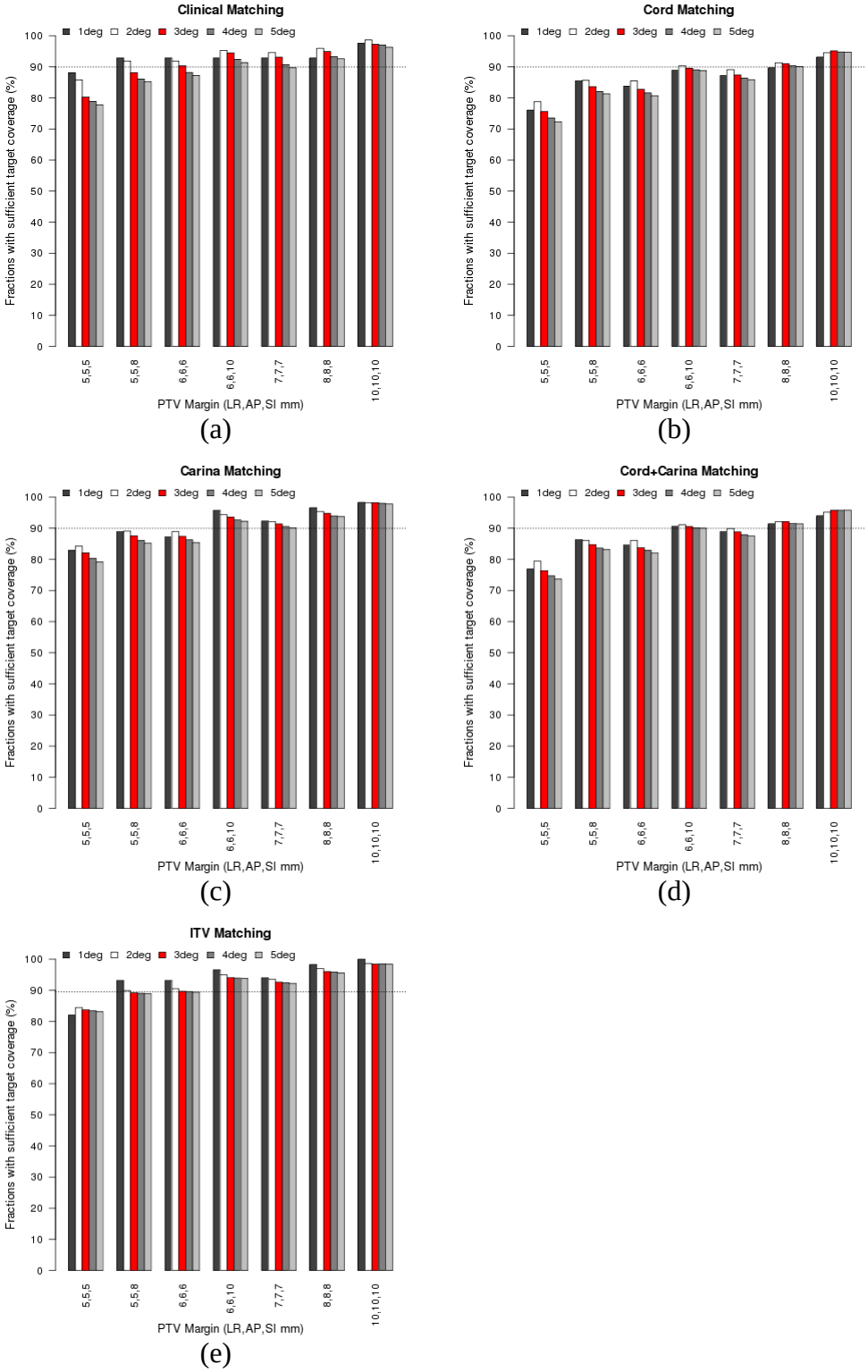


Figure 3.19. Percentage of fractions where sufficient ITV coverage was met within various PTV margins and rotational tolerances using the (a) clinical match and automatic matches of (b) cord, (c) carina, (d) combination of cord and carina, and (e) ITV. Only automatic matching results were based on simulation data.

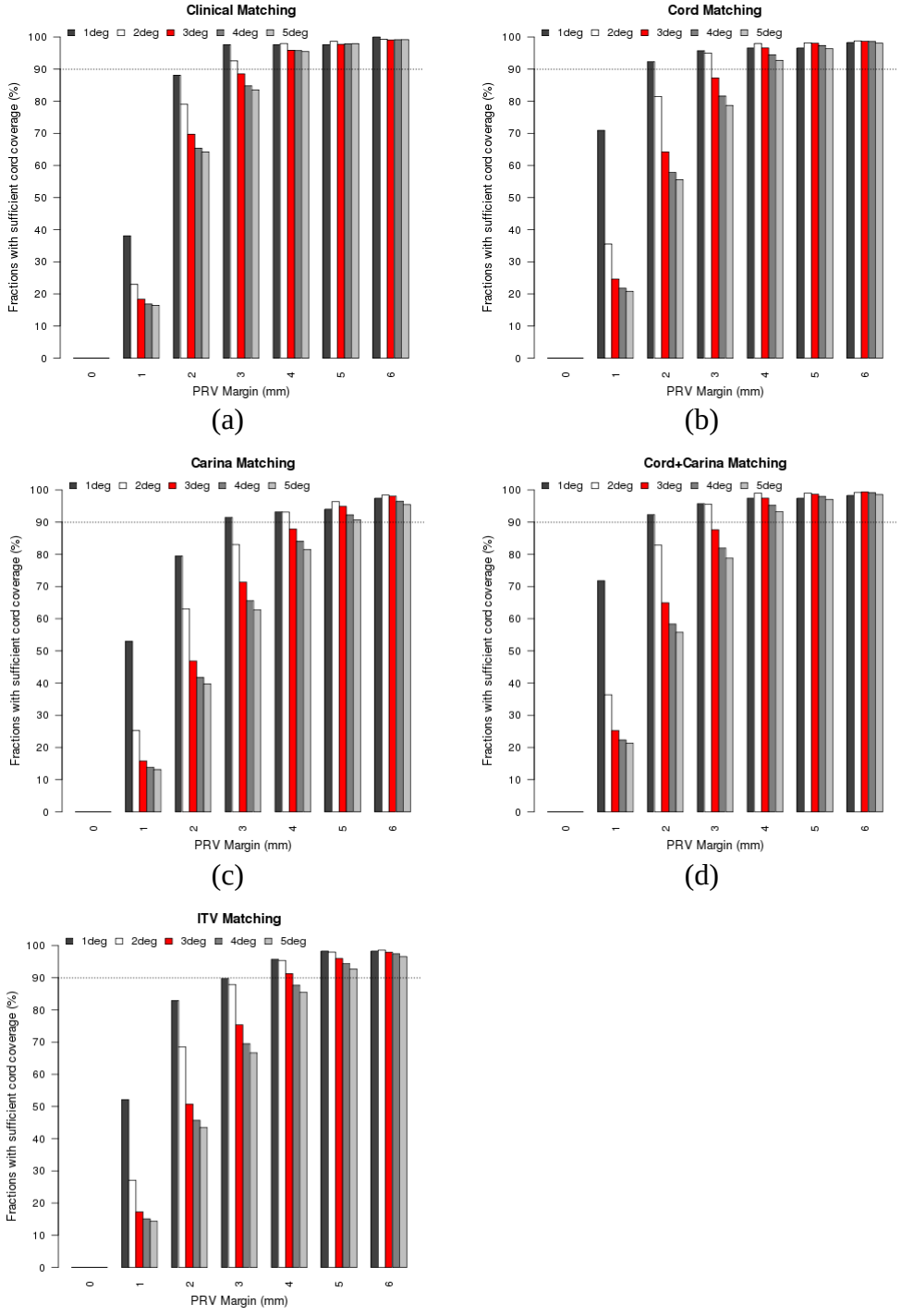


Figure 3.20. Percentage of fractions where sufficient cord coverage was met within various PRV margins and rotational tolerances using the (a) clinical match and automatic matches of (b) cord, (c) carina, (d) combination of cord and carina, and (e) ITV. Only automatic matching results were based on simulation data.

### 3.2.3 Interplay of IGRT Parameters

Selecting an appropriate combination of PTV margin, PRV margin, matching strategy, and rotational tolerance entailed the following analyses. First, a pool of acceptable PTV margins was formed from those covering at least 99% of the ITV in 90% of the fractions (Table 3.3). Second, a pool of PRV margins achieving least 99% cord coverage in 90% of the fractions was identified (Table 3.4). Next, a Friedman test (F) was used to test for significant differences between matching strategies within a specific margin. Input data consisted of the mean ITV coverage per patient. Friedman tests were conducted under the case of large samples. Since there were more than 13 patients, the critical value of F was determined by the critical value for the $\chi^2$ test with a tolerance of 0.05 for degrees of freedom equal to (matching strategies – 1). If there was no significance (i.e., F value less than or equal to the critical value of $\chi^2$), then any matching strategy would be acceptable. If there was significance, a Nemenyi test was conducted to see possible differences between pairs. Scaled ITV coverage data were used to further reduce the possible matching strategies. More appropriate matching strategies would demonstrate a lack of significance between non-scaled and scaled ITV coverage data using a Wilcoxon signed rank test (tolerance value of 0.05). However, combinations of matching strategies and PTV margins based on scaled ITVs that still achieved sufficient coverage in at least 90% of the fractions were also acceptable. Once an interesting set of PTVs and PRVs was established and the optimal matching method identified, the acceptable rotational tolerance was determined by ensuring the ITV and cord are covered 90% of the time. The most

optimal solution to the lung IGRT protocol consisted of a matching strategy that minimized PTV margin, cord PRV margin, and rotational tolerance, while maximizing the frequency of successful target coverage. It should be noted that PTV margin selection did not account for intrafractional motion as conducted in Project 1 since post-treatment images were not analyzed using the automatic matching strategies.

Following this process, Table 3.3 shows that the smallest margins that achieved sufficient ITV coverage in at least 90% of the fractions were the 6,6,10 mm and 6,6,6 mm margins, where the latter was previously shown to be affected by intrafractional motion when the clinical matching strategy was employed (Project 1; Table 3.1). For this reason, the results again lean towards the 6,6,10 mm PTV margin as optimal in terms of ITV coverage, while the isotropic 6 mm PTV margin may be used as an alternative option if intrafractional motion is ignored. Successful coverage using the 6,6,10 mm margin was achieved using all matching strategies although the Friedman test revealed a significant difference (F-value=17.3854, $\chi^2_{0.05}(df = 4)$=9.488, $p < 0.01$). A Nemenyi post-hoc test was conducted on the matching strategies for this margin with the results shown in Table 3.6.

Table 3.6. *P*-values for pairwise comparisons of matching strategies using the Nemenyi multiple comparison test for the 6,6,10 mm PTV margin. Significance between pairs is seen for p-values less than 0.05.

| | Carina | Clinical | Cord | Cord+carina |
|---|---|---|---|---|
| Clinical | 0.187 | - | - | - |
| Cord | 0.700 | 0.899 | - | - |
| Cord+carina | 0.987 | 0.448 | 0.936 | - |
| ITV | 0.899 | 0.018 | 0.187 | 0.629 |

According to the Nemenyi post-hoc test for multiple joint samples shown in Table 3.6, the clinical matching strategy based on the mean ITV coverage per patient differed significantly ($p < 0.05$) to the soft-tissue (ITV) matching strategy. All other comparisons did not reveal significant differences ($p > 0.05$). From Figure 3.9, the frequencies of sufficient ITV coverage using the 6,6,10 mm PTV margin were 90.8, 93.2, 95.6, 94.0, and 97.6 % for the clinical, cord, carina, cord+carina, and soft-tissue matching strategies respectively. Indeed, significance between clinical and soft-tissue matching strategies makes sense as these two strategies represented the minimum and maximum frequencies (91 % vs. 98%).

Successful coverage using the 6 mm isotropic margin was achieved using the carina and soft-tissue matching strategies and a Friedman test revealed a significant difference between the five types of matching strategies (F-value=25.249, $\chi^2_{0.05}(df = 4)$=9.488, $p < 0.01$). A Nemenyi post-hoc test conducted on the matching strategies for this 6 mm margin did not reveal significant differences between carina and soft-tissue matching, which both achieved successful coverage in 92% of the fractions. The significant pairs included carina and clinical ($p = 0.03$), clinical and soft-tissue ($p < 0.01$), and cord and soft-tissue ($p = 0.04$).

Although the treatment plans used for this patient group did not contain and account for cord PRVs, this analysis revealed a geometrical inaccuracy of at least 3 mm between planning and treatment cord positions, even after couch corrections. This can be seen in Figure 3.10 which showed that for all matching strategies, cord coverage was not sufficient in a least 15% of the fractions for PRV margins of 3

mm or less. Therefore, a minimum cord PRV margin of at least 4 mm appears to be appropriate. This is in line with the literature that addressed margins for geometric uncertainty around organs at risk in radiotherapy. McKenzie, van Herk, and Minjnheer (2002) utilized a formula for serial organs that suggested a uniform margin of 4.6 mm around the cord to account for both systematic and random uncertainties. Unlike the PTV margin recipe, the margin recipe for cord PRVs was not challenged in this thesis since there is less motion and deformation involved. Figure 3.10 and Table 3.4 show that all matching strategies achieve sufficient cord coverage in at least 90% of the fractions for the 5 and 6 mm PRV margins. With the exception of carina matching, all matching yielded sufficient coverage for the 4 mm cord PRV margin. Further statistical analysis using the Friedman test indeed revealed significant differences between the matching strategies for the 4 mm PRV margin (F-value=12.3359, $\chi^2_{0.05}(df = 4)$=9.488, $p < 0.05$). A Nemenyi post-hoc test was conducted on the matching strategies for this 4 mm PRV margin with results shown in Table 3.7.

Table 3.7. *P*-values for pairwise comparisons of matching strategies using a Nemenyi multiple comparison test for the 4 mm PRV margin.

| | Carina | Clinical | Cord | Cord+carina |
|---|---|---|---|---|
| Clinical | 0.260 | - | - | - |
| Cord | 0.041 | 0.936 | - | - |
| Cord+carina | 0.056 | 0.963 | 1.000 | - |
| ITV | 0.260 | 1.000 | 0.936 | 0.936 |

According to the Nemenyi post-hoc test for multiple joint samples, the carina matching strategy based on the mean cord coverage per patient differed significantly ($p < 0.05$) to the cord matching strategy when a 4 mm PRV margin

was evaluated. All other comparisons did not reveal significant differences ($p > 0.05$). Friedman tests for matching strategy differences under the 5 mm and 6 mm PRV margins revealed a lack of significance with respect to the mean cord coverage. Thus, any matching strategy can be used with the more typical 5 mm cord PRV employed in lung IGRT at the JCC.

The results thus far showed that the combination of a 6,6,10 mm PTV margin with a 5 mm cord PRV using any matching strategy is acceptable, with soft-tissue matching providing the highest frequency of ITV coverage. A 4 mm PRV margin could be employed with the exception of carina matching. Alternatively, the combination of an isotropic 6 mm PTV margin with a 5 mm cord PRV using either carina or soft-tissue matching is acceptable. The next analysis to reduce possible matching strategies was to determine if scaling the ITVs resulted in significant coverage loss. Wilcoxon Signed Rank Tests were used to test differences in coverage between unscaled and scaled ITVs. These results are shown in Table 3.8. The clinical matching strategy was eliminated for the 6,6,10 mm PTV margin as there were significant differences detected between the unscaled and scaled ITV coverage results. In the alterative 6 mm PTV margin, significant differences were detected between the unscaled and scaled ITV coverage using carina matching, thus eliminating this option.

Table 3.8. Possible combinations of matching strategies and PTV margins that did not show significance between unscaled and scaled ITV coverage using Wilcoxon signed rank test ($p > 0.05$) or achieved sufficient scaled ITV coverage in at least 90% of the fractions.

| PTV Margin (LR, AP, SI mm) | Matching Strategy | | | | |
|---|---|---|---|---|---|
| | Clinical | Cord | Carina | Cord +carina | ITV |
| 5,5,5 | | | | | |
| 5,5,8 | | | | | ✓ |
| 6,6,6, | | | | | ✓ |
| 6,6,10 | | ✓* | ✓* | ✓* | ✓ |
| 7,7,7 | | ✓ | ✓ | ✓ | ✓ |
| 8,8,8 | ✓* | ✓ | ✓ | ✓ | ✓ |
| 10,10,10 | ✓ | ✓ | ✓ | ✓ | ✓ |

*Wilcoxon signed rank test revealed significance but scaled ITV still achieved sufficient coverage in 90% of the fractions

The last step of determining the optimal approach for a lung IGRT protocol involved incorporating the effect of rotations. The goal was to find a rotational tolerance, PTV and PRV margins, and matching strategy that resulted in sufficient target and cord coverage in at least 90% of the fractions. An important factor to consider when choosing a rotational tolerance is the frequency of occurrence since exceeding the tolerance leads to patient repositioning and additional imaging. If the tolerance is too low, excessive time and effort is needed to execute the workflow. According to Table 3.5, a 2° tolerance was exceeded in 40% and 50% of the clinical and simulated cases respectively. Having to reposition and perform the image registration process in roughly half of the cases would not be clinically feasible. Thus, the combination of any matching strategy and PTV margin using a 2° tolerance would be removed as an option. This is in contrast to the CBCT study by Guckenberger *et al.* (2007) which recorded 26.4% cases greater than 2°; however, this was limited to 48 CBCTs across 6 patients. Table 3.9 shows the largest acceptable rotational tolerance for the possible combinations of matching

strategies and PTV margins from Table 3.8. For the 6,6,10 mm margin, with the exception cord matching, all other matching strategies could be tolerated with a 5° rotation (Figure 3.19). Cord matching was limited to a 2° tolerance and therefore eliminated as an option. Figure 3.19(e) shows that the use of soft-tissue matching with the isotropic 6 mm PTV margin would require a rotational tolerance of 4°, which barely met the cut off criterion, while the 5° tolerance fell short of the 90% mark by less than 1 percent.

The consideration of PRV margin and cord coverage based on the rotational simulations affected the rotational tolerance. Table 3.10 shows the largest acceptable rotational tolerance for the possible combinations of matching strategies and cord PRV margins seen in Table 3.4. The soft-tissue matching strategy was previously shown to be acceptable with a 4 mm PRV margin based on clinical cord coverage (Table 3.4) and a 5° rotational tolerance based on ITV coverage (Table 3.9). However, Figure 3.20(e) shows that using this matching strategy along with a 4 mm PRV margin would require a rotational tolerance of 3°. All other PRV and matching strategy options could be employed with a 5° tolerance.

Table 3.9. Largest acceptable rotational tolerance for the possible combinations of matching strategies and PTV margins.

| PTV Margin (LR, AP, SI mm) | Matching Strategy | | | | |
|---|---|---|---|---|---|
| | Clinical | Cord | Carina | Cord +carina | ITV |
| 5,5,5 | | | | | |
| 5,5,8 | | | | | 3° |
| 6,6,6, | | | | | 4° |
| 6,6,10 | | 2° | 5° | 5° | 5° |
| 7,7,7 | | 0° | 5° | 2° | 5° |
| 8,8,8 | 5° | 5° | 5° | 5° | 5° |
| 10,10,10 | 5° | 5° | 5° | 5° | 5° |

Table 3.10. Largest acceptable rotational tolerance for the possible combinations of matching strategies and PRV margins.

| PRV Margin (mm) | Matching Strategy | | | | |
|---|---|---|---|---|---|
| | Clinical | Cord | Carina | Cord +carina | ITV |
| 4 | 5° | 5° | | 5° | 3° |
| 5 | 5° | 5° | 5° | 5° | 5° |
| 6 | 5° | 5° | 5° | 5° | 5° |

This work explored the interplay of various parameters in a lung IGRT protocol including PTV margin, PRV margin, matching strategies, and rotational tolerance. The combination of these parameters impact the overall structure of an IGRT protocol, specifically work flow timing and geometrical accuracy. The work of Li, Jaffray, Wilson, and Moseley (2016) found that there was a correlation between image assessment decision timing and setup displacement magnitude. For lung IGRT, the decision timing was relatively quick (less than 75s on average) compared to genito-urinary or gynecological disease sites. Nevertheless, justified corrective action levels serve as a measure of clinical integrity for meeting sufficient patient care. A tighter rotational tolerance of 3° would be more susceptible to repositioning, while larger tolerances (4° or 5°) result in lower (although minor) geometrical coverage of ITV and cord. Inappropriate combinations of matching strategies and PTV margins (e.g., automatic cord matching with a 5 mm PTV margin) would result in increased treatment setup difficulties and sub-optimal geometrical coverage. There is no single solution as gains in one area have to be balanced against losses in another. Table 3.11 presents combinations of parameters comprising some potential IGRT protocols. The majority of the enable a 5° tolerance along with a 5 mm PRV margin. IGRT

Protocol Options 1 and 2 allow any matching strategy using the isotropic 8 or 10 mm PTV margins, a 5 mm cord PRV margin, and 5° rotational tolerance. IGRT Protocol Options 3 and 4 both involve using an isotropic 7 mm PTV margin with either carina or soft-tissue matching along a 5 mm cord PRV margin and 5° rotational tolerance. Options 5, 6, and 7 utilize the 6, 6, 10 mm PTV margin with carina, cord+carina, or soft-tissue matching which can all be used with a 5° tolerance and 5 mm PRV margin. However, the cord+carina matching strategy allows for a reduced PRV margin of 4 mm. The last two options (8 and 9) are more aggressive and are limited to soft-tissue matching using an isotropic 6 mm or 5,5,8 mm PTV margin, where tighter rotational tolerances of 4° and 3° were required, respectively. Although a Wilcoxon signed-rank test did reveal significant differences between the 6 mm isotropic and 6,6,10 mm anisotropic PTV margins using soft-tissue matching ($p < 0.05$), both margins resulted in 15 out of 16 patients with mean ITV coverage of at least 99%, where Patient 01 was the only patient compromised; based on 7 fractions, mean ITV coverage were 95.8% and 98.9%, respectively. In the options that did not involve the clinical matching strategy, intrafractional motion was not directly tested and the PTV margins may not be potentially robust to intrafractional motion; however, it is safe to assume that intrafractional motion would be contained for the 6,6,10 mm and 8 mm margins since they were deemed acceptable in Project 1 using the now-inferior clinical matching strategy. Intrafractional variation, which includes any patient movement following initial set-up, couch correction, and beam delivery should be minimized. With the combination of volumetric arc therapy delivery (Quan, Chang, *et al.*,

2012) and automatic matching (Grams, Brown, *et al.*, 2014; Li *et al.*, 2016), a faster overall treatment time from set-up to end of delivery is possible; thus, reducing the geometrical impact of intrafractional variation.

Table 3.11. Optimal Lung IGRT Protocol Parameters

| IGRT Protocol Option | PTV Margin (LR, AP, SI mm) | Matching Strategy | Cord PRV Margin (mm) | Rotational Tolerance (°) |
|---|---|---|---|---|
| 1 | 10,10,10 | Any* | 5** | 5 |
| 2 | 8,8,8 | Any* | 5** | 5 |
| 3 | 7,7,7 | Carina | 5 | 5 |
| 4 | 7,7,7 | Soft-tissue | 5 | 5 |
| 5 | 6,6,10 | Carina | 5 | 5 |
| 6 | 6,6,10 | Cord+carina | 4 | 5 |
| 7 | 6,6,10 | Soft-tissue | 5 | 5 |
| 8 | 6,6,6 | Soft-tissue | 5 | 4 |
| 9 | 5,5,8 | Soft-tissue | 5 | 3 |

* No significance between matching strategies
** 4mm cord PRV margin can be used for clinical, cord, or cord+carina matching strategies

### 3.2.4 Dose Reconstruction

This work quantified geometrical coverage to optimize various parameters of a lung IGRT protocol. The relationship between geometric and dosimetric coverage using a three-field radiotherapy technique for early-stage lung cancer was previously explored by van Sörnsen de Koste *et al.* (2001) who found sufficient dosimetric coverage was achieved even when geometrical coverage was less than 99%. Indeed, this work confirms that conclusion as shown by the dosimetric analysis for the select cases seen in Table 3.12. Three different cases were chosen to represent poor (< 90%), moderate (~95%), and sufficient geometrical coverage (99%). These cases were obtained from one of the fractions from Patients 08, 16, and 15 respectively. A direct comparison was made between the geometric and

dosimetric analyses for the optimal 6,6,10 mm PTV margin using automatic bone matching. Following the dose calculation on the deformed geometry, the 95% isoline was converted into a surface mesh. This isoline represented the high dose region during treatment following an automatic correction using bone matching. Akin to the geometric analysis, the dosimetric analysis then involved quantifying the percentage of the original planning ITV surface points within the deformed 95% isoline. For all three cases, the dosimetric analysis resulted in greater ITV coverage compared to the geometric result. This indicates all analyses in this thesis were seen as a worst case scenario. Therefore, it is likely that the computed PTV margins may be reduced further or, alternatively, that the currently suggested margins indeed achieve the goals of treatment.

Table 3.12. Comparison of ITV coverage between the purely geometric approach and dosimetric reconstruction for a single fraction following automatic cord matching. Both metrics utilized deformable image registration to localize treatment-specific ITVs. Geometric coverage was quantified as the percentage of localized ITV surface points within the PTV using a 6,6,10 mm PTV margin expansion. Dosimetric coverage was quantified as the percentage of planning ITV surface points within the 95% isoline obtained on deformed anatomy.

| Patient | ITV Coverage (%) | |
|---|---|---|
| | Geometric | Dosimetric |
| 08 | 83.0 | 91.7 |
| 16 | 94.9 | 95.1 |
| 15 | 98.8 | 99.1 |

# Chapter 4

# Conclusions and Future Work

The goal of this thesis was to develop a method to quantify the accuracy of image-guided radiation therapy (IGRT) practices, including planning target volume (PTV) design. This was carried out in two projects which aimed to show that:

1. accounting for target deformation throughout treatment can reduce the currently employed 10 mm PTV margin for lung IGRT, and
2. simultaneous optimization of various parameters of a lung IGRT protocol, including matching strategy, rotational tolerance, and PTV margin can improve treatment accuracy.

This chapter concludes the discussion of these methods and the recommendations obtained from the investigations along with future work.

## 4.1 Assessment of ITV Coverage

Project 1 utilized deformable image registration (DIR) to localize treatment-specific internal target volumes (ITV) for advanced-stage lung cancer under daily CBCT image-guidance. Geometrical accuracy of IGRT was quantified by computing the percentage of treatment ITVs within various PTV margins. Coverage was quantified for three scenarios: initial patient set-up, pre-treatment following any necessary couch corrections, and post-treatment. The analysis

confirmed that accuracy the clinically employed isotropic 10 mm PTV margin resulted in sufficient accuracy, while the 8 mm or 6,6,10 mm were the most notable. Statistically, these two margins ensured CBCT image-guidance was beneficial, intrafractional motion contained, and sufficient target coverage achieved in at least 90% of the treatment fractions. An additional advantage of the anisotropic margin is that it allows treatment of targets closer to the esophagus and spinal cord. Systematic and random error were estimated and used to calculate an anisotropic PTV margin of 3, 4, 5 in the LR, AP, and SI directions respectively using the van Herk margin recipe (2000). This calculated PTV margin is comparable to a 5 mm margin employed at other cancers when using CBCT image-guidance to align spinal cord (Bissonnette *et al.*, 2009; Higgins *et al.*, 2009); however, shown to be insufficient to satisfy the geometrical matching criteria imposed in this work.

## 4.2 Simulations to Optimize Lung IGRT Protocol Parameters

PTV margin optimization performed in Project 1 clarifies only one aspect of an IGRT protocol. To exploit the full benefits of IGRT, compressive understanding of the link between all workflow parameters is needed. Project 2 investigated the interplay between the parameters constituting a clinical lung IGRT protocol. The clinical matching strategy, which allowed for manual adjustments, along with automatic matching strategies on four regions of interest (ROI) (cord, carina, cord+carina, soft-tissue) were investigated in an advanced-stage lung cancer setting with RT delivered under daily CBCT image-guidance. Automatic matching strategies were conducted using clipboxes that included a 2 cm expansion of the ROI. Both localized ITV and cord geometrical coverage were quantified on clinical

data and simulation data that involved introducing rotational off-sets. The results showed that IGRT accuracy was compromised if inappropriate parameters are used; margins were functions of matching strategy and rotational error. Sets of optimal parameters including PTV and cord planning organ at risk (PRV) margin were proposed based on achieving sufficient ITV and cord coverage in 90% of the treatment fractions. A minimum rotational tolerance of 3° was recommended since 2° rotations would require additional repositioning ~40% of the time, which would hinder workflow efficiency. Nine IGRT protocol options were proposed. With the exception of the 5 mm PTV margin, all evaluated PTV margins were capable of being employed but restricted to certain combinations of matching strategies, cord PRV margins, and rotational tolerances. In two of the options, the PTV margins (isotropic 8 mm and 10 mm) were large enough such that any matching strategy could be employed effectively along with a 5 mm cord PRV and 5° rotational tolerance. In these two PTV margin options, the clinical, cord, and cord+carina matching strategies satisfied cord coverage with a smaller 4 mm cord PRV. However, challenges with larger PRVs are less severe compared to smaller PTVs since the cord is typically far away from the high dose regions and dose gradients can accommodate larger PRVs, unlike PTVs which must be covered by a high percentage of the prescription dose. It appeared that the clinical matching strategy was inferior to the proposed automatic matching strategies for PTV margins less than 8 mm. These automatic matching strategies were not free of large geometrical misses which prompts the IGRT protocol to still incorporate manual assessments. Perhaps additional training for therapists is required to ensure interventions do not

compromise coverage. Direct soft-tissue matching to the ITV was the most versatile strategy as it was capable of being employed with all PTV margins except for the 5 mm margin. Aggressive strategies were proposed using the smaller PTV margins of either 6 mm or 5,5,8 mm; however, these involved a trade-off with a tighter rotational tolerance of 4° and 3° respectively. Regardless of which option is chosen, IGRT needs to be implemented under a set of procedures to ensure consistency and with the results documented for future reference. Additionally, changes need to be communicated to the entire IGRT team, including physicists, dosimetrists, therapists, and oncologists.

## 4.3 Future Work

While this thesis has addressed a number of components of a lung IGRT protocol using patient-specific data to establish safe, efficient practice, a few parameters have not been analyzed. These include imaging dose - can soft-tissue matching be accurately carried out with lower CBCT dose? - and the translational action threshold. In this thesis, employment of couch corrections required exceeding a 2 mm translational action threshold. If large translational tolerances are not justified, there is potential for loss of accuracy under certain combinations of parameters. Simulations can be carried out to again quantify target and OAR coverage under various image dose and translational tolerances. However, the latter investigation is quite limited in a sense that residual patient movement during the shift is unknown (i.e., a 1 mm translational correction may actually impose an additional 2 mm translational error). The simulations in this thesis all involved quantifying geometrical accuracy based on ITV and cord expansions. Alternatively,

a matching strategy could be devised where the PRV is matched to an isodose line and ITV to the prescription isodose.

The methods of this thesis can be applied to any other disease site where accuracy of IGRT is unknown or where protocol parameters and decisions are not yet justified. Although currently limited to a retrospective analysis, validation of DIR in commercial software (García-Mollá *et al.*, 2015; Varadhan, Karangelis, Krishnan, & Hui, 2013) gives potential for efficient adaptive radiation therapy, where accurate 'deformable dose accumulation', 'automatic re-contouring' and 'tumour growth evaluation' are possible (W. Lu *et al.*, 2006; Linjing Wang, Zhang, Yuan, Zhou, & Wang, 2015). Alternatively, DIR could be used to quantify geometrical miss as seen in this thesis immediately prior to treatment. The ability to quantify miss prior to treatment can then serve as a basis for protocol decisions.

## References

Abdelnour, A. F., Nehmeh, S. A., Pan, T., Humm, J. L., Vernon, P., Schöder, H., … Erdi, Y. E. (2007). Phase and amplitude binning for 4D-CT imaging. *Physics in Medicine and Biology*, *52*(12), 3515–29. http://doi.org/10.1088/0031-9155/52/12/012

Admiraal, M. A., Schuring, D., & Hurkmans, C. W. (2008). Dose calculations accounting for breathing motion in stereotactic lung radiotherapy based on 4D-CT and the internal target volume. *Radiotherapy and Oncology*, *86*(1), 55–60. http://doi.org/10.1016/j.radonc.2007.11.022

Ahnesjö, A., & Aspradakis, M. M. (1999). Dose calculations for external photon beams in radiotherapy. *Physics in Medicine and Biology*, *44*(11), R99–R155. http://doi.org/10.1088/0031-9155/44/11/201

Balter, J. M., Ten Haken, R. K., Lawrence, T. S., Lam, K. L., & Robertson, J. M. (1996). Uncertainties in CT-based radiation therapy treatment planning associated with patient breathing. *International Journal of Radiation Oncology, Biology, Physics*, *36*(1), 167–174. http://doi.org/10.1016/S0360-3016(96)00275-1

Baskar, R., Dai, J., Wenlong, N., Yeo, R., & Yeoh, K.W. (2014). Biological response of cancer cells to radiation treatment. *Frontiers in Molecular Biosciences*, *1*, 24. http://doi.org/10.3389/fmolb.2014.00024

Bell, L. J., Cox, J., Eade, T., Rinks, M., Herschtal, A., & Kneebone, A. (2015). Determining optimal planning target volume and image guidance policy for post-prostatectomy intensity modulated radiotherapy. *Radiation Oncology*, *10*, 151. http://doi.org/10.1186/s13014-015-0467-8

Beyzadeogly, M., Ozyigit, G., & Ebruli, C. (2010). *Basic Radiation Oncology*. Springer.

Bissonnette, J.P., Purdie, T. G., Higgins, J. A., Li, W., & Bezjak, A. (2009). Cone-Beam Computed Tomographic Image Guidance for Lung Cancer Radiation Therapy. *International Journal of Radiation Oncology, Biology, Physics*, *73*(3), 927–934. http://doi.org/http://dx.doi.org/10.1016/j.ijrobp.2008.08.059

Bookstein, F. L. (1989). Principal Warps: Thin-Plate Splines and the Decomposition of Deformations. *IEEE Transactions on Pattern Analysis and Machine Itelligence*, *11*(6).

Bortfeld, T. (2006). IMRT: a review and preview. *Physics in Medicine and Biology*, *51*(13), R363–R379. http://doi.org/10.1088/0031-9155/51/13/R21

Bortfeld, T., Bürkelbach, J., Boesecke, R., Schlegel, W. (1990). Methods of image reconstruction from projections applied to conformation radiotherapy. *Physics in Medicine and Biology*, *35*(10), 1423–1434. http://doi.org/10.1088/0031-9155/35/10/007

Bortfeld, T., Jokivarsi, K., Goitein, M., Kung, J., & Jiang, S. B. (2002). Effects of intra-fraction motion on IMRT dose delivery: statistical analysis and simulation. *Physics in Medicine and Biology*, *47*(13), 2203–2220. http://doi.org/10.1088/0031-9155/47/13/302

Bosmans, G., Buijsen, J., Dekker, A., Velders, M., Boersma, L., De Ruysscher, D., … Lambin, P. (2006). An "in silico" clinical trial comparing free breathing, slow and respiration correlated computed tomography in lung cancer patients. *Radiotherapy and Oncology*, *81*(1), 73–80. http://doi.org/10.1016/j.radonc.2006.08.009

Bosmans, G., van Baardwijk, A., Dekker, A., Ollers, M., Boersma, L., Minken, A., … De Ruysscher, D. (2006). Intra-patient variability of tumor volume and tumor motion during conventionally fractionated radiotherapy for locally advanced non-small-cell lung cancer: a prospective clinical study. *International Journal of Radiation Oncology, Biology, Physics*, *66*(3), 748–753. http://doi.org/10.1016/j.ijrobp.2006.05.022

Bradley, J. D., Nofal, A. N., El Naqa, I. M., Lu, W., Liu, J., Hubenschmidt, J., … Khullar, D. (2006). Comparison of helical, maximum intensity projection (MIP), and averaged intensity (AI) 4D CT imaging for stereotactic body radiation therapy (SBRT) planning in lung cancer. *Radiotherapy and Oncology*, *81*(3), 264–268. http://doi.org/10.1016/j.radonc.2006.10.009

Bradley, J. D., Paulus, R., Komaki, R., Masters, G. A., Forster, K., Schild, S. E., … Choy, H. (2013). A randomized phase III comparison of standard-dose (60 Gy) versus high-dose (74 Gy) conformal chemoradiotherapy with or without cetuximab for stage III non-small cell lung cancer: Results on radiation dose in RTOG 0617. *ASCO Meeting Abstracts*, *31*(15_suppl), 7501.

Brahme, A. (1988). Optimal setting of multileaf collimators in stationary beam radiation therapy. *Strahlentherapie Und Onkologie*, *164*(6), 343–50.

Britton, K. R., Starkschall, G., Tucker, S. L., Pan, T., Nelson, C., Chang, J. Y., … Komaki, R. (2007). Assessment of Gross Tumor Volume Regression and Motion Changes During Radiotherapy for Non–Small-Cell Lung Cancer as Measured by Four-Dimensional Computed Tomography. *International Journal of Radiation Oncology, Biology, Physics*, *68*(4), 1036–1046. http://doi.org/10.1016/j.ijrobp.2007.01.021

Brock, K. K. (2010). Results of a Multi-Institution Deformable Registration Accuracy Study (MIDRAS). *International Journal of Radiation Oncology, Biology, Physics*, *76*(2), 583–596. http://doi.org/10.1016/j.ijrobp.2009.06.031

Brown, W. T., Wu, X., Fowler, J. F., García, S., Fayad, F., Amendola, B. E., … Schwade, J. G. (2007). Lung Metastases Treated by CyberKnife Image-Guided Robotic Stereotactic Radiosurgery at 41 Months. *Clinical Lung Cancer*, *8*(8), 488–492.

Bucci, M. K., Bevan, A., & Roach, M. (2005). Advances in Radiation Therapy: Conventional to 3D, to IMRT, to 4D, and Beyond. *CA: A Cancer Journal for Clinicians*, *55*(2), 117–134. http://doi.org/10.3322/canjclin.55.2.117

Canadian Cancer Society. (2015). Canadian Cancer Statistics Special topic : Predictions of the future burden of cancer in Canada. *Public Health Agency of Canada*, 1–151. http://doi.org/Canadian Cancer Society

Cao, M., Lasley, F. D., Das, I. J., DesRosiers, C. M., Slessinger, E. D., & Cardenes, H. R. (2012). Evaluation of Rotational Errors in Treatment Setup of Stereotactic Body Radiation Therapy of Liver Cancer. *International Journal of Radiation Oncology, Biology, Physics*, *84*(3), e435–e440. http://doi.org/10.1016/j.ijrobp.2012.05.018

Chinneck, C. D., McJury, M., & Hounsell, A. R. (2010). The potential for undertaking slow CT using a modern CT scanner. *The British Journal of Radiology*, *83*(992), 687–93. http://doi.org/10.1259/bjr/31551018

Collignon, A., Maes, F., Delaere, D., Vandermeulen, D., Suetens, P., & Marchal, G. (1995). Automated Multi-modality Image Registration Based on Information Theory. In *Information Processing in Medical Imaging* (pp. 263–274).

Dona Lemus, O. (2012). *Dose-based evaluation of a prostate bed protocol* (Master's thesis). McMaster University.

Duggan, D. M., & Coffey, C. W. (1998). Small photon field dosimetry for stereotactic radiosurgery. *Medical Dosimetry*, *23*(3), 153–159. http://doi.org/10.1016/S0958-3947(98)00013-2

Ecclestone, G., Bissonnette, J.-P., & Heath, E. (2013). Experimental validation of the van Herk margin formula for lung radiation therapy. *Medical Physics*, *40*(11), 111721. http://doi.org/10.1118/1.4824927

Ekstrand, K. E., & Barnes, W. H. (1990). Pitfalls in the use of high energy X rays to treat tumors in the lung. *International Journal of Radiation Oncology, Biology, Physics*, *18*(1), 249–252. http://doi.org/10.1016/0360-3016(90)90290-Z

Emami, B., Lyman, J., Brown, A., Cola, L., Goitein, M., Munzenrider, J. E., … Wesson, M. (1991). Tolerance of normal tissue to therapeutic irradiation. *International Journal of Radiation Oncology, Biology, Physics*, *21*(1), 109–122. http://doi.org/10.1016/0360-3016(91)90171-Y

Evans, P. M., Coolens, C., & Nioutsikou, E. (2006). Effects of averaging over motion and the resulting systematic errors in radiation therapy. *Physics in Medicine and Biology*, *51*(1), N1–N7. http://doi.org/10.1088/0031-9155/51/1/N01

Fakiris, A. J., McGarry, R. C., Yiannoutsos, C. T., Papiez, L., Williams, M., Henderson, M. A., & Timmerman, R. (2009). Stereotactic Body Radiation

Therapy for Early-Stage Non–Small-Cell Lung Carcinoma: Four-Year Results of a Prospective Phase II Study. *International Journal of Radiation Oncology, Biology, Physics*, *75*(3), 677–682. http://doi.org/10.1016/j.ijrobp.2008.11.042

Feng, M., Kong, F. M., Gross, M., Fernando, S., Hayman, J. A., & Ten Haken, R. K. (2009). Using Fluorodeoxyglucose Positron Emission Tomography to Assess Tumor Volume During Radiotherapy for Non-Small-Cell Lung Cancer and Its Potential Impact on Adaptive Dose Escalation and Normal Tissue Sparing. *International Journal of Radiation Oncology, Biology, Physics*, *73*(4), 1228–1234. http://doi.org/10.1016/j.ijrobp.2008.10.054

Ford, E. C., Mageras, G. S., Yorke, E., & Ling, C. C. (2003). Respiration-correlated spiral CT: A method of measuring respiratory-induced anatomic motion for radiation treatment planning. *Medical Physics*, *30*(1), 88. http://doi.org/10.1118/1.1531177

Fu, W., Yang, Y., Li, X., Heron, D. E., Huq, M. S., & Yue, N. J. (2006). Dosimetric effects of patient rotational setup errors on prostate IMRT treatments. *Physics in Medicine and Biology*, *51*(20), 5321–5331. http://doi.org/10.1088/0031-9155/51/20/016

Fu, W., Yang, Y., Yue, N. J., Heron, D. E., & Saiful Huq, M. (2013). Dosimetric influences of rotational setup errors on head and neck carcinoma intensity-modulated radiation therapy treatments. *Medical Dosimetry*, *38*(2), 125–132. http://doi.org/10.1016/j.meddos.2012.09.003

Gagné, I. M., & Robinson, D. M. (2004). The impact of tumor motion upon CT image integrity and target delineation. *Medical Physics*, *31*(12), 3378. http://doi.org/10.1118/1.1799291

García-Mollá, R., Marco-Blancas, N. de, Bonaque, J., Vidueira, L., López-Tarjuelo, J., & Perez-Calatayud, J. (2015). Validation of a deformable image registration produced by a commercial treatment planning system in head and neck. *Physica Medica*, *31*(3), 219–223. http://doi.org/10.1016/j.ejmp.2015.01.007

Garibaldi, C., Piperno, G., Ferrari, A., Surgo, A., Muto, M., Ronchi, S., … Orecchia, R. (2016). Translational and rotational localization errors in cone-beam CT based image-guided lung stereotactic radiotherapy. *Physica Medica*. http://doi.org/10.1016/j.ejmp.2016.05.055

Godley, A., Ahunbay, E., Peng, C., & Li, X. A. (2012). Accumulating daily-varied dose distributions of prostate radiation therapy with soft-tissue-based kV CT guidance. *Journal of Applied Clinical Medical Physics*, *13*(3), 3859. Retrieved from http://www.ncbi.nlm.nih.gov/pubmed/22584178

Graff, P., Kirby, N., Weinberg, V., Chen, J., Yom, S. S., Lambert, L., & Pouliot, J. (2013). The Residual Setup Errors of Different IGRT Alignment Procedures for Head and Neck IMRT and the Resulting Dosimetric Impact.

*International Journal of Radiation Oncology, Biology, Physics*, *86*(1), 170–176. http://doi.org/10.1016/j.ijrobp.2012.10.040

Graham, M. V, Purdy, J. A., Emami, B., Harms, W., Bosch, W., Lockett, M. A., & Perez, C. A. (1999). Clinical dose-volume histogram analysis for pneumonitis after 3D treatment for non-small cell lung cancer (NSCLC). *International Journal of Radiation Oncology, Biology, Physics*.

Grams, M. P., Brown, L. C., Brinkmann, D. H., Pafundi, D. H., Mundy, D. W., Garces, Y. I., … de los Santos, L. E. F. (2014). Analysis of automatic match results for cone-beam computed tomography localization of conventionally fractionated lung tumors. *Practical Radiation Oncology*, *4*(1), 35–42. http://doi.org/10.1016/j.prro.2013.02.008

Grams, M. P., Fong de Los Santos, L. E., Brown, L. C., Mayo, C. S., Park, S. S., Garces, Y. I., … Brinkmann, D. H. (2014). Separating the dosimetric consequences of changing tumor anatomy from positional uncertainty for conventionally fractionated lung cancer patients. *Practical Radiation Oncology*, *4*(6), 455–65. http://doi.org/10.1016/j.prro.2014.02.006

Grills, I. S., Hugo, G., Kestin, L. L., Galerani, A. P., Chao, K. K., Wloch, J., & Yan, D. (2008). Image-Guided Radiotherapy via Daily Online Cone-Beam CT Substantially Reduces Margin Requirements for Stereotactic Lung Radiotherapy. *International Journal of Radiation Oncology, Biology, Physics*, *70*(4), 1045–1056. http://doi.org/10.1016/j.ijrobp.2007.07.2352

Grutters, J. P. C., Kessels, A. G. H., Pijls-Johannesma, M., De Ruysscher, D., Joore, M. A., & Lambin, P. (2010). Comparison of the effectiveness of radiotherapy with photons, protons and carbon-ions for non-small cell lung cancer: A meta-analysis. *Radiotherapy and Oncology*, *95*(1), 32–40. http://doi.org/10.1016/j.radonc.2009.08.003

Guckenberger, M., Meyer, J., Vordermark, D., Baier, K., Wilbert, J., & Flentje, M. (2006). Magnitude and clinical relevance of translational and rotational patient setup errors: A cone-beam CT study. *International Journal of Radiation Oncology, Biology, Physics*, *65*(3), 934–942. http://doi.org/10.1016/j.ijrobp.2006.02.019

Guckenberger, M., Meyer, J., Wilbert, J., Baier, K., Sauer, O., & Flentje, M. (2007). Precision of Image-Guided Radiotherapy (IGRT) in Six Degrees of Freedom and Limitations in Clinical Practice. *Strahlentherapie Und Onkologie*, *183*(6), 307–313. http://doi.org/10.1007/s00066-007-1695-0

Guckenberger, M., Meyer, J., Wilbert, J., Richter, A., Baier, K., Mueller, G., & Flentje, M. (2007). Intra-fractional uncertainties in cone-beam CT based image-guided radiotherapy (IGRT) of pulmonary tumors. *Radiotherapy and Oncology*, *83*(1), 57–64. http://doi.org/10.1016/j.radonc.2007.01.012

Guckenberger, M., Richter, A., Wilbert, J., Flentje, M., & Partridge, M. (2011). Adaptive radiotherapy for locally advanced non-small-cell lung cancer does

not underdose the microscopic disease and has the potential to increase tumor control. *International Journal of Radiation Oncology, Biology, Physics*, *81*(4), 275–282. http://doi.org/10.1016/j.ijrobp.2011.01.067

Haasbeek, C. J. a, Slotman, B. J., & Senan, S. (2009). Radiotherapy for lung cancer: clinical impact of recent technical advances. *Lung Cancer (Amsterdam, Netherlands)*, *64*(1), 1–8. http://doi.org/10.1016/j.lungcan.2008.07.008

Hall, E., & Giaccia, A. (2006). *Radiobiology for the Radiologist*. Lippincott Williams & Wilkins.

Hall, E. J., & Wuu, C.S. (2003). Radiation-induced second cancers: the impact of 3D-CRT and IMRT. *International Journal of Radiation Oncology, Biology, Physics*, *56*(1), 83–88. http://doi.org/10.1016/S0360-3016(03)00073-7

Han, K., Cheung, P., Basran, P. S., Poon, I., Yeung, L., & Lochray, F. (2010). A comparison of two immobilization systems for stereotactic body radiation therapy of lung tumors. *Radiotherapy and Oncology*, *95*(1), 103–108. http://doi.org/10.1016/j.radonc.2010.01.025

Hanley, J., Debois, M. M., Mah, D., Mageras, G. S., Raben, A., Rosenzweig, K., … Kutcher, G. J. (1999). Deep inspiration breath-hold technique for lung tumors: the potential value of target immobilization and reduced lung density in dose escalation. *International Journal of Radiation Oncology, Biology, Physics*, *45*(3), 603–611. http://doi.org/10.1016/S0360-3016(99)00154-6

Harsolia, A., Hugo, G. D., Kestin, L. L., Grills, I. S., & Yan, D. (2008). Dosimetric Advantages of Four-Dimensional Adaptive Image-Guided Radiotherapy for Lung Tumors Using Online Cone-Beam Computed Tomography. *International Journal of Radiation Oncology, Biology, Physics*, *70*(2), 582–589. http://doi.org/10.1016/j.ijrobp.2007.08.078

Heath, E., Unkelbach, J., & Oelfke, U. (2009). Incorporating uncertainties in respiratory motion into 4D treatment plan optimization. *Medical Physics*, *36*(7), 3059–3071. http://doi.org/10.1118/1.3148582

Henkelman, R. M., & Mah, K. (1982). How important is breathing in radiation therapy of the thorax? *International Journal of Radiation Oncology, Biology, Physics*, *8*(11), 2005–2010. http://doi.org/10.1016/0360-3016(82)90462-X

Henschke, C. I., McCauley, D. I., Yankelevitz, D. F., Naidich, D. P., McGuinness, G., Miettinen, O. S., … Smith, J. P. (1999). Early Lung Cancer Action Project: Overall design and findings from baseline screening. *Lancet*, *354*(9173), 99–105. http://doi.org/10.1016/S0140-6736(99)06093-6

Higgins, J., Bezjak, A., Franks, K., Le, L. W., Cho, B. C., Payne, D., & Bissonnette, J. P. (2009). Comparison of Spine, Carina, and Tumor as Registration Landmarks for Volumetric Image-Guided Lung Radiotherapy. *International Journal of Radiation Oncology, Biology, Physics*, *73*(5), 1404–1413. http://doi.org/10.1016/j.ijrobp.2008.06.1926

Higgins, J., Bezjak, A., Hope, A., Panzarella, T., Li, W., Cho, J. B. C., … Bissonnette, J. P. (2011). Effect of image-guidance frequency on geometric accuracy and setup margins in radiotherapy for locally advanced lung cancer. *International Journal of Radiation Oncology, Biology, Physics*, *80*(5), 1330–1337. http://doi.org/10.1016/j.ijrobp.2010.04.006

Hugo, G. D., Yan, D., & Liang, J. (2007). Population and patient-specific target margins for 4D adaptive radiotherapy to account for intra- and inter-fraction variation in lung tumour position. *Physics in Medicine and Biology*, *52*(1), 257–274. http://doi.org/10.1088/0031-9155/52/1/017

ICRU, International Commission on Radiation Units and Measurements. (1993). *Prescribing, recording and reporting photon beam therapy (Report 50)*. Bethesda, MD.

ICRU, International Commission on Radiation Units and Measurements. (1999). *Prescribing, recording and reporting photon beam therapy (Report 62)*. Bethesda, MD.

Jabbour, S. K., Kim, S., Haider, S. A., Xu, X., Wu, A., Surakanti, S., … Zou, W. (2015). Reduction in Tumor Volume by Cone Beam Computed Tomography Predicts Overall Survival in Non-Small Cell Lung Cancer Treated With Chemoradiation Therapy. *International Journal of Radiation Oncology, Biology, Physics*, *92*(3), 627–633. http://doi.org/10.1016/j.ijrobp.2015.02.017

Jaffray, D. A. (2012). Image-guided radiotherapy: from current concept to future perspectives. *Nature Reviews Clinical Oncology*, *9*(12), 688–699. http://doi.org/10.1038/nrclinonc.2012.194

Jaffray, D. A., Langen, K. M., Mageras, G., Dawson, L. A., Yan, D., Adams, R., … Fraass, B. (2013). Safety considerations for IGRT: Executive summary. *Practical Radiation Oncology*, *3*(3), 167–170. http://doi.org/10.1016/j.prro.2013.01.004

Jaffray, D., Kupelian, P., Djemil, T., & Macklis, R. M. (2007). Review of image-guided radiation therapy. *Expert Review of Anticancer Therapy*, *7*(1), 89–103. http://doi.org/10.1586/14737140.7.1.89

James, S. St., Mishra, P., Hacker, F., Berbeco, R. I., Lewis, J. H. (2012). Quantifying ITV instabilities arising from 4DCT: a simulation study using patient data. *Physics in Medicine and Biology*, *57*(5), L1–L7. http://doi.org/10.1088/0031-9155/57/5/L1

Juhler Nøttrup, T., Korreman, S. S., Pedersen, A. N., Aarup, L. R., Nyström, H., Olsen, M., & Specht, L. (2007). Intra- and interfraction breathing variations during curative radiotherapy for lung cancer. *Radiotherapy and Oncology*, *84*(1), 40–48. http://doi.org/10.1016/j.radonc.2007.05.026

Keall, P. J., Mageras, G. S., Balter, J. M., Emery, R. S., Forster, K. M., Jiang, S. B., … Yorke, E. (2006). The management of respiratory motion in radiation

oncology report of AAPM Task Group 76. *Medical Physics*, *33*(10), 3874–3900. http://doi.org/10.1118/1.2349696

Kilburn, J. M., Soike, M. H., Lucas, J. T., Ayala-Peacock, D., Blackstock, W., Isom, S., … Urbanic, J. J. (2016). Image guided radiation therapy may result in improved local control in locally advanced lung cancer patients. *Practical Radiation Oncology*, *6*(3), e73–e80. http://doi.org/10.1016/j.prro.2015.10.004

Kubo, H. D., & Hill, B. C. (1996). Respiration gated radiotherapy treatment: a technical study. *Physics in Medicine and Biology*, *41*, 83–91.

Kung, J. H., Zygmanski, P., Choi, N., & Chen, G. T. Y. (2003). A method of calculating a lung clinical target volume DVH for IMRT with intrafractional motion. *Medical Physics Med. Phys*, *30*(552). http://doi.org/10.1118/1.1576233

Kwint, M., Conijn, S., Schaake, E., Knegjens, J., Rossi, M., Remeijer, P., … Belderbos, J. (2014). Intra thoracic anatomical changes in lung cancer patients during the course of radiotherapy. *Radiotherapy and Oncology*, *113*, 392–397. http://doi.org/10.1016/j.radonc.2014.10.009

Lagerwaard, F. J., Van Sornsen de Koste, J. R., Nijssen-Visser, M. R. J., Schuchhard-Schipper, R. H., Oei, S. S., Munne, A., & Senan, S. (2001). Multiple "slow" CT scans for incorporating lung tumor mobility in radiotheraphy planning. *International Journal of Radiation Oncology, Biology, Physics*, *51*(4), 932–937. http://doi.org/10.1016/S0360-3016(01)01716-3

Larry, C. K., Mary, G., Bahman, E., Karen, H., & Rush. (1993). Radiation therapy alone for stage I non-small cell lung cancer. *International Journal of Radiation Oncology, Biology, Physics*, *27*(3), 517–523. http://doi.org/10.1088/0031-9155/61/4/1515

Lavoie, C., Higgins, J., Bissonnette, J.P., Le, L. W., Sun, A., Brade, A., … Bezjak, A. (2012). Volumetric Image Guidance Using Carina vs Spine as Registration Landmarks for Conventionally Fractionated Lung Radiotherapy. *International Journal of Radiation Oncology, Biology, Physics*, *84*(5), 1086–1092. http://doi.org/10.1016/j.ijrobp.2012.02.012

Lee, J., Kim, J.-I., Ye, S.J., Kim, H. J., Carlson, J., & Park, J. M. (2015). Dosimetric effects of roll rotational setup errors on lung stereotactic ablative radiotherapy using volumetric modulated arc therapy. *http://dx.doi.org/10.1259/bjr.20140862*.

Lee, S., Wolberg, G., & Shin, S. Y. (1997). Scattered data interpolation with multilevel B-splines. *IEEE Transactions on Visualization and Computer Graphics*, *3*(3), 228–244. http://doi.org/10.1109/2945.620490

Li, W., Jaffray, D. A., Wilson, G., & Moseley, D. (2016). How long does it take? An analysis of volumetric image assessment time. *Radiotherapy and*

*Oncology*, *119*(1), 150–153. http://doi.org/http://dx.doi.org/10.1016/j.radonc.2016.01.015

Lim, G., Bezjak, A., Higgins, J., Moseley, D., Hope, A. J., Sun, A., … Bissonnette, J.P. (2011). Tumor regression and positional changes in non-small cell lung cancer during radical radiotherapy. *Journal of Thoracic Oncology : Official Publication of the International Association for the Study of Lung Cancer*, *6*(3), 531–536. http://doi.org/10.1097/JTO.0b013e31820b8a52

Lips, I. M., van der Heide, U. A., Kotte, A. N. T. J., van Vulpen, M., & Bel, A. (2009). Effect of Translational and Rotational Errors on Complex Dose Distributions With Off-Line and On-Line Position Verification. *International Journal of Radiation Oncology, Biology, Physics*, *74*(5), 1600–1608. http://doi.org/10.1016/j.ijrobp.2009.02.056

Liu, H. H., Balter, P., Tutt, T., Choi, B., Zhang, J., Wang, C., … Dong, L. (2007). Assessing Respiration-Induced Tumor Motion and Internal Target Volume Using Four-Dimensional Computed Tomography for Radiotherapy of Lung Cancer. *International Journal of Radiation Oncology, Biology, Physics*, *68*(2), 531–540. http://doi.org/10.1016/j.ijrobp.2006.12.066

Liu, H., & Wu, Q. (2011). Dosimetric and geometric evaluation of a hybrid strategy of offline adaptive planning and online image guidance for prostate cancer radiotherapy. *Physics in Medicine and Biology*, *56*(15), 5045–5062. http://doi.org/10.1118/1.3182218

Lu, B., Mittauer, K., Li, J., Samant, S., Dagan, R., Okunieff, P., … Liu, C. (2012). A patient alignment solution for lung SBRT setups based on a deformable registration technique. *Medical Physics*, *39*(12), 7379. http://doi.org/10.1118/1.4766875

Lu, W., Olivera, G. H., Chen, Q., Ruchala, K. J., Haimerl, J., Meeks, S. L., … Kupelian, P. A. (2006). Deformable registration of the planning image (kVCT) and the daily images (MVCT) for adaptive radiation therapy. *Physics in Medicine and Biology*, *51*(17), 4357–4374. http://doi.org/10.1088/0031-9155/51/17/015

Mageras, G. S., & Yorke, E. (2004). Deep inspiration breath hold and respiratory gating strategies for reducing organ motion in radiation treatment. *Seminars in Radiation Oncology*, *14*(1), 65–75. http://doi.org/10.1053/j.semradonc.2003.10.009

Maintz, J. B., & Viergever, M. A. (1998). A survey of medical image registration. *Medical Image Analysis*, *2*(1), 1–36. http://doi.org/10.1016/S1361-8415(01)80026-8

Mancosu, P., Reggiori, G., Gaudino, A., Lobefalo, F., Paganini, L., Palumbo, V., … Scorsetti, M. (2015). Are pitch and roll compensations required in all pathologies? A data analysis of 2945 fractions. *The British Journal of*

*Radiology*, *88*(1055), 20150468. http://doi.org/10.1259/bjr.20150468

Markelj, P., Tomaževič, D., Likar, B., & Pernuš, F. (2012). A review of 3D/2D registration methods for image-guided interventions. *Medical Image Analysis*, *16*(3), 642–661. http://doi.org/10.1016/j.media.2010.03.005

Marks, L. B., Yorke, E. D., Jackson, A., Ten Haken, R. K., Constine, L. S., Eisbruch, A., … Deasy, J. O. (2010). Use of Normal Tissue Complication Probability Models in the Clinic. *International Journal of Radiation Oncology, Biology, Physics*, *76*(3 SUPPL.). http://doi.org/10.1016/j.ijrobp.2009.07.1754

McKenzie, A., van Herk, M., & Mijnheer, B. (2002). Margins for geometric uncertainty around organs at risk in radiotherapy. *Radiotherapy and Oncology*, *62*(3), 299–307. http://doi.org/10.1016/S0167-8140(02)00015-4

McQuaid, D., & Webb, S. (2006). IMRT delivery to a moving target by dynamic MLC tracking: delivery for targets moving in two dimensions in the beam's eye view. *Physics in Medicine and Biology*, *51*(19), 4819–4839. http://doi.org/10.1088/0031-9155/51/19/007

Meijer, G. J., de Klerk, J., Bzdusek, K., van den Berg, H. A., Janssen, R., Kaus, M. R., … van der Toorn, P. P. (2008). What CTV-to-PTV Margins Should Be Applied for Prostate Irradiation? Four-Dimensional Quantitative Assessment Using Model-Based Deformable Image Registration Techniques. *International Journal of Radiation Oncology, Biology, Physics*, *72*(5), 1416–1425. http://doi.org/10.1016/j.ijrobp.2008.03.005

Metcalfe, P. E., Wong, T. P., & Hoban, P. W. (1993). Radiotherapy X-ray beam inhomogeneity corrections: the problem of lateral electronic disequilibrium in lung. *Australasian Physical & Engineering Sciences in Medicine / Supported by the Australasian College of Physical Scientists in Medicine and the Australasian Association of Physical Sciences in Medicine*, *16*(4), 155–67. Retrieved from http://www.ncbi.nlm.nih.gov/pubmed/8122987

Miller, R. C., Bonner, J. A., & Kline, R. W. (1998). Impact of beam energy and field margin on penumbra at lung tumor-lung parenchyma interfaces. *International Journal of Radiation Oncology, Biology, Physics*, *41*(3), 707–713. http://doi.org/10.1016/S0360-3016(98)00133-3

Mok, H., Crane, C. H., Palmer, M. B., Briere, T. M., Beddar, S., Delclos, M. E., … Das, P. (2011). Intensity modulated radiation therapy (IMRT): differences in target volumes and improvement in clinically relevant doses to small bowel in rectal carcinoma. *Radiation Oncology*, *6*(1), 63. http://doi.org/10.1186/1748-717X-6-63

Murphy, M. J. (2004). Tracking moving organs in real time. *Seminars in Radiation Oncology*, *14*(1), 91–100. http://doi.org/10.1053/j.semradonc.2003.10.005

Murphy, M. J. (2007). Image-guided patient positioning: If one cannot correct for

rotational offsets in external-beam radiotherapy setup, how should rotational offsets be managed? *Medical Physics*, *34*(6), 1880. http://doi.org/10.1118/1.2731485

Murshed, H., Liu, H. H., Liao, Z., Barker, J. L., Wang, X., Tucker, S. L., … Change, J. Y. (2004). Dose and volume reduction for normal lung using intensity-modulated radiotherapy for advanced-stage non-small-cell lung cancer. *International Journal of Radiation Oncology, Biology, Physics*, *58*(4), 1258–67. http://doi.org/10.1016/j.ijrobp.2003.09.086

Mutanga, T. F., De Boer, H. C. J., Van Der Wielen, G. J., Hoogeman, M. S., Incrocci, L., & Heijmen, B. J. M. (2011). Margin evaluation in the presence of deformation, rotation, and translation in prostate and entire seminal vesicle irradiation with daily marker-based setup corrections. *International Journal of Radiation Oncology, Biology, Physics*, *81*(4), 1160–1167. http://doi.org/10.1016/j.ijrobp.2010.09.013

Nabavizadeh, N., Elliott, D. A., Chen, Y., Kusano, A. S., Mitin, T., Thomas, C. R., & Holland, J. M. (2016). Image Guided Radiation Therapy (IGRT) Practice Patterns and IGRT's Impact on Workflow and Treatment Planning: Results From a National Survey of American Society for Radiation Oncology Members. *International Journal of Radiation Oncology, Biology, Physics*, *94*(4), 850–857. http://doi.org/10.1016/j.ijrobp.2015.09.035

Negoro, Y., Nagata, Y., Aoki, T., Mizowaki, T., Araki, N., Takayama, K., … Hiraoka, M. (2001). The effectiveness of an immobilization device in conformal radiotherapy for lung tumor: reduction of respiratory tumor movement and evaluation of the daily setup accuracy. *International Journal of Radiation Oncology, Biology, Physics*, *50*(4), 889–898. http://doi.org/10.1016/S0360-3016(01)01516-4

Nelder, J. A., & Mead, R. (1965). A Simplex Method for Function Minimization. *The Computer Journal*, *7*(4), 308–313. http://doi.org/10.1093/comjnl/7.4.308

Nelson, C., Starkschall, G., & Chang, J. Y. (2006). The potential for dose escalation in lung cancer as a result of systematically reducing margins used to generate planning target volume. *International Journal of Radiation Oncology, Biology, Physics*, *65*(2), 573–586. http://doi.org/10.1016/j.ijrobp.2006.01.032

Njeh, C. (2008). Tumor delineation: The weakest link in the search for accuracy in radiotherapy. *Journal of Medical Physics*, *33*(4), 136. http://doi.org/10.4103/0971-6203.44472

Ohara, K., Okumura, T., Akisada, M., Inada, T., Mori, T., Yokota, H., & Calaguas, M. J. B. (1989). Irradiation synchronized with respiration gate. *International Journal of Radiation Oncology, Biology, Physics*, *17*(4), 853–857. http://doi.org/10.1016/0360-3016(89)90078-3

Oldham, M., Neal, A., & Webb, S. (1995). A comparison of conventional

"forward planning" with inverse planning for 3D conformal radiotherapy of the prostate. *Radiotherapy and Oncology*, *35*(3), 248–262. http://doi.org/10.1016/0167-8140(95)01556-V

Otto, K. (2008). Volumetric modulated arc therapy: IMRT in a single gantry arc. *Medical Physics*, *35*(1), 310. http://doi.org/10.1118/1.2818738

Paganelli, C., Lee, D., Greer, P. B., Baroni, G., Riboldi, M., & Keall, P. (2015). Quantification of lung tumor rotation with automated landmark extraction using orthogonal cine MRI images. *Physics in Medicine and Biology*, *60*(18), 7165–7178. http://doi.org/10.1088/0031-9155/60/18/7165

Pan, X., Sidky, E. Y., & Vannier, M. (2009). Why do commercial CT scanners still employ traditional, filtered back-projection for image reconstruction? *Inverse Problems*, *25*(12), 1230009. http://doi.org/10.1088/0266-5611/25/12/123009

Peng, J. L., Liu, C., Chen, Y., Amdur, R. J., Vanek, K., & Li, J. G. (2011). Dosimetric consequences of rotational setup errors with direct simulation in a treatment planning system for fractionated stereotactic radiotherapy. *Journal of Applied Clinical Medical Physics*, *12*(3). http://doi.org/10.1120/JACMP.V12I3.3422

Purdie, T. G., Bissonnette, J. P., Franks, K., Bezjak, A., Payne, D., Sie, F., … Jaffray, D. A. (2007). Cone-Beam Computed Tomography for On-Line Image Guidance of Lung Stereotactic Radiotherapy: Localization, Verification, and Intrafraction Tumor Position. *International Journal of Radiation Oncology, Biology, Physics*, *68*(1), 243–252. http://doi.org/10.1016/j.ijrobp.2006.12.022

Quan, E. M., Chang, J. Y., Liao, Z., Xia, T., Yuan, Z., Liu, H., … Zhang, X. (2012). Automated volumetric modulated Arc therapy treatment planning for stage III lung cancer: how does it compare with intensity-modulated radio therapy? *International Journal of Radiation Oncology, Biology, Physics*, *84*(1), e69-76. http://doi.org/10.1016/j.ijrobp.2012.02.017

Quan, E. M., Li, X., Li, Y., Wang, X., Kudchadker, R. J., Johnson, J. L., … Zhang, X. (2012). A comprehensive comparison of IMRT and VMAT plan quality for prostate cancer treatment. *International Journal of Radiation Oncology, Biology, Physics*, *83*(4), 1169–1178. http://doi.org/10.1016/j.ijrobp.2011.09.015

Rahman, F. (2014). *Evaluation of soft-tissue match methods for utilization in CBCT guided adaptive radiotherapy of lung cancer patients – clinical benefits, limitations and margin determination*. Lund University.

Redpath, A. T., & Muren, L. P. (2005). An optimisation algorithm for determination of treatment margins around moving and deformable targets. *Radiotherapy and Oncology*, *77*(2), 194–201. http://doi.org/10.1016/j.radonc.2005.07.010

Redpath, A. T., Wright, P., & Muren, L. P. (2009). The contribution of on-line correction for rotational organ motion in image-guided radiotherapy of the bladder and prostate. *Acta Oncologica*, *47*(7), 1367–1372. http://doi.org/10.1080/02841860802263232

Remeijer, P., Geerlof, E., Ploeger, L., Gilhuijs, K., van Herk, M., & Lebesque, J. V. (2000). 3-D portal image analysis in clinical practice: an evaluation of 2-D and 3-D analysis techniques as applied to 30 prostate cancer patients. *International Journal of Radiation Oncology, Biology, Physics*, *46*(5), 1281–1290. http://doi.org/10.1016/S0360-3016(99)00468-X

Sawant, A., Venkat, R., Srivastava, V., Carlson, D., Povzner, S., Cattell, H., & Keall, P. (2008). Management of three-dimensional intrafraction motion through real-time DMLC tracking. *Medical Physics*, *35*(5), 2050. http://doi.org/10.1118/1.2905355

Schweikard, A., Glosser, G., Bodduluri, M., Murphy, M. J., & Adler, J. R. (2000). Robotic motion compensation for respiratory movement during radiosurgery. *Computer Aided Surgery*, *5*(4), 263–277. http://doi.org/http://dx.doi.org/10.3109/10929080009148894

Sederberg, T. W., Parry, S. R., Sederberg, T. W., & Parry, S. R. (1986). Free-form deformation of solid geometric models. *ACM SIGGRAPH Computer Graphics*, *20*(4), 151–160. http://doi.org/10.1145/15886.15903

Senan, S., van Sörnsen de Koste, J., Samson, M., Tankink, H., Jansen, P., Nowak, P. J., … Lagerwaard, F. J. (1999). Evaluation of a target contouring protocol for 3D conformal radiotherapy in non-small cell lung cancer. *Radiotherapy and Oncology*, *53*(3), 247–255. http://doi.org/10.1016/S0167-8140(99)00143-7

Shannon, C. E. (2001). A mathematical theory of communication. *ACM SIGMOBILE Mobile Computing and Communications Review*, *5*(1), 3. http://doi.org/10.1145/584091.584093

Shih, H. A., Jiang, S. B., Aljarrah, K. M., Doppke, K. P., & Choi, N. C. (2004). Internal target volume determined with expansion margins beyond composite gross tumor volume in three-dimensional conformal radiotherapy for lung cancer. *International Journal of Radiation Oncology, Biology, Physics*, *60*(2), 613–622. http://doi.org/10.1016/j.ijrobp.2004.05.031

Shimizu, S., Shirato, H., Kagei, K., Nishioka, T., Bo, X., Dosaka-Akita, H., … Miyasaka, K. (2000). Impact of respiratory movement on the computed tomographic images of small lung tumors in three-dimensional (3D) radiotherapy. *International Journal of Radiation Oncology, Biology, Physics*, *46*(5), 1127–1133. http://doi.org/10.1016/S0360-3016(99)00352-1

Shirato, H., Seppenwoolde, Y., Kitamura, K., Onimura, R., & Shimizu, S. (2004). Intrafractional tumor motion: lung and liver. *Seminars in Radiation Oncology*, *14*(1), 10–18. http://doi.org/10.1053/j.semradonc.2003.10.008

Siker, M. L., Tomé, W. A., & Mehta, M. P. (2006). Tumor volume changes on serial imaging with megavoltage CT for non–small-cell lung cancer during intensity-modulated radiotherapy: How reliable, consistent, and meaningful is the effect? *International Journal of Radiation Oncology, Biology, Physics*, *66*(1), 135–141. http://doi.org/10.1016/j.ijrobp.2006.03.064

Sixel, K. E., Ruschin, M., Tirona, R., & Cheung, P. C. F. (2003). Digital fluoroscopy to quantify lung tumor motion: Potential for patient-specific planning target volumes. *International Journal of Radiation Oncology, Biology, Physics*, *57*(3), 717–723. http://doi.org/10.1016/S0360-3016(03)00713-2

Sotiras, A., Davatzikos, C., & Paragios, N. (2013). Deformable Medical Image Registration: A Survey. *IEEE Transactions on Medical Imaging*, *32*(7), 1153–1190. http://doi.org/10.1109/TMI.2013.2265603

Steenbakkers, R. J. H. M., Duppen, J. C., Fitton, I., Deurloo, K. E. I., Zijp, L. J., Comans, E. F. I., … Rasch, C. R. N. (2006). Reduction of observer variation using matched CT-PET for lung cancer delineation: A three-dimensional analysis. *International Journal of Radiation Oncology, Biology, Physics*, *64*(2), 435–448. http://doi.org/10.1016/j.ijrobp.2005.06.034

Stroom, J. C., De Boer, H. C. J., Huizenga, H., & Visser, A. G. (1999). Inclusion of geometrical uncertanties in radiotherapy treatment planning by means of coverage probability. *International Journal of Radiation Oncology, Biology, Physics*, *43*(4), 905–919.

Studholme, C., Hill, D. L. G., & Hawkes, D. J. (1999). An overlap invariant entropy measure of 3D medical image alignment. *Pattern Recognition*, *32*(1), 71–86. http://doi.org/10.1016/S0031-3203(98)00091-0

Suzuki, O., Nishiyama, K., Ueda, Y., Miyazaki, M., & Tsujii, K. (2012). Influence of Rotational Setup Error on Tumor Shift in Bony Anatomy Matching Measured with Pulmonary Point Registration in Stereotactic Body Radiotherapy for Early Lung Cancer. *Japanese Journal of Clinical Oncology*, *42*(12), 1181–1186. http://doi.org/10.1093/jjco/hys167

Takahashi, S., & Matsuda, T. (1960). Axial Transverse Laminagraphy Applied to Rotational Therapy. *Radiology*, *74*, 61–64. http://doi.org/http://dx.doi.org/10.1148/74.1.61

Tyldesley, S., Boyd, C., Schulze, K., Walker, H., & Mackillop, W. J. (2001). Estimating the need for radiotherapy for lung cancer: An evidence-based, epidemiologic approach. *International Journal of Radiation Oncology, Biology, Physics*, *49*(4), 973–985. http://doi.org/10.1016/S0360-3016(00)01401-2

Underberg, R. W. M., Lagerwaard, F. J., Slotman, B. J., Cuijpers, J. P., & Senan, S. (2005). Use of maximum intensity projections (MIP) for target volume generation in 4DCT scans for lung cancer. *International Journal of*

*Radiation Oncology, Biology, Physics*, *63*(1), 253–260. http://doi.org/10.1016/j.ijrobp.2005.05.045

Van de Steene, J., Linthout, N., de Mey, J., Vinh-Hung, V., Claassens, C., Noppen, M., … Storme, G. (2002). Definition of gross tumor volume in lung cancer: inter-observer variability. *Radiotherapy and Oncology*, *62*(1), 37–49. http://doi.org/10.1016/S0167-8140(01)00453-4

van der Voort van Zyp, N. C., Prévost, J.-B., Hoogeman, M. S., Praag, J., van der Holt, B., Levendag, P. C., … Nuyttens, J. J. (2009). Stereotactic radiotherapy with real-time tumor tracking for non-small cell lung cancer: Clinical outcome. *Radiotherapy and Oncology*, *91*(3), 296–300. http://doi.org/10.1016/j.radonc.2009.02.011

van Herk, M. (2004). Errors and Margins in Radiotherapy. *Seminars in Radiation Oncology*, *14*(1), 52–64. http://doi.org/10.1053/j.semradonc.2003.10.003

van Herk, M., Remeijer, P., & Lebesque, J. V. (2002). Inclusion of geometric uncertainties in treatment plan evaluation. *International Journal of Radiation Oncology, Biology, Physics*, *52*(5), 1407–1422. http://doi.org/10.1016/S0360-3016(01)02805-X

van Herk, M., Remeijer, P., Rasch, C., & Lebesque, J. V. (2000). The probability of correct target dosage: Dose-population histograms for deriving treatment margins in radiotherapy. *International Journal of Radiation Oncology, Biology, Physics*, *47*(4), 1121–1135. http://doi.org/10.1016/S0360-3016(00)00518-6

van Sörnsen de Koste, J. R., Lagerwaard, F. J., Schuchhard-Schipper, R. H., Nijssen-Visser, M. R. J., Voet, P. W. J., Oei, S. S., & Senan, S. (2001). Dosimetric consequences of tumor mobility in radiotherapy of stage I non-small cell lung cancer – an analysis of data generated using "slow" CT scans. *Radiotherapy and Oncology*, *61*(1), 93–99. http://doi.org/10.1016/S0167-8140(01)00373-5

Varadhan, R., Karangelis, G., Krishnan, K., & Hui, S. (2013). A framework for deformable image registration validation in radiotherapy clinical applications. *Journal of Applied Clinical Medical Physics / American College of Medical Physics*, *14*(1), 4066. Retrieved from http://www.ncbi.nlm.nih.gov/pubmed/23318394

Vedam, S. S., Keall, P. J., Kini, V. R., Mostafavi, H., Shukla, H. P., & Mohan, R. (2003). Acquiring a four-dimensional computed tomography dataset using an external respiratory signal. *Physics in Medicine and Biology*, *48*(1), 45–62. http://doi.org/10.1088/0031-9155/48/1/304

Verhaegen, F., & Seuntjens, J. (2003). Monte Carlo modelling of external radiotherapy photon beams. *Physics in Medicine and Biology*, *48*(21), R107-64. http://doi.org/10.1088/0031-9155/48/21/R01

Vorwerk, H., Beckmann, G., Bremer, M., Degen, M., Dietl, B., Fietkau, R., …

Christiansen, H. (2009). The delineation of target volumes for radiotherapy of lung cancer patients. *Radiotherapy and Oncology*, *91*(3), 455–460. http://doi.org/10.1016/j.radonc.2009.03.014

Wang, L., Feigenberg, S., Chen, L., Pasklev, K., & Ma, C. (2006). Benefit of three-dimensional image-guided stereotactic localization in the hypofractionated treatment of lung cancer. *International Journal of Radiation Oncology, Biology, Physics*, *66*(3), 738–747. http://doi.org/10.1016/j.ijrobp.2006.05.032

Wang, L., Feigenberg, S., Fan, J., Jin, L., Turaka, A., Chen, L., & Ma, C.-M. C. (2012). Target Repositional Accuracy and PTV Margin Verification using Three-dimensional Cone-Beam Computed Tomography (CBCT) in Stereotactic Body Radiotherapy (SBRT) of Lung Cancers. *Journal of Applied Clinical Medical Physics*, *13*(2).

Wang, L., Zhang, S., Yuan, K., Zhou, L., & Wang, R. (2015). Dosimetric study of the deformable image registration based lung cancer adaptive radiotherapy. In *2015 8th International Conference on Biomedical Engineering and Informatics (BMEI)* (pp. 402–406). IEEE. http://doi.org/10.1109/BMEI.2015.7401538

Webb, S. (1989). Optimisation of conformal radiotherapy dose distribution by simulated annealing. *Physics in Medicine and Biology*, *34*(10), 1349–1370. http://doi.org/10.1088/0031-9155/34/10/002

Webb, S. (2003). The physical basis of IMRT and inverse planning. *The British Journal of Radiology*, *76*(910), 678–89. http://doi.org/http://dx.doi.org/10.1259/bjr/65676879

Weiss, E., & Hess, C. F. (2003). The Impact of Gross Tumor Volume (GTV) and Clinical Target Volume (CTV) Definition on the Total Accuracy in Radiotherapy. *Strahlentherapie Und Onkologie*, *179*(1), 21–30. http://doi.org/10.1007/s00066-003-0976-5

Wells, W. M., Viola, P., Atsumi, H., Nakajima, S., & Kikinis, R. (1996). Multi-modal volume registration by maximization of mutual information. *Medical Image Analysis*, *1*(1), 35–51. http://doi.org/10.1016/S1361-8415(01)80004-9

Wierzbicki, M., Drangova, M., Guiraudon, G., & Peters, T. (2004). Validation of dynamic heart models obtained using non-linear registration for virtual reality training, planning, and guidance of minimally invasive cardiac surgeries. *Medical Image Analysis*, *8*(3), 387–401. http://doi.org/10.1016/j.media.2004.06.014

Wolthaus, J. W. H., Schneider, C., Sonke, J.J., van Herk, M., Belderbos, J. S. A., Rossi, M. M. G., … Damen, E. M. F. (2006). Mid-ventilation CT scan construction from four-dimensional respiration-correlated CT scans for radiotherapy planning of lung cancer patients. *International Journal of Radiation Oncology, Biology, Physics*, *65*(5), 1560–1571.

http://doi.org/10.1016/j.ijrobp.2006.04.031

Wong, J. W., Sharpe, M. B., Jaffray, D. A., Kini, V. R., Robertson, J. M., Stromberg, J. S., & Martinez, A. A. (1999). The use of active breathing control (ABC) to reduce margin for breathing motion. *International Journal of Radiation Oncology, Biology, Physics*, *44*(4), 911–919. http://doi.org/10.1016/S0360-3016(99)00056-5

Wurstbauer, K., Deutschmann, H., Kopp, P., & Sedlmayer, F. (2005). Radiotherapy planning for lung cancer: Slow CTs allow the drawing of tighter margins. *Radiotherapy and Oncology*, *75*(2), 165–170. http://doi.org/10.1016/j.radonc.2005.02.003

Yan, D., Vicini, F., Wong, J., & Martinez, A. (1997). Adaptive radiation therapy. *Physics in Medicine and Biology*, *42*(1), 123–132. http://doi.org/10.1155/2011/690595

Yang, Y., Catalano, S., Kelsey, C. R., Yoo, D. S., Yin, F.F., & Cai, J. (2014). Dosimetric effects of rotational offsets in stereotactic body radiation therapy (SBRT) for lung cancer. *Medical Dosimetry*, *39*(1), 117–121. http://doi.org/10.1016/j.meddos.2013.11.002

Yanyang, W., Xiaolong, F., & Bing, X. (2010). Impact of different anatomical landmarks on registration in imaging-guided radiation for lung cancer. *Chinese Journal of Radiation Oncology*, *19*(6), 517–519.

Yeung, A. R., Li, J. G., Shi, W., Newlin, H. E., Chvetsov, A., Liu, C., … Olivier, K. (2009). Tumor Localization Using Cone-Beam CT Reduces Setup Margins in Conventionally Fractionated Radiotherapy for Lung Tumors. *International Journal of Radiation Oncology, Biology, Physics*, *74*(4), 1100–1107. http://doi.org/10.1016/j.ijrobp.2008.09.048